Politecnico di Torino

Master's Degree in

Physics of Complex Systems

Master's Degree Thesis

Effects of Doping on Stripe Order and Superconductivity in Cuprates:

A Variational Monte Carlo Approach

Supervisor: Candidate:

Prof. Luca Fausto TOCCHIO Antonio LECHIARA

April 2023

Abstract

High-temperature superconductors constitute a very special class of materials, whose puzzling properties and rich physics have caught the attention of the physicists soon after their discovery. The peculiar self-organization of the electrons into periodic structures of wavelength λ breaking the periodicities of the underlying lattice, called stripes, is found to coexist with superconducting correlations.

By employing Variational Monte Carlo simulations on a single-band Hubbard model on the square lattice with both nearest-(t) and next-nearest-(t') neighbour hopping, the present work investigates the consequences of increasing hole doping on the instauration of stripes and the behavior of the superconducting order parameter, with a particular focus on cuprate superconductors, along with a discussion on how the two phenomena affect each other. We consider two different values of the next-nearest neighbour hopping parameter, that are appropriate for describing cuprate superconductors.

We observe that stripes are the optimal state in a wide doping range, while they melt into a uniform state for large values of the doping. A larger absolute value of the next-nearest neighbour hopping is found to penalize the formation of stripes. The existence of charge and spin order, associated to the static structure factor $N(\mathbf{q})$ and the spin-spin correlations $S(\mathbf{q})$ respectively, is discussed, along with the metallic or insulating character of the stripes. Superconducting pair-pair correlations $D(x)$ indicating the presence of superconductivity are, on the other hand, suppressed with respect to the uniform state, suggesting a com-

peting interplay between stripes and superconductivity. The phase diagram for the single-band Hubbard model is found to be dominated by stripes, leaving little room for superconductivity.

Our findings shed light on the underlying physics of these complex materials and contribute to a deeper understanding of high-temperature superconductivity, with potential applications in the development of new and improved superconducting technologies.

Acknowledgements

Torino, April 2023

I am very grateful to my supervisor Luca Tocchio for having me guided and constantly supported in these months. His help, patience and hours of useful discussions, made this whole thesis possible.

I would also like to thank Vito for helping me learn how to run the simulations, interpret some of the results and make sense of them.

Computational resources were provided by HPC@POLITO.

Contents

Acronyms

μSR muon Spin Rotation. 36, 52

AF antiferromagnetic. 9, 10, 26, 29, 32, 33, 35, 39, 98

BCS Bardeen–Cooper–Schrieffer. 4, 17, 26, 84

DBC Detailed Balance Condition. 75

EM electromagnetic. 61

FS Fermi Surface. 28

HTSC high-temperature superconductor. 27

HTSCs high-temperature superconductors. 4, 26, 36, 37, 41, 45, 112

LBCO $La_{2-x}Ba_xCuO_4$. 46

LSCO $La_{2-x}Sr_xCuO_4$. 28, 34, 39, 46, 49

LTO low-temperature orthorhombic. 29, 46, 47

LTT low-temperature tetragonal. 46, 47

MC Monte Carlo. 72, 83, 92

MCMC Markov Chain Monte Carlo. 74

MIT Metal-Insulator Transition. 9, 12

NMR Nuclear Magnetic Resonance. 52

PD Photon Detector. 66

QMC Quantum Monte Carlo. 68

r.l.u. reciprocal lattice units. 41

RXS Resonant X-Ray Scattering. 49, 52, 60, 61, 63–67

VMC Variational Monte Carlo. 68, 91, 109

XAS X-Ray Absorption. 65

XRD X-Ray Diffraction. 63–65, 67

Chapter 1

Highly-correlated Electron Systems and Cuprates

The conventional quantum theory of electronic structure of solids, known as "Fermi liquid theory", which successfully describes the properties of many good electrical conductors and semiconductors, treats the electrons in the material as a gas of weakly interacting particles and the electron-electron interactions are mostly analyzed at the mean-field level.

If the interaction term is small compared to the kinetic energy or, in other words, if the Coulomb repulsion U resulting from the intra-atomic electron-electron interaction is small compared to the bandwidth W[1] determined by the hopping amplitude, approximations such as the Hartree-Fock approach are considered to be adequate. In this scenario, the band structure and single-particle state spectrum can be determined using a one-particle potential that includes exchange. The corrections beyond this approximation, known as correlation contributions, can be treated as weak perturbations when U is much smaller than W.

This is not always the case in physically realistic systems, as the bandwidth

[1]The bandwidth W is defined as the energy difference between the highest and lowest energy levels in the band, namely $W = E_{max}(\mathbf{k}) - E_{min}(\mathbf{k})$.

and Coulomb repulsion can have comparable energy scales, or the Coulomb repulsion can even be greater, making them *strongly correlated systems*. Strong enough Coulomb repulsion can also result in magnetic order in electron systems, that cannot be described by the single-particle picture with spin-split bands, leading to challenges in the theoretical description of antiferromagnetic (AF) states (developed where a nonzero average magnetic moment on each site appears in a direction that alternates from site to site) in itinerant electron systems with a half-filled band [1]. This can result in the Mott Metal-Insulator Transition (MIT), which is one of the topics explored in this chapter.

1.1 The Mott Metal-Insulator Transition

The transition from a metallic to an insulating phase can sometimes be explained in terms of conventional band theory.

For instance, consider an element with an even number of electrons per unit cell. Due to the fact that the number of states in a band is twice the number of elementary cells, materials that have an even number of electrons per unit cell and crystallize in structures with a monoatomic unit cell should have completely filled or empty bands unless there is an energy overlap between the bands. This overlap of bands is what makes divalent elements of the second group in the periodic table metals.

As the distance between atoms increases, the overlap between the wave functions of neighboring atoms decreases and the bands become narrower. Once the atoms are brought very far apart, they become independent and the atomic energy levels are recovered. The narrowing of the bands is displayed in Fig. 1.1.

When the overlap between the bands reaches zero at a critical value of the interatomic distance, the lower band becomes completely filled and the upper band becomes empty, resulting in an insulating state. For smaller lattice parameters, instead, the material remains metallic.

This type of metal-nonmetal transition that occurs when the lattice parameter is altered (for example, by applying pressure) is known as *band-overlap* or

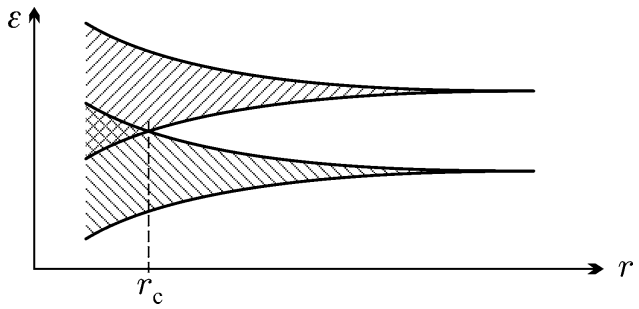

Figure 1.1: Variation of the bandwidth as a function of the distance between the atoms [1].

Wilson transition, named after A.H. Wilson (1931). The resulting insulating state is referred to as a *band insulator* or *Bloch-Wilson insulator*. The interaction with the periodic one-particle potential plays a dominant role in the formation of bands and this transition can be explained within the one-particle picture without taking into account the electron-electron interaction.

Naively, according to the predictions of the one-particle band picture, one would expect systems with an odd number of electrons per atom to be always metals. In reality, however, this is not the case.

For example, NiO is not a metal despite having an odd number of electrons, as the Ni^{2+} ion has eight $3d$ electrons but the band states cannot by filled by eight electrons in order to get a full band and an empty one. This cannot be explained by antiferromagnetic ordering, as NiO is insulating even in the paramagnetic phase. Similarly, in CoO, a transition from a paramagnetic insulator to an antiferromagnetic insulator is observed with an odd number of d electrons.

Another example is V_2O_3, which undergoes a first-order phase transition from an AF insulating state to a metallic state. The conductivity changes abruptly by several orders of magnitude. The phase diagram becomes even more complex when pressure is changed; this is done in practice by doping the material with atomic species that have a larger/smaller atomic size, effectively varying the lattice constants. In this case, three phases are found: a paramagnetic metallic phase, a paramagnetic insulating phase, and an antiferromagnetic insulating

phase.

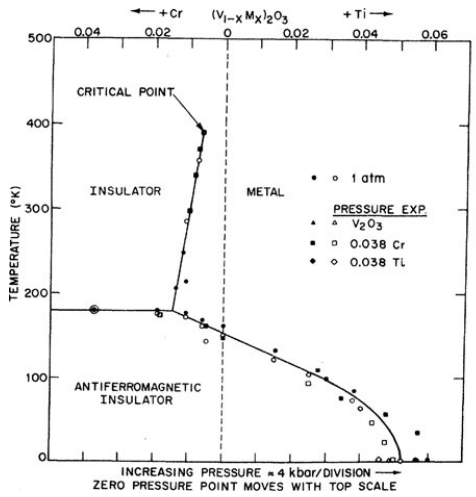

Figure 1.2: Temperature vs Pressure phase diagram of V_2O_3, doped with Cr and Ti at concentration x. The pressure is decreased by replacing V with Cr atoms, that have a larger atomic size. Ti-doping, on the other hand, results in an increased pressure, allowing electrons to move easier and hence the system enters the metallic phase. The vertical dashed line indicates the ambient pressure (or undoped material). From D. B. McWhan *et al.*, Phys. Rev. B 7, 1920 (1973).

N. F. Mott proposed in 1949 that the correlation between electrons can open a further gap within the conducting Bloch band and resulting in an insulating state. Indeed, in the Bloch picture the electron-electron repulsion is not considered, meaning that electrons described for instance by plane waves and with momenta $\mathbf{k}$ and $\mathbf{k}'$ have equal probabilities of being located at any point in the Bravais lattice, even on the same site. However, the Coulomb repulsion should prevent this from happening. As a result, Mott suggested that the actual density of states in real bands is different from what is predicted by Bloch theory due to the presence of electron-electron repulsion.

If the distance between atoms decreases and the bands widen, a sudden and abrupt (first-order) transition from insulating and strongly correlated to metallic and weakly correlated behavior is expected. This *Mott transition* occurs as a

result of changes in the ratio U/W due to variations in temperature or pressure, or changes in dopant concentration.

The mechanism is illustrated in Fig.1.3.

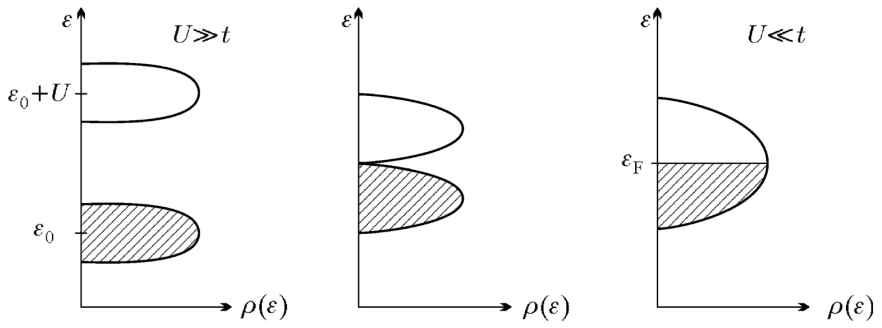

Figure 1.3: Density of states $\rho(\epsilon)$ as the on-site Coulomb interaction strength U increases, from right to left.

As the interaction increases, starting from the Bloch band (rightmost subplot), the density of states first shows a minimum at the band center (central subplot), dividing it into a lower energy sub-band (consisting of singly occupied Wannier states) and a higher energy sub-band (with some doubly occupied Wannier states). Beyond a critical interaction level, the minimum in density of states vanishes and the two sub-bands become separated by an energy gap in two distinct bands (as seen in the left part of the figure). At half-filling, the lower energy band is completely filled and the higher energy band is empty, resulting in an insulating state.

1.2 The Hubbard model

The Hubbard Model (1963), named after J. Hubbard, is a model that includes the interaction between electrons and allows to take into account the eventual magnetic behavior of the electron system. It was specifically derived in order to explain the MIT transition.

In the Fock space built on Wannier functions, the single particle Wannier

states are labeled by the sites of the Bravais lattice, and they overlap less and less as the sites are far apart.

In second quantization, the creation operator for an electron on the site $\mathbf{R}_j$ is given by

$$c^\dagger_{\mathbf{R}_j\sigma} = \frac{1}{\sqrt{N}} \sum_{\mathbf{k}} e^{-i\mathbf{k}\cdot\mathbf{R}_j} c^\dagger_{\mathbf{k}\sigma}, \tag{1.1}$$

where $c^\dagger_{\mathbf{k}\sigma}$ creates a Bloch electron with momentum $\mathbf{k}$ and spin σ. This allows us to write the one-body part of the electron Hamiltonian in its tight-binding form

$$H^{(1)}_{el} = \sum_{\mathbf{R}\mathbf{R}'\sigma} t_{\mathbf{R}\mathbf{R}'} c^\dagger_{\mathbf{R}_j\sigma} c_{\mathbf{R}'_j\sigma} \tag{1.2}$$

where

$$t_{\mathbf{R}\mathbf{R}'} = \int d^3r \phi^*(\mathbf{r}-\mathbf{R}) H(\mathbf{r}) \phi(\mathbf{r}-\mathbf{R}') \tag{1.3}$$

is the overlap integral, and $\phi(\mathbf{r}-\mathbf{R})$ the Wannier functions centered on $\mathbf{R}$.

The electron-electron interaction, written also in real space, becomes

$$H^{(2)}_{el} = \frac{1}{2} \sum_{\mathbf{R}_1\mathbf{R}_2\mathbf{R}'_1\mathbf{R}'_2\sigma_1\sigma_2} V_{\mathbf{R}_1\mathbf{R}_2\mathbf{R}'_1\mathbf{R}'_2} c^\dagger_{\mathbf{R}'_1\sigma_1} c^\dagger_{\mathbf{R}'_2\sigma_2} c_{\mathbf{R}_2\sigma_2} c_{\mathbf{R}_1\sigma_1} \tag{1.4}$$

with[2]

$$V_{\mathbf{R}_1\mathbf{R}_2\mathbf{R}'_1\mathbf{R}'_2} = \frac{e^2}{4\pi\epsilon_0} \int d^3r d^3r' \phi^*(\mathbf{r}-\mathbf{R}'_1)\phi^*(\mathbf{r}'-\mathbf{R}'_2) \frac{e^{-q_{TF}|\mathbf{r}-\mathbf{r}'|}}{|\mathbf{r}-\mathbf{r}'|} \phi(\mathbf{r}'-\mathbf{R}_1)\phi(\mathbf{r}-\mathbf{R}_2) \tag{1.5}$$

In the simplest form of the Hubbard model, only the Wannier states located at $\mathbf{R}_1 = \mathbf{R}_2 = \mathbf{R}'_1 = \mathbf{R}'_2$ are taken into account, since their contribution is dominant.

Upon identifying $\mathbf{R}_j \to j$, the electron-electron interaction Hamiltonian of Eq.1.4 is rewritten as

$$H^{(2)}_{el} = \frac{1}{2} \sum_{j_1,j_2,j'_1,j'_2,\sigma_1,\sigma_2} V_{j_1,j_2,j'_1,j'_2} c^\dagger_{j'_1\sigma_1} c^\dagger_{j'_2\sigma_2} c_{j_2\sigma_2} c_{j_1\sigma_1}. \tag{1.6}$$

[2]Here, e is the elementary charge, ϵ_0 the dielectric constant, and the potential includes the Thomas-Fermi screening effect.

As a further simplification, only the hopping among adjacent sites (with nearest-neighbours denoted by $\langle \dots \rangle$ and next-nearest-neighbours by $\langle\langle \dots \rangle\rangle$) is kept. Explicitly,

$$t_{j,j'} = \begin{cases} -t & \text{for } \langle j, j' \rangle \\ -t' & \text{for } \langle\langle j, j' \rangle\rangle \\ 0 & \text{otherwise} \end{cases}. \tag{1.7}$$

By keeping only the terms for $j = j_1 = j_2 = j'_1 = j'_2$, noticing that the only choice $\sigma_2 = -\sigma_1$ amounts to a non-vanishing contribution (since we cannot annihilate twice the same spin on a given site) and defining $U = V_{j_1,j_2,j'_1,j'_2}$, we obtain the celebrated Hamiltonian of the Hubbard model

$$H = -t \sum_{\langle j,j' \rangle,\sigma} c^\dagger_{j\sigma} c_{j'\sigma} + \frac{U}{2} \sum_{j,\sigma} c^\dagger_{j\sigma} c^\dagger_{j(-\sigma)} c_{j(-\sigma)} c_{j\sigma}. \tag{1.8}$$

The second term can be rewritten as follows:

$$\sum_{j,\sigma=\{\uparrow,\downarrow\}} c^\dagger_{j\sigma} c^\dagger_{j(-\sigma)} c_{j(-\sigma)} c_{j\sigma} = c^\dagger_{j\uparrow} c^\dagger_{j\downarrow} c_{j\downarrow} c_{j\uparrow} + c^\dagger_{j\downarrow} c^\dagger_{j\uparrow} c_{j\uparrow} c_{j\downarrow} \tag{1.9}$$

$$= n_{j\uparrow} n_{j\downarrow} + n_{j\downarrow} n_{j\uparrow} = 2 n_{j\uparrow} n_{j\downarrow} \tag{1.10}$$

in order to obtain the final result:

$$\boxed{H = -t \sum_{\langle j,j' \rangle,\sigma} c^\dagger_{j\sigma} c_{j'\sigma} + U \sum_j n_{j\uparrow} n_{j\downarrow}}. \tag{1.11}$$

To gain insight into the physics of the model, we first consider the scenario where the number of electrons is equal to the number of lattice sites (half-filling). The interaction between electrons is treated in the mean-field approximation, which is reasonable for weak couplings where $U \ll t$. In this picture, the electrons fill half of a band, resulting in a metallic system. Conversely, when $U \gg t$, the half-filled Hubbard model is equivalent to an antiferromagnetic Heisenberg model with exchange coupling $J = -2t^2/U$. In this case, spins can be exchanged, but electrons cannot carry current, leading to an insulating system. Due to the strong on-site repulsion, if an electron hops to a neighboring site, double occupancy occurs only briefly, and one of the electrons must hop back

to the temporarily empty site. The $t - J$ model, which is a further simplification, keeps the kinetic energy term, adds a Heisenberg interaction between neighboring spins, and considers Coulomb repulsion by excluding states with double occupancy.

Since the Hamiltonian captures in the two limits both the metallic and the insulating behavior, it was proposed as a candidate to describe an interaction induced phase transition from a metallic to a Mott insulating phase.

1.3 Conventional Superconductivity

The electrical resistivity of metals decreases as the temperature is lowered. In an ideal crystal without any impurities or inhomogeneities, the contribution of lattice vibrations to the resistivity would vanish at zero temperature, resulting in a null resistivity. However, in real samples, the presence of impurities and inhomogeneities leads to finite transport relaxation times for electrons even at $T = 0$, causing a finite conductivity $\sigma = n_e e^2 \tau / m_e$ according to the prediction of the Drude model[3]. The liquefaction of helium in 1908 made it possible to study the metal resistivity at much lower temperatures than before. In 1911, *H. Kamerlingh Onnes* found that the resistivity of pure mercury dropped suddenly to a very low value, practically zero within experimental error, around $T = 4.2$K, which is known as the liquid-helium temperature. The remarkable discovery is shown in Fig.1.4.

This result was unexpected[4] and later confirmed for a broad class of metals, which show a similar behavior. These metals do not have a gradual decrease in resistivity with temperature but, instead, their resistivity drops suddenly to zero at a finite critical temperature, T_c. This phenomenon was named *supercon-*

[3]In the (classical) Drude theory of transport, n_e is the density of conduction electrons, e the elementary charge, τ the average time interval between two collision events, m_e the electron mass.

[4]Indeed one might wonder which one between the scattering amplitude and the electron mobility would first drop to zero first as the temperature decreases (leading to no resistivity in the former case and no conductivity in the latter).

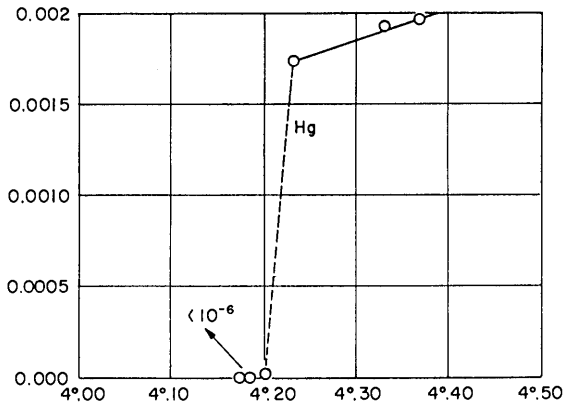

Figure 1.4: Temperature dependence of the resistivity of mercury at low temperatures, as measured by Kamerlingh Onnes *[Comm. Phys. Lab. Univ. Leiden, No. 120b (1911)]*[2].

ductivity and the materials were referred to as *superconductors* by Kamerlingh Onnes [2].

The critical temperature of superconductivity typically observed is much lower than the temperatures at which magnetic ordering or density-wave states occur. Superconductivity can be easily disrupted by a thermal energy of just a few millielectron volts, which suggests that the interaction responsible for this phenomenon is much weaker than the dominant interactions (Coulomb repulsion or exchange) in electronic systems. This led H. Fröhlich and J. Bardeen to propose in 1950 that superconductivity could be due to electron-phonon interaction. The discovery of the isotope effect the same year confirmed that ions and their vibrations play an important role in superconductivity.

The emission of a phonon by one electron and its absorption by another can be seen as a direct interaction between the two electrons.

This interaction, mediated by phonons, is attractive when the electrons are close to the Fermi surface within a range determined by the width of $2\hbar\omega_D$ in the phonon spectrum. From a pictorial point of view, the first electron causes a deformation and polarization in the lattice that attracts the other

electron. If this attraction is strong enough, it can overcome the repulsive Coulomb interaction between the electrons. On the other hand, contributions from electrons further away from the Fermi energy, where the interaction is repulsive, can be disregarded.

These concepts are applicable to conventional superconductors where the attraction between electrons is caused by phonon-mediated interactions even if also other mechanisms, such as magnetic interactions, can generate attraction between electrons.

In 1956, *L. N. Cooper* made a significant contribution to the understanding of superconductivity by showing that if the potential between two electrons is attractive, no matter what is its origin, a bound state of two electrons, called **Cooper pair**, can be formed when they move through a Fermi sea that is already filled.

Under these circumstances the pairs are formed not one by one, but instead the entire Fermi sea becomes unstable below a critical temperature T_c. This new state, known as the superconducting state, has completely different properties from those of the Fermi system. The non-analyticity of the binding energy of the Cooper pairs in relation to the interaction potential highlights that the superconducting state cannot be obtained through perturbation theory from the non-interacting Fermi sea.

1.3.1 The BCS Theory

The development of the BCS theory [3], the microscopic theory of superconductivity, named after J. Bardeen, L. N. Cooper, and J. R. Schrieffer, was made possible in 1957 due to the discovery of the instability of the electron gas in forming Cooper pairs. The role of singlet Cooper pairs is assumed dominant, and only those processes involving singlet pairs with total momentum zero scattered into singlet pairs are considered[5]. The Hamiltonian acting on the reduced

[5]The restriction to singlet pairs alone is not acceptable in the superfluid phase of ^{3}He. Additionally, experimental data supports the existence of triplet pairs in certain unconventional superconductors.

Hilbert space of the $\mathbf{K} = \mathbf{k} + \mathbf{k}' = 0$ singlet pair states is

$$\mathcal{H}_{BCS} = \sum_{\mathbf{k}} \epsilon_{\mathbf{k}} (c^{\dagger}_{\mathbf{k}\uparrow} c_{\mathbf{k}\uparrow} + c^{\dagger}_{-\mathbf{k}\downarrow} c_{-\mathbf{k}\downarrow}) + \sum_{\mathbf{k},\mathbf{k}'} V_{\mathbf{k},\mathbf{k}'} c^{\dagger}_{\mathbf{k}\uparrow} c^{\dagger}_{-\mathbf{k}\downarrow} c_{-\mathbf{k}'\downarrow} c_{\mathbf{k}'\uparrow}, \tag{1.12}$$

where the interaction $V_{\mathbf{k},\mathbf{k}'}$ in most cases only weakly depends on $\mathbf{k}$ and $\mathbf{k}'$, since only electrons near the Fermi surface are involved in the creation of Cooper pairs. $\epsilon_{\mathbf{k}}$ is the electronic dispersion relation.

A further crucial assumption of the BCS theory is that all electrons in superconductors are paired as Cooper pairs in the ground state. This means that if a state with wave vector $\mathbf{k}$ and spin $\uparrow$ is occupied, the state with wave vector $-\mathbf{k}$ and spin $\downarrow$ will also be occupied. This requirement is fulfilled by the ground state of a non-interacting Fermi gas, of the form

$$|\Psi_{FS}\rangle = \prod_{|\mathbf{k}|<k_F} c^{\dagger}_{\mathbf{k}\uparrow} c^{\dagger}_{-\mathbf{k}\downarrow} |0\rangle , \tag{1.13}$$

where $|0\rangle$ is the vacuum state of electrons.

The electrons are unable to take advantage of the attractive interaction between them because there are no available empty states for them to be scattered into elastically. If the momentum distribution function has a smoothed out discontinuity, meaning that there are empty states below the chemical potential and filled states above it, the kinetic energy increases compared to the ground state of free electrons. However, this increase can be offset by the binding energy of the Cooper pairs. It may be energetically favorable for the system to transition to a new state where the distribution function is smoothed over a finite energy range, but all electrons are still bound into pairs through the attractive effective interaction.

According to the BCS theory, the ground state of a superconductor is a coherent linear combination of states that consist of Cooper pairs with all possible wave vectors $\mathbf{k}$ that, for N_e electrons, would look like

$$|\Psi_{N_e}\rangle = \sum_{\mathbf{k}_1,\ldots,\mathbf{k}_{N_e/2}} \alpha_{\mathbf{k}_1} \ldots \alpha_{\mathbf{k}_{N_e/2}} c^{\dagger}_{\mathbf{k}_1\uparrow} c^{\dagger}_{-\mathbf{k}_1\downarrow} \ldots c^{\dagger}_{\mathbf{k}_{N_e/2}\uparrow} c^{\dagger}_{-\mathbf{k}_{N_e/2}\downarrow} |0\rangle , \tag{1.14}$$

but calculations are made feasible by choosing a simpler, variational wavefunction explicitly written as a superposition of states where pairs $(\mathbf{k}\uparrow, -\mathbf{k}\downarrow)$

are either occupied or empty, for every possible value of $\mathbf{k}$. This gives the *BCS Ansatz*

$$\boxed{|\Psi_{BCS}\rangle = \prod_{\mathbf{k}} (u_{\mathbf{k}} + v_{\mathbf{k}} c^{\dagger}_{\mathbf{k}\uparrow} c^{\dagger}_{-\mathbf{k}\downarrow}) |0\rangle}. \tag{1.15}$$

The quantities $u_{\mathbf{k}}$ and $v_{\mathbf{k}}$ are variational parameters to be minimized in order to find the ground state energy. Their moduli $|v_{\mathbf{k}}|^2$ and $|u_{\mathbf{k}}|^2$ represent respectively, according to the probabilistic interpretation of the wavefunction, the probability of having or not having the pair associated to the momentum $\mathbf{k}$ in the system. To ensure the normalization constraint $\langle \Psi_{BCS} | \Psi_{BCS} \rangle = 1$, the relation

$$|u_{\mathbf{k}}|^2 + |v_{\mathbf{k}}|^2 = 1 \tag{1.16}$$

has to be satisfied. It is worth pointing out that Eq.1.15 reduces to the the wavefunction of the normal metal of Eq.1.13 in the particular case in which

$$\begin{cases} u_{\mathbf{k}} = 0, \quad v_{\mathbf{k}} = 1 \text{ for } k < k_f \\ u_{\mathbf{k}} = 1, \quad v_{\mathbf{k}} = 0 \text{ for } k > k_f \end{cases}. \tag{1.17}$$

From a practical point of view, being the number of electrons not fixed in Eq.1.15, it is sometimes convenient to move to the grand canonical ensemble. This can be done by considering the total number of particles

$$N = \sum_{\mathbf{k},\sigma} c^{\dagger}_{\mathbf{k}\sigma} c_{\mathbf{k}\sigma} = \sum_{\mathbf{k}} (c^{\dagger}_{\mathbf{k}\uparrow} c_{\mathbf{k}\uparrow} + c^{\dagger}_{-\mathbf{k}\downarrow} c_{-\mathbf{k}\downarrow}), \tag{1.18}$$

taking into account the chemical potential μ, and redefining the BCS Hamiltonian of Eq.1.12 as

$$\mathcal{H}_{BCS} \rightarrow \mathcal{H}_{BCS} - \mu N, \tag{1.19}$$

leading to

$$\boxed{\mathcal{H}_{BCS} = \sum_{\mathbf{k}} \xi_{\mathbf{k}} (c^{\dagger}_{\mathbf{k}\uparrow} c_{\mathbf{k}\uparrow} + c^{\dagger}_{-\mathbf{k}\downarrow} c_{-\mathbf{k}\downarrow}) + \sum_{\mathbf{k},\mathbf{k}'} V_{\mathbf{k},\mathbf{k}'} c^{\dagger}_{\mathbf{k}\uparrow} c^{\dagger}_{-\mathbf{k}\downarrow} c_{-\mathbf{k}'\downarrow} c_{\mathbf{k}'\uparrow}}, \tag{1.20}$$

with $\xi_{\mathbf{k}} = \epsilon_{\mathbf{k}} - \mu$ being the energy of the electrons measured with respect to the chemical potential[6].

[6]It is straightforward to show that, by computing $Var(N)$, the discrepancy between the

At the very root of the BCS approach, the variational wavefunction of Eq.1.15 is used to find a variational estimate of the ground state energy. By defining the superconducting parameter

$$\Delta_{\mathbf{k}} = -\sum_{\mathbf{k}'} V_{\mathbf{k},\mathbf{k}'} \langle c^{\dagger}_{\mathbf{k}'\uparrow} c^{\dagger}_{-\mathbf{k}'\downarrow} \rangle = -\sum_{\mathbf{k}'} V_{\mathbf{k},\mathbf{k}'} u'_{\mathbf{k}} v'_{\mathbf{k}}, \tag{1.21}$$

where $\langle \dots \rangle = \langle \Psi_{BCS} | \dots | \Psi_{BCS} \rangle$, one can show that, in minimizing $\langle \Psi_{BCS} | \mathcal{H}_{BCS} | \Psi_{BCS} \rangle$, the variational parameters of the BCS wavefunction are given by

$$u^2_{\mathbf{k}} = \frac{1}{2}\left(1 + \frac{\xi_{\mathbf{k}}}{E_{\mathbf{k}}}\right) \tag{1.22}$$

$$v^2_{\mathbf{k}} = \frac{1}{2}\left(1 - \frac{\xi_{\mathbf{k}}}{E_{\mathbf{k}}}\right), \tag{1.23}$$

with

$$E_{\mathbf{k}} = \sqrt{\xi^2_{\mathbf{k}} + \Delta^2_{\mathbf{k}}}. \tag{1.24}$$

The Eq.1.20 can be simplified to a mean-field problem whose Hamiltonian is given, discarding constant terms, by

$$\mathcal{H}^{MF}_{BCS} = \sum_{\mathbf{k},\sigma} \xi_{\mathbf{k}} c^{\dagger}_{\mathbf{k}\sigma} c_{\mathbf{k}\sigma} + \sum_{\mathbf{k},\mathbf{k}'} V_{\mathbf{k},\mathbf{k}'} \left(\langle c^{\dagger}_{\mathbf{k}\uparrow} c^{\dagger}_{-\mathbf{k}\downarrow} \rangle c_{-\mathbf{k}'\downarrow} c_{\mathbf{k}'\uparrow} + c^{\dagger}_{\mathbf{k}\uparrow} c^{\dagger}_{-\mathbf{k}\downarrow} \langle c_{-\mathbf{k}'\downarrow} c_{\mathbf{k}'\uparrow} \rangle \right) \tag{1.25}$$

which becomes

$$\mathcal{H}^{MF}_{BCS} = \sum_{\mathbf{k},\sigma} \xi_{\mathbf{k}} c^{\dagger}_{\mathbf{k}\sigma} c_{\mathbf{k}\sigma} + \sum_{\mathbf{k}} (\Delta_{\mathbf{k}} c_{-\mathbf{k}\downarrow} c_{\mathbf{k}\uparrow} + \Delta^{*}_{\mathbf{k}} c^{\dagger}_{\mathbf{k}\uparrow} c^{\dagger}_{-\mathbf{k}\downarrow}) \tag{1.26}$$

upon substituting the definition for $\Delta_{\mathbf{k}}$.

Given the expressions for $u^2_{\mathbf{k}}$ and $v^2_{\mathbf{k}}$, a set of self-consistent equations for the parameters $\Delta_{\mathbf{k}}$ is found

$$\Delta_{\mathbf{k}} = -\frac{1}{2} \sum_{\mathbf{k}'} \frac{\Delta_{\mathbf{k}'}}{E_{\mathbf{k}'}} V_{\mathbf{k},\mathbf{k}'}. \tag{1.27}$$

Under the hypothesis of having

$$V_{\mathbf{k}\mathbf{k}'} = \begin{cases} -V/\Omega & \text{for } |\xi_{\mathbf{k}}|, |\xi'_{\mathbf{k}}| < \hbar\omega_D \\ 0 & \text{otherwise} \end{cases}, \tag{1.28}$$

results obtained using a fixed number of particles and those calculated using the BCS wavefunction is extremely small.

the approximation

$$\Delta_{\mathbf{k}} = \begin{cases} \Delta_0 & \text{for } |\xi_{\mathbf{k}}| < \hbar\omega_D \\ 0 & \text{otherwise} \end{cases} \tag{1.29}$$

follows and the self-consistency equations become easily solvable by replacing the sum over the momenta by an integral over the energy, with the insertion of the density of states $g(E)$. Here, $V > 0$ is a constant, the minus sign in Eq.1.28 makes explicit the attractiveness of the potential, and Ω is the volume of the solid.

It is then possible to show that, as a final result,

$$\boxed{\Delta_0 \approx 2\hbar\omega_D e^{-1/Vg(E_F)}}, \tag{1.30}$$

with ω_D denoting the Debye cutoff frequency.

1.3.2 The gap parameter Δ

The mean-field analysis of the BCS Hamiltonian allows to compute the *condensation energy*, that is the energy difference between the superconductor and normal ground-state energies, and relate it to Eq.1.24. Indeed, $E_{\mathbf{k}}$ coincides to the energy of the quasiparticle excitations above the ground state (sometimes called *bogulons*[7]). This makes clear the role of the self-consistent parameter Δ as that of an energy gap. A nonzero value of Δ changes the spectrum with respect to that of a normal metal as shown in Fig.1.5.

The BCS approach considers the gap parameter to be independent of energy and only dependent on momentum $\mathbf{k}$. However, in actuality, $\Delta_{\mathbf{k}}$ can possess a nontrivial dependence on $\mathbf{k}$ due to the symmetry of the underlying lattice structure.

[7]This name derives from the Bogoliubov transformation involved in the discussion. Bogulons are related to the fermion operators $\gamma_{\mathbf{k}\sigma}$ and $\gamma^{\dagger}_{\mathbf{k}\sigma}$, representing the creation and annihilation of quasiparticles with wave vector $\mathbf{k}$ and spin σ of the correlated system (i.e. of the interacting electron gas where an appropriate attractive 2-body coupling is acting among electrons).

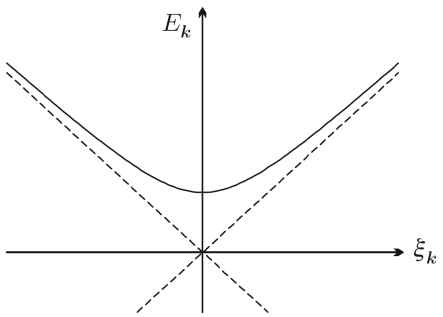

Figure 1.5: Spectrum of quasiparticles in the superconducting state [2] for the superconducting state *(solid line)* and normal metal *(dashed line)*. The value of the gap at $\xi_{\mathbf{k}} = 0$ is usually denoted by Δ_0.

For instance, in crystal structures with a center of inversion, it must either be even ($\Delta_{\mathbf{k}} = \Delta_{-\mathbf{k}}$) or odd ($\Delta_{-\mathbf{k}} = -\Delta_{\mathbf{k}}$) under inversion through the origin in $\mathbf{k}$ space. $\Delta_{\mathbf{k}}$ may not have the same sign everywhere on the Fermi surface and can result in regions of opposite sign being separated by nodal lines. Such states correspond to Cooper pairs with non-zero internal angular momentum, which is allowed by the point group symmetry of the lattice.

The symmetry of the superconducting gap function, whether even (such as s- or d-wave) or odd (p-wave), determines the spin of the Cooper pairs, which can either be a singlet or a triplet. An even orbital symmetry leads to a spin-singlet wave function, while an odd orbital symmetry leads to a spin-triplet wave function. However, the presence of a spin-orbit interaction limits the possibility of a mixture of singlet and triplet pair states.

In conclusion, the gap parameter is a well-defined quantity whose symmetry can be experimentally determined. The pair amplitude $\langle c^{\dagger}_{\mathbf{k}\uparrow} c^{\dagger}_{-\mathbf{k}\downarrow} \rangle$ encapsulates the essence of the macroscopic phase coherence in all superconducting states.

A few symmetries on the two-dimensional square lattice are reported in Fig.1.6. The s-wave symmetry is fully and isotropically gapped, whereas the $d_{x^2-y^2}$-wave and d_{xy}-wave symmetries exhibit along the Brillouin zone boundary in diagonal directions a gap which is identically zero for the former and

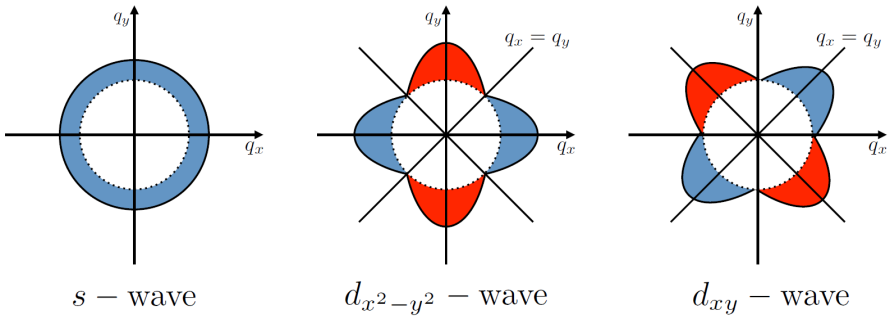

Figure 1.6: Symmetries of the gap parameter on the two-dimensional square lattice. The dashed line represents the Fermi surface, while the solid curves indicate the first excited states.

maximum for the latter. As will be discussed later on, the d-wave symmetry is a distinctive feature of unconventional superconductors, as for cuprates.

1.3.3 Gap equation and Critical Temperature

[8] Among the many fundamental results of the BCS theory, there is one very relevant in the discussion of the present work. The quantity $\Delta_{\mathbf{k}}$, representing the width of the forbidden region in the excitation spectrum, is directly related to the critical temperature T_c. At nonzero temperature, the quasiparticle states are thermally excited and a number of Cooper pairs is broken. Along to this process, the energy gap decreases, until eventually the system transitions to the normal metallic state. In conventional superconductors, the temperature dependence of the gap $\Delta(T)$ is found to follow a *universal behaviour*, as reported in Fig.1.7.

A mean-field approach at a temperature $T > 0$ of the BCS theory can account for this phenomenon. Indeed, one can express the product $c^\dagger_{\mathbf{k}\uparrow}c^\dagger_{-\mathbf{k}\downarrow}$ as

$$c^\dagger_{\mathbf{k}\uparrow}c^\dagger_{-\mathbf{k}\downarrow} = a_{\mathbf{k}} + (c^\dagger_{\mathbf{k}\uparrow}c^\dagger_{-\mathbf{k}\downarrow} - a_{\mathbf{k}}), \tag{1.31}$$

where $a_{\mathbf{k}} = \langle c^\dagger_{\mathbf{k}\uparrow}c^\dagger_{-\mathbf{k}\downarrow}\rangle_T$ is the thermal average and the second term the fluctu-

[8] For an exhaustive discussion, see [1].

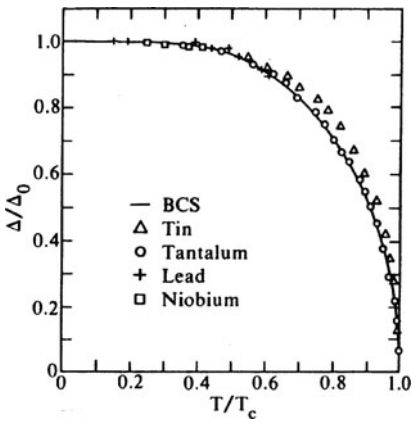

Figure 1.7: Values of the superconducting gap Δ normalized w.r.t. its value at zero temperature Δ_0 as a function of T, for different materials. From P. Townsend and J. Sutton, *Phys. Rev.* **128**, 591 (1962).

ation operator. The gap parameter is in this case defined as

$$\Delta_{\mathbf{k}} = -\sum_{\mathbf{k}'} V_{\mathbf{k}\mathbf{k}'} \langle c^{\dagger}_{\mathbf{k}\uparrow} c^{\dagger}_{-\mathbf{k}\downarrow} \rangle_T. \tag{1.32}$$

The complete mathematical derivation involves the introduction of the Bogoliubov canonical transformation, and leads to the following self-consistency equation

$$\Delta_{\mathbf{k}} = -\frac{1}{2} \sum_{\mathbf{k}'} V_{\mathbf{k}\mathbf{k}'} \frac{\Delta'_{\mathbf{k}}}{E'_{\mathbf{k}}} \tanh \frac{\beta E'_{\mathbf{k}}}{2} \tag{1.33}$$

where, again, $E_{\mathbf{k}} = \sqrt{\xi^2_{\mathbf{k}} + \Delta^2_{\mathbf{k}}}$. This last equation is a generalization at nonzero temperature of Eq.1.27 and reduces to it at zero temperature. By moving from a sum over momenta to an integral over the energy, under the same assumptions of the previous section (with the only difference of having $\Delta = \Delta(T)$), the gap equation at the critical temperature, where $\Delta = 0$, leads to

$$k_B T_c = \frac{2e^{\gamma}}{\pi} \hbar \omega_D e^{-1/Vg(E_f)}, \tag{1.34}$$

where γ is the Euler's constant and $\frac{2e^{\gamma}}{\pi} \approx 1.13$.

At this point, Eq.1.30 and Eq.1.34 can be used to get rid of the material-dependent parameters $g(E_f)$ and ω_D in order to obtain a single universal equa-

tion with no free parameters. This represents *the most fundamental result of the BCS theory*, directly connecting T_c and Δ_0

$$\boxed{\frac{\Delta_0}{2} = \frac{\pi}{2e^{\gamma}} k_B T_c \Rightarrow \frac{2\Delta_0}{k_B T_c} \approx 3.528}. \tag{1.35}$$

The agreement of the measured gap to the values predicted theoretically, for some superconductors, is reported in Fig.1.8. For many of them, the two values are rather close but however, for other materials the difference is appreciably different, pointing out the limitations of the BCS theory. Still, being able to measure a well-defined ratio even for these materials is a remarkable result.

Material	$2\Delta_0/k_{\mathrm{B}}T_{\mathrm{c}}$	Material	$2\Delta_0/k_{\mathrm{B}}T_{\mathrm{c}}$
Al	3.53	Hg	4.6
Cd	3.44	Pb	4.3
In	3.65	Os	4.8
Nb	3.65	Ir	5.6
Sn	3.59	$YBa_2Cu_3O_{7-\delta}$	4.0
Ta	3.63	$Bi_2Sr_2Ca_2Cu_3O_{10}$	5.7

Figure 1.8: The ratio $2\Delta_0/k_BT_c$ for some superconductors [1].

The reason why the BCS theory, which is essentially a mean-field theory, is so good at describing many fundamental features of conventional superconductors is that the effective coherence length of the Cooper pairs (or, in a sense, their size) ξ is usually 100 to 1000 times larger than the lattice constant a. If we consider a sphere with a radius approximately equal to the distance between two electrons forming a Cooper pair, this volume would likely contain around 10^6 other pairs[9]. This large number of pairs in the volume ensures that any fluctuations are smoothed out and effectively averaged.

[9]This is not the case for cuprates, being in fact unconventional superconductors.

1.4 High-temperature Superconductivity and Cuprates

[10] The discovery of superconductivity in layered copper-oxide compounds, by Bednorz and Müller in 1986 [6], has been surprising: first of all because of the highest transition temperature ever observed at that time (30K), as shown in Fig.1.9, but also since, in their "normal" (i.e. non-superconducting) state, they are insulators. The materials exhibiting *high-temperature superconductivity* are called high-temperature superconductors (HTSCs). Due to the low electron-phonon coupling constant[11] and the unexpected nature of the materials (transition-metal oxides), along with other unusual features such as the remarkable linearity of its resistivity at low temperatures above T_c and the k-dependent superconducting gap (d-wave pairing, see Fig.1.10), it became clear that a different mechanism was at play, distinct from the conventional superconductivity.

HTSCs are obtained from AF Mott insulators "parent" compounds (materials in which a strong electron-electron interaction generates both the antiferromagnetism and the insulating behaviour, as introduced before) that are electronically doped. Local magnetic correlations survive in the metallic compounds, hence it is appropriate to describe these materials as doped antiferromagnets. Since then, many families of compounds have been shown to exhibit superconductivity at high temperature.

1.4.1 Correlation Effects

In the standard theory of solids the kinetic energy of the electrons is considered the primary energy in the system, while the interactions between electrons and their effects are considered secondary. Indeed, their main behaviour is primarily determined by the reduction in total kinetic energy supported by a periodic potential, which enables the delocalization of local orbitals into extended wave-

[10] Main references: [4, 5]

[11] The upper limit for electron-phonon coupling, according to BCS theory, occurs at $T_c > 30$K

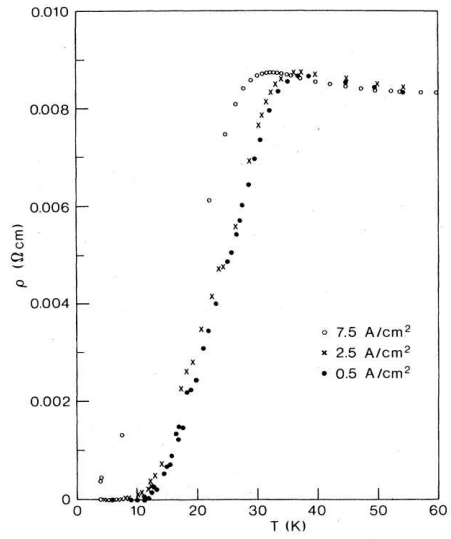

Figure 1.9: Behaviour of the resistivity of $Ba_xLa_{5-x}Cu_5O_{5(3-y)}$ as a function of temperature, at different current densities [6].

functions with a well-defined momentum (i.e. highly structured in momentum space). As a result of the uncertainty principle, the electronic states are highly homogeneous in real space.

The presence of a potential energy drives any eventual transition to a low-temperature ordered phase, inasmuch as it involves a gain in energy between electrons at a smaller cost of kinetic energy.

The mean free path l is a key concept in describing transport properties: it is defined as the distance travelled by an electron in between two consecutive scattering events. As long as l is much larger than λ_F, the de Broglie wavelength at the Fermi energy, it is well defined.

Many synthetic metals, among which also cuprate HTSCs, seem to violate this theory and the mean free path inferred from data by a conventional analysis is shorter than λ_F, implying an ill-defined momentum space. The main source of trouble relies in the nature itself of these materials: they are doped correlated insulators, in which the short-range repulsive interaction is not only a secondary

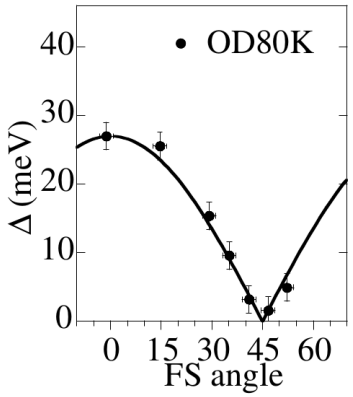

Figure 1.10: Superconducting gap Δ as a function of the angle along the Fermi Surface (FS) . Except at $k_y = \pm k_x$ (d-wave pairing), there is a finite gap protecting the ground state from the creation of excitations (photoexcited electrons). From J. Mesot *et al.*, PRL 83, 840 (1999).

effect, but the largest energy in the system.

However, the ground state of this part of the Hamiltonian is not unique, so the kinetic energy cannot simply be treated as a perturbation; such materials display substantial structure in both real space and momentum space. The conventional theory of Fermi liquids, as a consequence, must be abandoned. Neither the kinetic energy nor the potential energy is totally dominant, and they must be treated on an equal footing.

Also the very successful theory of superconductivity developed by Bardeen, Cooper and Schrieffer is no longer appropriate to describe high-temperature superconductivity in cuprates, being the original one designed to describe good metals and not doped insulators.

1.4.2 General features of cuprates

Among the uncountable number of cuprates, $La_{2-x}Sr_xCuO_4$, a layered cuprate with built-in broken symmetry (see Fig.1.11), is one of the most studied, as it shows superconductivity in a wide range of doping x (achieved by atomic

substitution of trivalent La with divalent Sr). Superconductivity develops in the CuO_2 planes, that have a square lattice geometry.

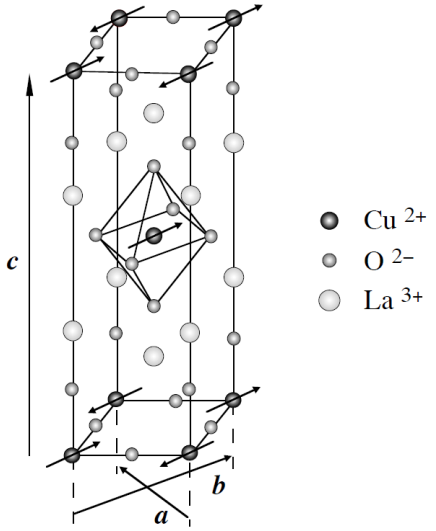

Figure 1.11: Atomic and magnetic structure of La_2CuO_4. Arrows indicate the orientation of the magnetic moments in the AF phase. The lattice parameters shown correspond to its low-temperature orthorhombic (LTO) crystal structure. The CuO_6 octahedron in the center of the cell is also reported [5].

The undoped ("parent") compound La_2CuO_4, i.e. with $x = 0$, has a layered perovskite structure, in which the crystalline environment for Cu atoms is tetragonal and it is an insulator with antiferromagnetic order in the CuO_2 plane. Each Cu has six O neighbours (see also Fig.1.13*(a)*), but with the octahedral arrangement elongated along the c axis, perpendicular to the planes.

Electronic structure

A closer look at the electronic structure of copper oxides allows one to see why these materials tend to become Mott insulators and explain why a single-orbital[12] Hubbard model is a good model.

[12]i.e. in which each site has only one place where at most two electrons can accommodate.

The role of the oxygen atoms located between each pair of copper atoms cannot be ignored in gaining a complete understanding of the situation.

The copper atom is a multi-orbital system with 9 electrons in five d-orbitals, as reported in Fig.1.12.

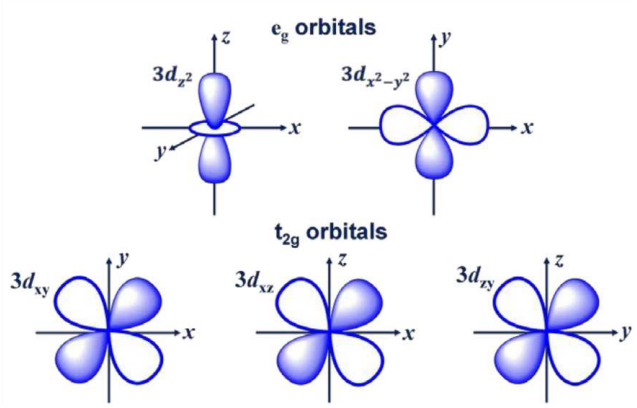

Figure 1.12: The five d-orbitals of Cu

In an undistorted lattice, the octahedral symmetry favours energetically the t_{2g} orbitals (see Fig.1.13*(c)*), that have lower Coulomb repulsion among the electrons in the d-orbitals and the oxygens, being further away from one another. This is not the case in Fig.1.13*(b)*, where the electrons in the $d_{x^2-y^2}$ orbital are closer to the oxygens and hence more energetically costly. When a lattice distortion along z is instead present, as in the case of cuprates, the d_{z^2} and $d_{x^2-y^2}$ levels split, being the d_{z^2} energetically favoured (Fig.1.13*(d)*).

As a result, among its 9 electrons, each Cu atom has one electron (consequently one hole) on each ion site in the d shell, in the $d_{x^2-y^2}$ orbital, effectively creating a half-filled orbital; because of its finite overlap with the p orbitals of the four neighboring O atoms in the CuO_2 planes, Wannier orbitals centered around the Copper atoms are created.

The illustration in Fig.1.14 shows the orbital radial charge densities at the typical Cu-O spacing and provides insight into the relationship between Cu and O. The strong overlap between the Cu $4s$ states and the O $2p$ states suggests

that these electrons can be treated as having been transferred to the O, resulting in a valence of 2− when the O $2p$ states are filled. On the other hand, the peak density of the Cu $3d$ states is located inside that of the $3p$ and $3s$ states, indicating strong Coulomb interactions between Cu $3d$ electrons. Furthermore, the significant overlap between the Cu $3d$ and O $2p$ orbitals results in significant hybridization.

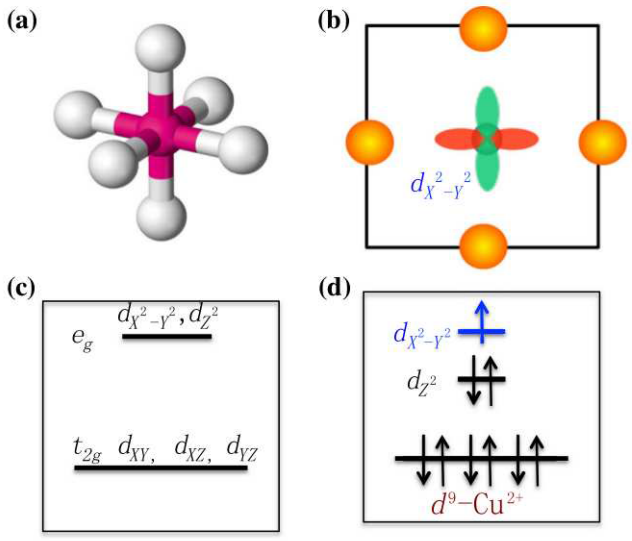

Figure 1.13: *(a)* Cu atom (in red) surrounded by six O (in white) in a octahedron structure. *(b)* Top view of a Cu orbital (central atom) and O (orange circles). *(c)* Energy levels in the undistorted structure. *(d)* A lattice distortion along the z axis splits the d_{z^2} and $d_{x^2-y^2}$ levels, creating an (effective) half-filling.

The behavior of Copper oxides at low energies is considered to be well represented by a single-band Hubbard model [7], due to a strong on-site repulsion that disfavors configurations with either no holes or two holes. This leads to a microscopic understanding in terms of the Hubbard model or its strong coupling version.

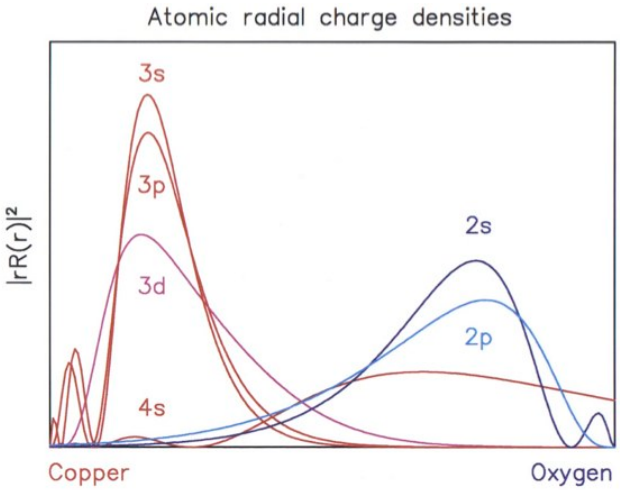

Figure 1.14: Radial charge densities for outer orbitals of Cu and O at a tipical Cu-O bond spacing [5].

Superexchange

The properties of the parent compound La_2CuO_4 have been explained by Anderson [8], who described it as a Mott insulator with superexchange driving AF correlations among Cu moments, rather than a "conventional" insulator in the sense of simple band theory. Indeed, according to conventional band structure calculations, La_2CuO_4 is expected to be metallic.

The concept of *superexchange* is here discussed for the simple Hubbard model, with a single orbital per Copper site (disregarding in this brief analysis the impact of the oxygen atoms) on a square lattice and nearest neighbour hopping only t. The conventional band theory focuses on the kinetic energy of electrons and the attempt of an electron to reduce its energy by hopping from one site to the next. The band width is equal to $8t$. The Hubbard model also considers the Coulomb repulsion U between two electrons on the same site. If U is larger than the band width, the electrons will tend to be localized on individual sites. Despite this, an electron can still reduce its kinetic energy by making virtual hops to a neighboring site and back (see Fig.1.15), but only if its spin

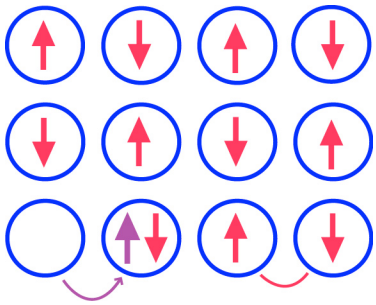

Figure 1.15: Schematic representation of the Hubbard model and the superexchange mechanism. The *hopping* process, indicated by the purple arrow has an energy "cost" $-t$; the double occupancy, disfavoured by the Coulomb repulsion, costs U; the AF configuration, indicated by the red line, has cost $J = 4t^2/U$. [5]

is antiparallel to that of the electron already on that neighboring site, due to Pauli exclusion principle. This results in an effective Heisenberg exchange energy between antiparallel spins, known as the superexchange energy $J = 4t^2/U$. This analysis suggests that the parent compound La_2CuO_4 should be classified, as experimentally observed, as an antiferromagnetic insulator.

Phase diagram for Cuprates

The phase diagram of this material, by varying doping and temperature, follows a universal pattern (see Fig.1.16) in which the long-range antiferromagnetic order is rapidly suppressed and ultimately disappears upon doping with holes or electrons, leading to the emergence of superconductivity. The metallic state above the superconducting one shows anomalous features that cannot be described by the Landau theory of Fermi liquids. Upon further doping, in the end, superconductivity disappears and a conventional metallic phase is established.

In the case of hole-doping, the maximum superconducting temperature T_c occurs for a hole doping $x \approx 0.16$. On the other side of the phase diagram, upon electron-doping, since the electronic correlations become even stronger,

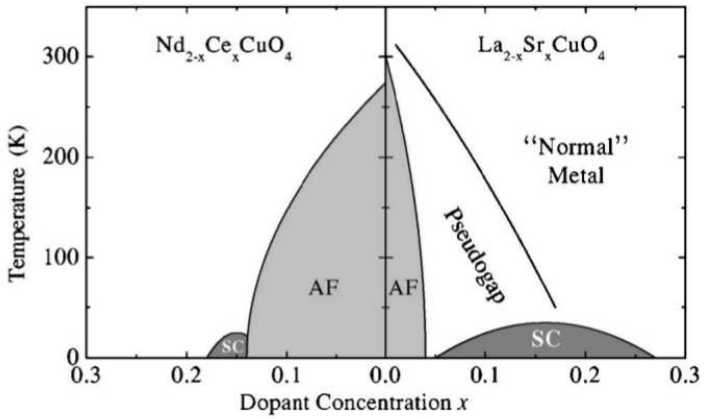

Figure 1.16: Phase diagram of $La_{2-x}Sr_xCuO_4$ for hole-doping, and $Nd_{2-x}Ce_xCuO_4$ for electron-doping, from [9]. AF = antiferromagnetic order, SC = superconducting order; in the pseudogap phase the density of states at the Fermi level in smaller than that predicted by conventional band theory.

the antiferromagnetic phase is more robust while the superconducting phase is reduced compared to the case of hole-doping. However, dynamic AF spin correlations are able to survive[13].

This rich behaviour is believed to be driven by the strong electron-electron correlations, as discussed before.

Suppression of Antiferromagnetism by hole-doping

The phase diagram in Fig.1.16 showed that hole doping x destroys the AF order, even for small values of x. It is worth investigating the nature of this destruction and looking for correlations that still survive[14].

As suggested in [7] by Zhang and Rice, an *effectively nonmagnetic site* is created in a CuO_2 plane when a hole (which has its own spin) forms a bound

[13] This will be discussed in more detail in Chapter 2.

[14] A comprehensive series of results and techniques can be found in [5]. Here only a few are reported.

singlet state with a Cu^{2+} ion. Magnetic correlations are affected by this bound hole in two ways: 1) the density of magnetic moments is reduced ("dilution"), and 2) the motion of the holes can also perturb the spins. Both the effects, effectively disrupt the magnetic order.

It is worth mentioning that dilution alone can be recreated and studied experimentally by preparing samples with a fraction z of Cu ions replaced by Zn and/or Mg. In [10] it is shown that, in a classical 2D antiferromagnet, the AF order is destroyed at the percolation[15] limit of $z \approx 0.41$.

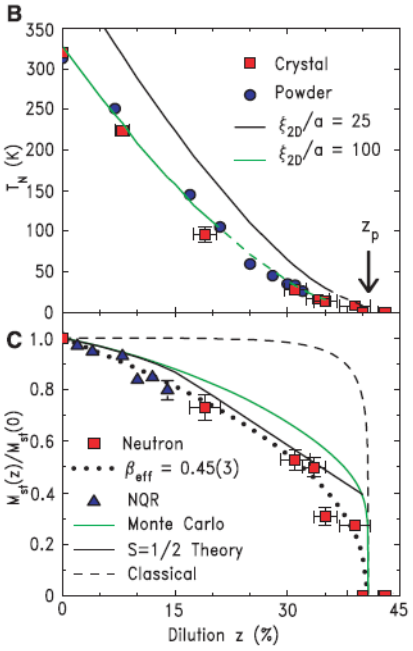

Figure 1.17: Impact of nonmagnetic dilution on AF order in $La_2Cu_{1-z}(Zn, Mg)_zO_4$, using different techniques and models. In the upper plot it is reported the Néel temperature T_N, while in the lower one the staggered moment per Cu normalized to $z = 0$.

The results from Vajk *et al.* [11] reported in Fig.1.17, show that: 1) the

[15] *Percolation* refers to the point at which a sufficient number of ions/holes are introduced into a system, such as a CuO_2 layer, that the magnetic order is destroyed

destruction of long-range order due to dilution occurs at the classical percolation limit, and 2) models that take into account quantum fluctuations capture the different, and reduced, ordered moment with respect to the classical prediction.

This clear shows that hole doping in CuO_2 layers has a greater impact than the dilution alone, since a much lower concentration of doping holes is enough to cause the same effects of a strong magnetic dilution.

Despite the long-range AF order being destroyed by a small density of holes, early studies demonstrated that, at low temperatures, local magnetic order can persist (see, for instance, the muon Spin Rotation (μSR) experiment from Niedermayer *et al.* [12].

In this regard, neutron scattering experiments, later discussed in Ch.2, are a primary tool to investigate the surviving correlations.

1.4.3 The Hubbard model for HTSCs

Models such as the Hubbard model to directly assess the impact of strong Coulomb interactions, are extremely important in particular when other methods like conventional density-functional calculations are unable to properly consider strong correlation effects.

The debate about the necessary complexity of a model to understand high-temperature superconductivity, with some advocating for a simple one-band model and others suggesting that a multi-band model is needed to capture all relevant degrees of freedom, is not settled. Multi-band Hubbard models taking into account multiple orbitals may be necessary to understand the rich behaviour of compounds such as La_2CuO_4. However, these models are challenging to solve and calculations beyond mean-field are limited to small clusters. It is common to start with a simpler 1-band Hubbard model focusing only on the Cu d-state and neglecting the impact of the oxygen atoms.

The inclusion of the next-nearest-neighbour hopping t', mentioned before, has been shown to be a relevant feature in all cuprates, as it constitutes an essential material-dependent parameter. Moreover, materials with higher transition

temperature T_c are associated to larger values of t' [13].

The previous discussion on the physical and electronic structure of cuprates, serves as a justification for the appropriateness of the single-band Hubbard model to describe them.

1.5 Stripe order and HTSCs

Doped antiferromagnets, belonging to the class of strongly correlated materials, are of particular importance and have been very well studied in the scientific literature over the years. Here, the parent compound is insulating, even at elevated temperatures, because of the strong short-range electron-electron repulsion.

The doping process considered is a *hole doping*, involving the removal of a small fraction of electrons from the insulating antiferromagnet. However, despite the charge distribution in a doped antiferromagnet being homogeneous, the added charges form clumps (predicted theoretically and later discovered experimentally) that constitute those called "topological defects", across which there is a change in phase of the background of spins. In particular, in one dimension these topological defects are solitons, in two dimensions linear "rivers of charge" and planes of charge when in three dimensions. More in general, for a generic d-dimensional system, the defects are $(d-1)$-dimensional objects. Such states tend to be insulating, even though they can exhibit a bad-metal character when thermally-disordered [4].

The importance of studying charge clustering and self-organization of topological defects resides in the large number of related systems in which they appear. Different forms of stripe formation show up, for instance, in Quantum Hall systems [14, 15], and in many other systems with competing interactions.

Hence, the electronic properties of synthetic metals, including their peculiar charge transport and superconducting properties, cannot be understood without a proper study of the formation of these spontaneously generated local structures.

1.5.1 Spin and Charge order in layered transition-metal oxides

In Sec.1.4.2 the general, and unconventional, features of cuprates have been discussed. The concept of a *stripe phase* is one of those features, that emerged over the years when interpreting a broad range of experimental results on copper-oxide superconductors and other systems closely related.

By *charge order* (or *charge-density-wave*) one refers to an electronic phase that breaks the translational symmetry of the underlying lattice, by self-organizing the electrons into periodic super-structures.

In general, the stripe order is an electronic ground state characterized by a combination of magnetic order and charge order with specific geometric constraints on the ordering wave vectors.

Once we allow holes to wander in an antiferromagnetic background, it becomes clearer that the creation of striped inhomogeneities can be a consequence. The reason for the self-organization of local inhomogeneities can be found in the competition between the tendency of the electrons to cluster in regions of suppressed antiferromagnetism [16], hence producing a short-range tendency to phase separation [17, 18, 19], and the long-range Coulomb interaction that instead frustrates it.

Striped states, reported in Fig.1.18, indeed constitute the best compromise between these competing phenomena and allow the doped holes to be delocalized along linear stripes, while the regions far from them remain more or less in the undoped correlated insulating state.

1.5.2 Theoretical Evidences

The impact of the hole motion was first analyzed by Trugman [20] for a 1-band Hubbard model (with nearest-neighbours hopping only). As shown in Fig.1.19, hole motion along a row of sites creates energetically-costly (with cost J, the exchange energy) ferromagnetic spin-correlations. In comparison, Fig.1.20 shows how a hole can effectively move diagonally by rotating around a square one

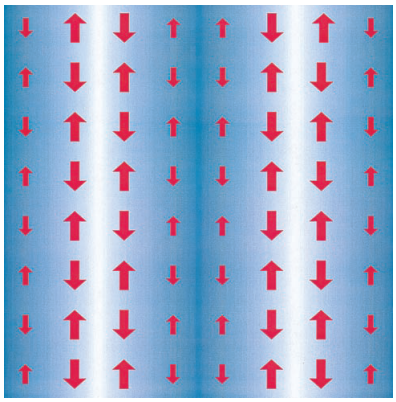

Figure 1.18: Schematic picture of a stripe-ordered phase [4]. Magnetic or spin order are represented by the arrows, while the local charge density is represented by the blue scale. Clusters of holes (stripes, in the dark-blue regions) lie between largely undoped regions behaving as in the undoped antiferromagnet.

and a half times. The first "rotation" creates costly ferromagnetic correlation (configuration 5), successively repaired after the next hopping events.

The first evidence of the possible development of an inhomogeneous state in a hole-doped cuprate layer came from the paper by Zaanen and Gunnarsson [21] thanks to a Hatree-Fock calculation on a 3-band Hubbard model. Their stripe solution is shown in Fig.1.21. A drawback of this particular solution is that the charge stripes have a density of one hole per copper site along the stripe, which leads to an insulating state and a spin periodicity that is half as large as what was observed in early measurements using inelastic neutron scattering on $La_{2-x}Sr_xCuO_4$. Stripe states that have a hole density of one-half per Cu site along the charge stripe, consistently with neutron and transport experiment, have been found in later studies. As justified in the following lines, it was expected that the stripe structure, with holes concentrated along rivers of charge-separating antiferromagnetic domains, would also be manifested as a periodic modulation of charge with a wave vector twice as long as that of the incommensurate AF peaks and linked to the hole concentration [22, 21].

It is fundamental to notice that, when crossing the hole stripe, there is a

Figure 1.19: Motion of one hole in an antiferromagnet. Starting from (a), the hole hops twice along a row (b) and causes spins to be flipped, creating energetically-costly ferromagnetic bonds, indicated by squiggles.[20]

shift in phase of the AF background by π (the so-called π-shift), as we proceed to illustrate with the following schemes. In absence of holes, the electrons (represented by their spin orientations $\{\uparrow,\downarrow\}$) in an AF pattern arrange themselves as follows

$$\uparrow \ \downarrow \ \uparrow \ \downarrow \ \uparrow \ \downarrow \ \uparrow \ \downarrow \ . \tag{1.36}$$

When a hole, represented by $\bigcirc$, is introduced somewhere, the situation changes

$$\boxed{\uparrow \ \downarrow \ \uparrow \ \underbrace{\downarrow \ \bigcirc \ \downarrow}_{\pi-\text{shift}} \ \uparrow \ \downarrow} \tag{1.37}$$

and two electrons with parallel spin end up being close to each other.

As a result, the presence of charge stripes disrupts the long-range antiferromagnetic order, however, the existence of periodic stripes can still result in a spin order.

Other evidences for spin and charge inhomogeneities came also from calculations on the $t-J$ model, indicating that doped holes would tend to phase separate [18] and the inclusion of extended Coulomb interactions should frustrate this phase separation [23], hence resulting in structures modulated in space, such as striped and checkerboard states.

All the studies in this regard identified a ground state with broken symmetry and short-range inhomogeneities in charge, arranged in an ordered pattern of one-directional arrays, separated from the magnetic domains and acting as

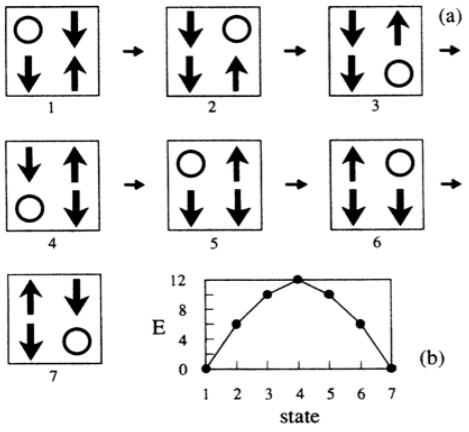

Figure 1.20: Motion of one hole in an antiferromagnet. (a) Going from configuration (1) to (7), that is by rotating around the square 1.5 times, we get a state degenerate with (1). (b) Plot of relative energy of each configuration in units of J.

boundaries for the latter.

The density of holes in the stripes is not fixed in principle, but it should correspond to the value that minimizes the free energy associated with the competing short- and long-range interactions.

1.5.3 Experimental Evidences

The scientific literature on the topic is extremely vast[16], as it reports a variety of experimental techniques on the even more vast family of HTSCs. In this section we report a few notable results.

Historically, the first evidence for stripe ordering came from neutron scattering experiments. The details on this commonly utilized technique to characterize the HTSCs will be discussed in Ch.2. From this point forward, we will utilize reciprocal lattice units (r.l.u.) as the unit of measurement for wave vectors in momentum space. The use of r.l.u. involves expressing wave vectors as $\mathbf{Q} = (H, K, L)$, corresponding to $\mathbf{Q} = (H \times 2\pi/a, K \times 2\pi/a, L \times 2\pi/a)$ in

[16] See for instance [24, 5, 25]

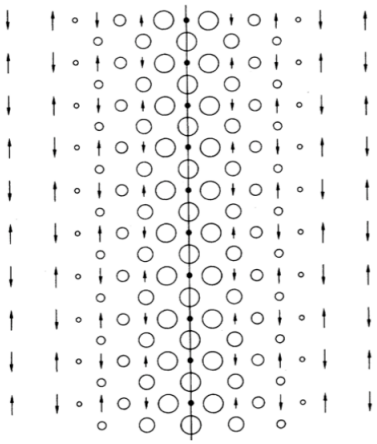

Figure 1.21: Stripe solution in a 3-band Hubbard model by Zaanen and Gunnarsson [21] by Hartree-Fock calculations.

physical units (with a denoting, as usual, the lattice constant).

The occurrence of AF order was first demonstrated for La_2CuO_4 by Vaknin *et. al.* [26]. The crystal structure for the copper atoms in a CuO_2 plane of La_2CuO_4, for both real and reciprocal space, is schematically represented in Fig.1.22.

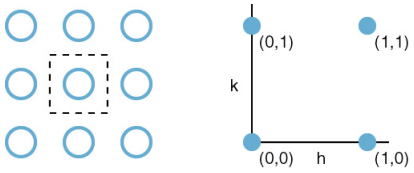

Figure 1.22: Crystal structure for the copper atoms in a CuO_2 plane of La_2CuO_4. *(Left):* real space; *(Right):* reciprocal space[5].

The Néel order with antiferromagnetism, found by looking at its magnetic structure, causes the unit cell to expand by a factor two in real space, which leads to the emergence of magnetic superlattice peaks, as shown in Fig.1.23. Therefore, the detection of the antiferromagnetic order can be accomplished by identifying these superlattice peaks. For an AF magnetic structure, these peaks

are located at the wave vectors $\mathbf{Q}_{AF} = \left(\pm\frac{1}{2}, \pm\frac{1}{2}, L\right)$.

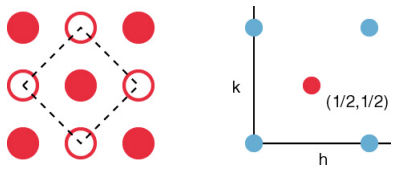

Figure 1.23: Magnetic structure for the copper atoms in a CuO_2 plane of La_2CuO_4. *(Left):* real space; *(Right):* reciprocal space. Filled and open circles denote $\uparrow$ and $\downarrow$ spins respectively[5].

However, it is crucial to differentiate between the magnetic superlattice peaks and the structural superlattice peaks resulting from staggered rotations of CuO_6 octahedra, as they can rotate slightly. Fortunately, the AF and structural peaks are observed at different positions, making them distinguishable.

The first experimental evidences for charge and stripe order were identified in two nickelate compounds $La_2NiO_{4.125}$ [27] and $La_{1.8}Sr_{0.2}NiO_4$ [17], in which stripes run diagonally, as shown in Fig.1.24*(b)*.

Successively, the neutron scattering study by Tranquada *et. al.* [24] on a single crystal of $La_{1.48}Nd_{0.4}Sr_{0.12}CuO_4$ (LNSCO, i.e. LSCO doped with Nd atoms) at doping $x = 1/8$, whose striped phase appears in Fig.1.24*(c)*, and reported in Fig.1.25, provided the first direct evidence of stripe order in cuprates. In this case the stripes are parallel to the Cu-O bonds.

Sets of four *"satellite" peaks*, appearing in presence of a modulated spin structure, are found at wave vectors $(\frac{1}{2} \pm \epsilon, \frac{1}{2} \pm \epsilon, L)$ and $(-\frac{1}{2} \pm \epsilon, \frac{1}{2} \pm \epsilon, L)$, where $\epsilon \approx x = 1/8 = 0.125$.

The period of the charge modulation is half that of the spins, which results in diffraction peaks appearing at second-harmonic positions (see Fig.1.25*(c)*), leading to a fundamental relationship between the spin and charge ordering

[17] Nickelates are materials closely related to cuprates, the main difference being the presence of NiO_2 in place of CuO_2 planes.

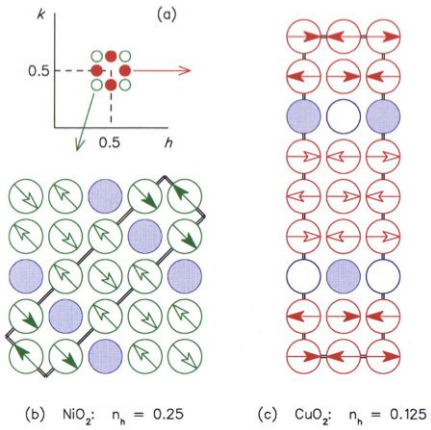

Figure 1.24: *(a)* Orientation of magnetic superlattice peaks for diagonal (open circles) and bond-parallel (filled circles) stripes. Representation of stripe order detected in $La_2NiO_{4.125}$ *(b)*, and in $La_{1.48}Nd_{0.4}Sr_{0.12}CuO_4$ *(c)*. [27] [24]. The thick lines indicate the magnetic unit cell, which is twice the size of the charge unit cell. Arrows indicate the orientation of magnetic moments on metal atoms, locally antiparallel, while oxygen atoms have been omitted. The spin direction rotates by π (relative to a simple AF structure) on crossing a domain wall. Holes are located at these boundaries, as indicated by circles without arrows; where a hole is present,centered on a metal site, the circle is filled. In *(b)* the hole density is assumed to be uniform along a domain wall, while in *(c)* it was assumed a hole-per-Cu ratio of 1/2.

incommensurability factors

$$\boxed{\delta_{\text{charge}} = 2\delta_{\text{spin}}} \tag{1.38}$$

or, in terms of the wavelengths λ of the modulations,

$$\boxed{\lambda_{\text{spin}} = 2\lambda_{\text{charge}}}. \tag{1.39}$$

Higher harmonics, in principle important to describe the spin structure, play a negligible role and thus indicate a more sinusoidal pattern of domain modulation. The charge distribution cannot be directly detected by neutrons, instead,

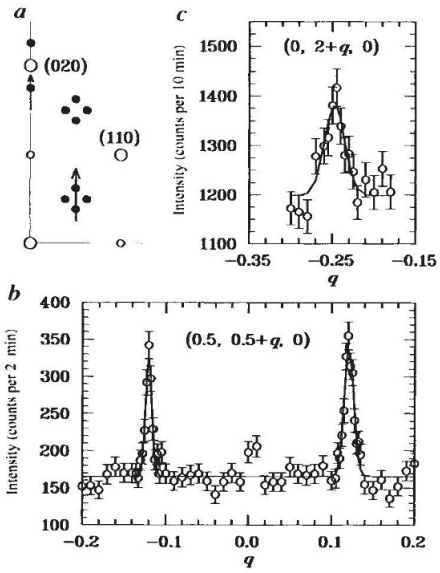

Figure 1.25: Scans of superlattice peaks of $La_{1.48}Nd_{0.4}Sr_{0.12}CuO_4$ at 11 K and doping $x = 1/8$. *(a)* $(H, K, 0)$ projection of the reciprocal space, showing the location of the measured charge and spin satellites (black circles) along the (010) and (110) directions, respectively; Bragg reflections are indicated by white circles. *(b,c)* Elastic neutron scattering measurement of the magnetic order peaks at $(0.5, 0.375, 0)$ and $(0.5, 0.625, 0)$ *(b)* and of the charge peak at $(0, 1.75, 0)$ *(c)*, with scans along the arrows indicated in *(a)*.

the modulation of atomic positions associated with the charge modulation, also known as a charge-density wave, is measured.

This study not only provided the first direct evidence of stripe order in cuprates but also, together with subsequent studies using neutron and x-ray scattering, marked the beginning of the entire experimental field of charge ordering phenomena in HTSCs.

1.5.4 The 1/8 anomaly

The previous results are not only interesting in their own right, but also because they provided the explanation for one of the long-standing mysteries associated to copper oxide superconductors: the so-called *1/8 anomaly*.

A study of the transition temperature as a function of doping in $La_{2-x}Ba_xCuO_4$ (LBCO) revealed a surprising anomaly, where T_c shows a significant dip at the unique hole-doping $x = 1/8$, in contrast to the slight kink at the same doping level for $La_{2-x}Sr_xCuO_4$ [28]. The fact that these two compounds, electronically almost identical, show a difference in T_c suggests the presence of some type of competing order. This remarkable discovery is shown in Fig.1.26.

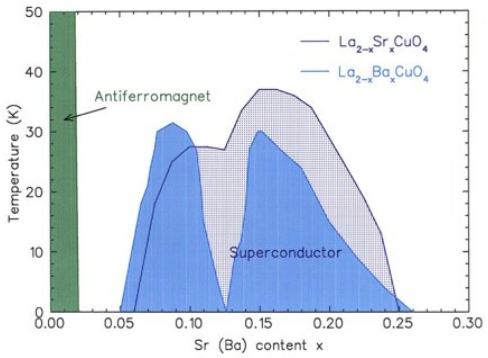

Figure 1.26: Comparison of T_c as a function of the doping x in LBCO and LSCO [28].

A subtle distinction between the two compounds comes from the fact that the CuO_6 octahedra that make up the CuO_2 planes are unstable to tilt distortion. An X-ray diffraction study by Axe *et al.* [29] revealed that, while there are no average tilts at high temperature, a second-order phase transition at low temperature brings the system to the low-temperature orthorhombic (LTO) phase. At even lower temperature, however, LBCO can undergo a second transition to the low-temperature tetragonal (LTT) phase. The LTO and LTT structures are reported in Fig.1.27. The LTO tilt pattern makes the diagonal directions of the Cu-O plaquettes inequivalent, while providing no distinction between the Cu-O

bonds along the c (i.e. perpendicular) direction. On the other hand, in the LTT phase, the orientation of the tilt axis rotates 90° when moving from one layer to the next one along the c axis, making clear that the latter phase could be more favorable for pinning a horizontal stripe phase. This anisotropy is what makes the two compounds different and is key to the pinning of the electronic order competing with the superconductivity.

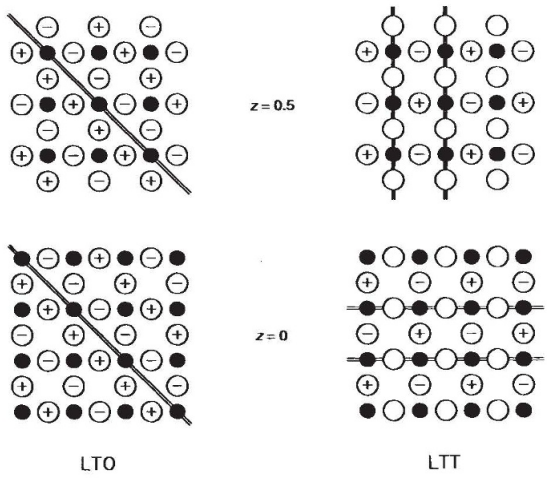

Figure 1.27: Displacement patterns within the two CuO_2 planes of a unit cell for the LTO and LTT structures. Open (solid) circles represent oxygen (copper) atoms. The oxygen atoms are displaced out of the plane (+ or −) by local rotations of square planar CuO_4 about the tilt axes represented by thick lines. In the LTT structure the tilt axes rotate by 90° when moving from $z = 0$ to $z = 0.5$, where z is the height along the c axis.

Growing LBCO crystals large enough to perform an accurate characterization by neutron scattering has been a challenge at the time of the discovery of the anomaly (1988). LNSCO, whose momentum structure was determined by the diffraction experiment reported earlier, was found to exhibit the same structural phases as LBCO and the same 1/8 anomaly. Hence, the superlattice peaks for charge and spin order in LNSCO (Fig.1.25), interpreted as evidence of horizontal stripes, address the anomalous suppression in LBCO as being caused

by the presence of stripes. Only in 2004, when LBCO crystals at $x = 1/8$ were eventually grown, stripe order was confirmed there as well [30].

1.5.5 Coexistence of the two phenomena

The relation between stripes and the mechanism of high-temperature superconductivity is still an issue, but there is strong empirical evidence for an intimate relation between the two phenomena:

- Strongly condensed stripe order can suppress superconductivity
- Sometimes a weak stripe ordering can appear at the superconducting transition temperature T_c
- In several materials a simple linear relation between the inverse stripe spacing and T_c is found [31]
- By "overdoping" the parent compound, stripe structure and other features of the doped insulator, together with high-temperature superconductivity, disappear

Additionally, it has been shown that the best conditions for high-temperature superconductivity involve stripe correlations that are not too static or strongly condensed, but also not too unstable or highly fluctuating.

Chapter 2

Experimental Tools

[1]The most direct evidence for stripe phases in doped antiferromagnets has come from neutron scattering and X-ray scattering studies.

When long-period spin and charge density modulations extend over a few unit cells, the diffraction of a neutron beam yields extra Bragg peaks. The position of such *superstructure peaks* allows one to measure the spatial period and orientation of the corresponding density modulation; its intensity provides a measure of the modulation amplitude. Being neutrons chargeless particles, they cannot directly scatter from the modulated electron density. Instead, they are scattered by the ionic displacements caused by the charge modulation.

X-ray scattering methods (and Resonant X-Ray Scattering (RXS) experiments in particular) are, on the other hand, a great tool for studying the ordering of charge, spin, orbital, and lattice degrees of freedom, often providing a distinctive viewpoint on their interaction and interplay.

Results from inelastic neutron scattering on superconducting $La_{2-x}Sr_xCuO_4$ [32] and on the related nickelate analog [33], have been the first indication of long-period spin-density modulations. Electron diffraction allowed to prove the existence of such ordering in the latter system [34] and, after that, the proper connection between the magnetic and charge-order peaks was determined in a

[1]A more complete discussion can be found in [5]

neutron diffraction study of $La_2 Ni O_{4.125}$ [27].

A significant observation is that the charge ordering is always observed at a higher temperature than the magnetic ordering, which is characteristic [35] of a transition driven by the charge. The period of the charge order has been shown to be generally temperature dependent, which means that the hole concentration along each stripe also varies with temperature; this feature is typical of structures that arise from competing interactions [36]: the clustering tendency of holes and the repulsive long-range Coulomb interaction.

Moreover, stripes are easier to detect when they are static, but a perfect staticness has been shown to be incompatible with the metallic behaviour of the cuprates [37].

2.1 Neutron Scattering

Neutron scattering is an effective method for investigating strongly correlated systems. It is capable of detecting common phenomena like magnetic order and can be used to measure the interaction between magnetic moments by examining spin-wave dispersions. When magnetic order is absent, it can still detect diffuse scattering and dynamic correlations. Neutrons are also effective in determining the atomic arrangement within solids (crystal structure) and lattice dynamics (phonons).

The neutrons typically involved in experiments related to the present work are called "thermal" neutrons, quite useful to the study of Bragg diffraction in crystal structures; in fact, they are characterized by a typical energy of 30meV (very moderate) and wavelength of order 1.65Å, which is well matched to common interatomic spacing.

The scattering of neutrons from atomic nuclei is mediated by the strong force. Contrary to its name, the nucleus, being small in comparison to the electron cloud of an atom, results in a relatively low scattering cross section.

The nuclear scattering cross section changes from element to element (and

even from one isotope to another, as one can see in Fig.2.1[2]), due to the very complicated interaction between neutrons and atoms, determined by the exact structure of the nucleus; however, the typical magnitude of the cross section is roughly independent of atomic number: this is particularly important when measuring the structure of compounds such as cuprates, where the constituent elements have very different atomic numbers (as an example, in La_2CuO_4, $Z(O) = 16$, $Z(La) = 57$, where Z indicates the atomic number).

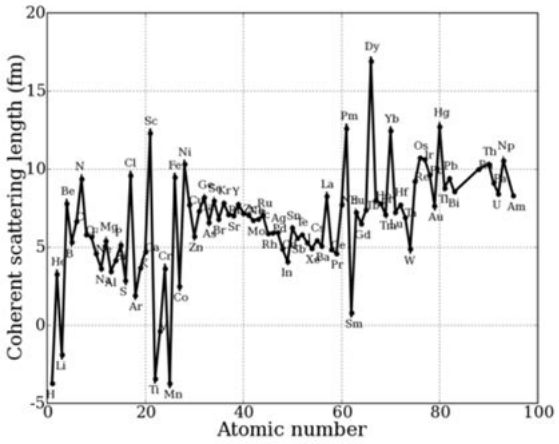

Figure 2.1: Coherent scattering length as a function of the atomic number. Notice the difference between those of hydrogen (H, negative value) and its isotope deuterium (H_2, positive value), despite having the same number of electrons.

As a comparison, x-rays are instead scattered by the electronic charge density of atoms and the weight per atom in diffraction pattern has a Z^2 dependence, thus providing a 13 times smaller sensitivity to O compared to La. Neutrons, on the other hand, have roughly uniform sensitivity to all these elements. This provides a different degree of chemical sensitivity between the two probes, as clearly visible from Fig.2.1 and Fig.2.2.

[2]A positive scattering length of a nucleus means that the neutron is subject to a repulsive potential as it approaches the nucleus, whereas a negative scattering length involves an attractive potential.

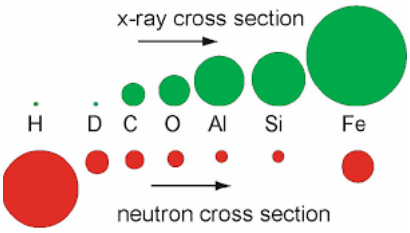

Figure 2.2: Pictorial representation of the cross-section of different atoms using neutron scattering and x-ray diffraction. The x-ray interaction simply depends on the number of electrons, meaning that adjacent nuclei in the periodic table have very similar x-ray scattering factors *(green circles)*. On the other hand, as pointed out in Fig.2.1, neutron scattering allows to distinguish isotopes such as H from H_2 *(red circles)*.

Neutrons are also spinful particles, which means that they are affected by dipole-dipole interaction, allowing them to scatter from atomic magnetic moments. Magnetic diffraction and nuclear diffraction can be of the same strength in presence of large ordered magnetic moments. This is not the case in X-ray diffraction, where the magnetic cross section is reduced relative to charge scattering by a factor α^2, where $\alpha = \frac{1}{137}$ is the fine structure constant.

Creating neutron beams is harder than finding x-ray sources, as will be mentioned in Sec.2.1.2. The number of neutrons produced by these sources is in any case modest, hence their "brightness" is lower than in x-ray sources.

One of the challenges of neutron scattering is its weak scattering cross section and limited source strength, which necessitate the use of large sample sizes. Despite this, the insights gained from neutron scattering make it worthwhile to grow large samples. To supplement the information obtained from neutron scattering, techniques such as muon Spin Rotation (μSR) spectroscopy and Nuclear Magnetic Resonance (NMR) can be utilized, although they may provide less information, as they offer greater precision. Although there have been advancements in Resonant X-Ray Scattering (RXS), neutron scattering remains a crucial tool for investigating strongly correlated systems.

2.1.1 Theory of Scattering of Neutrons by a Crystal

[3] The general diagram of a neutron scattering experiment is illustrated in Fig.2.3. Here, the incident neutron has average momentum $\hbar\mathbf{k}_i$ and magnitude of the wave vector $k = |\mathbf{k}_i| = 2\pi/\lambda$. where λ is the neutron wave length. Its energy is given by

$$E^{neutr} = \frac{\hbar^2 k^2}{2M_n},$$

where M_n is the mass of the neutron. Neutrons used in scattering experiments are non-relativistic. The quantity detected after the scattering event is the new wave vector $\mathbf{k}_f$ of the neutron.

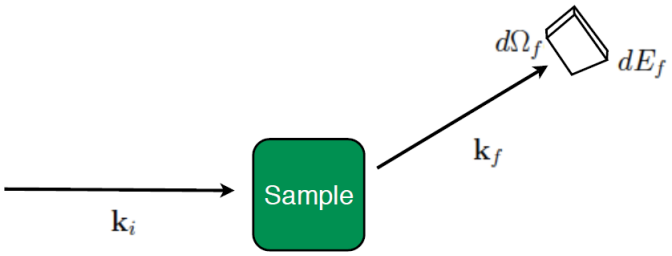

Figure 2.3: Diagram of scattering process. [5]

A few assumptions can be made:

- The only degrees of freedom of the crystal are those associated with ionic motion
- Before the scattering event, the ions are in an eigenstate of the crystal Hamiltonian with energy E_i
- After the scattering event, the ions are in a different eigenstate of the crystal Hamiltonian with energy E_f

The initial and final states, and their associated energies, of the neutron-ion system can be described as follows:

[3]Main reference:Ashcroft, Mermin: Solid State Physics [38]

Before scattering:

$$|\Psi_i\rangle = \psi_{\mathbf{k}_i}\Phi_i \qquad\qquad \epsilon_i = E_i + \frac{\hbar^2 {\mathbf{k}_i}^2}{2M_n} \tag{2.1}$$

After scattering:

$$|\Psi_f\rangle = \psi_{\mathbf{k}_f}\Phi_f \qquad\qquad \epsilon_f = E_f + \frac{\hbar^2 {\mathbf{k}_f}^2}{2M_n} \tag{2.2}$$

where $\psi_{\mathbf{k}} = e^{i\mathbf{k}\cdot\mathbf{r}}/\sqrt{V}$ and V is volume over which the wavefunction is normalized.

It is convenient to define the neutron momentum transfer

$$\hbar\mathbf{Q} = \mathbf{p}_f - \mathbf{p}_i = \hbar\mathbf{k}_f - \hbar\mathbf{k}_i,$$

illustrated in Fig.2.4, where the angle $2\Theta_s$ is called *scattering angle* and a useful formula is:

$$|\mathbf{Q}| = k_i^2 + k_f^2 - 2k_i k_f \cos 2\Theta_s.$$

The energy transferred to the sample is given by

$$\hbar\omega = E_i^{neutr} - E_f^{neutr} = \frac{\hbar^2}{2M_n}(k_i^2 - k_f^2).$$

The neutron-ion interaction can be written as:

$$V(\mathbf{r}) = \sum_{\mathbf{R}} v(\mathbf{r} - \mathbf{r}(\mathbf{R})) = \frac{1}{V}\sum_{\mathbf{k},\mathbf{R}} v_{\mathbf{k}} e^{i\mathbf{k}\cdot[\mathbf{r}-\mathbf{r}(\mathbf{R})]}. \tag{2.3}$$

Being the range of v of the order of the typical nuclear dimension ($\approx 10^{-13}$cm), its Fourier components will vary on the scale of $k \approx 10^{13}\text{cm}^{-1}$, and therefore be essentially independent of k in the relevant range for experiments that measure phonon spectra, in which $k \sim 10^{8}\text{cm}^{-1}$.

The scattering cross-section σ is a measure of the rate of interaction between radiation and a target, calculated by considering the incoming radiation as a series of particles, such as photons or neutrons.

The cross-section represents the number of scattering events per unit time per unit area of the target, per unit incident radiation flux. This measurement is expressed in terms of an effective area, in units of *barn* (10^{-28}m^2). The quantity

σ should not be considered as a true geometric cross-section, but rather as an area proportional to the interaction probability.

In the laboratory, differential scattering cross-sections are measured. The double-differential cross section $\frac{d^2\sigma}{d\Omega_f dE_f}$ measures the probability of scattering into a differential solid angle $d\Omega_f$ and energy dE_f. The latter is then used to calculate $\frac{d\sigma}{d\Omega}$ and σ by integrating over the energy of the scattered radiation and solid angle.

The constant quantity $v_0 \approx v_{\mathbf{k}}$ is conventionally written in terms of the *scattering length* a, defined so that the total cross section scattering of a neutron by a single isolated ion is given in Born approximation[4], in which nuclei are assumed to have zero spin and be made of a single isotope, by $4\pi a^2$.

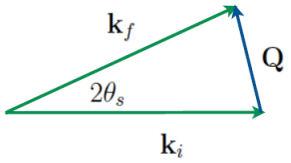

Figure 2.4: Scattering triangle

Eq.2.3 is thus written as:

$$V(\mathbf{r}) = \frac{2\pi\hbar^2 a}{M_n V} \sum_{\mathbf{k},\mathbf{R}} e^{i\mathbf{k}\cdot[\mathbf{r}-\mathbf{r}(\mathbf{R})]} \tag{2.4}$$

The *transition rate* P (i.e. probability per unit time) for a neutron to scatter from $\mathbf{p}_i$ to $\mathbf{p}_f$ as a result of its interaction with the ions can be calculated with

[4]In the most general case this approximation is not valid, implying a dependence of a on the nuclear state. Besides the *coherent* term, derived in the present discussion, the cross section acquires a new *incoherent* term, which has no distinct energy dependence and contributes, along with the multiphonon processes, to the diffuse background

the "golden rule" [39] of lowest-order time-dependent perturbation theory:

$$P = \sum_f \frac{2\pi}{\hbar}\delta(\epsilon_i - \epsilon_f)|\left\langle \Psi_i \,|\, V \,|\, \Psi_f \right\rangle|^2 \tag{2.5}$$

$$= \sum_f \frac{2\pi}{\hbar}\delta(E_f - E_i + \hbar\omega)\left|\frac{1}{V}\int d\mathbf{r} e^{i\mathbf{Q}\cdot\mathbf{r}}\left\langle \Phi_i \,|\, V(\mathbf{r}) \,|\, \Phi_f \right\rangle\right|^2 \tag{2.6}$$

$$= \frac{(2\pi\hbar)^3}{(M_n V)^2} a^2 \sum_f \delta(E_f - E_i + \hbar\omega)\left|\sum_{\mathbf{R}}\left\langle \Phi_i \,\middle|\, e^{i\mathbf{Q}\cdot\mathbf{r}(\mathbf{R})} \,\middle|\, \Phi_f \right\rangle\right|^2, \tag{2.7}$$

P is related to the measured cross section $\frac{d^2\sigma}{d\Omega dE}$ by connecting it to the *incident neutron flux*

$$j = \frac{k}{M_n}|\psi_{\mathbf{k}}|^2 = \frac{k}{M_n V},$$

so that [5]

$$j\frac{d^2\sigma}{d\Omega dE}d\Omega dE = \frac{k_i}{M_n V}\frac{d^2\sigma}{d\Omega dE}d\Omega dE = \frac{PV d\mathbf{k}_f}{(2\pi\hbar)^3} \tag{2.8}$$

$$= \frac{PV k_f^2 dk_f d\Omega}{(2\pi\hbar)^3} = \frac{PV M_n k_f dE d\Omega}{(2\pi\hbar)^3}. \tag{2.9}$$

Finally, Eq.2.5 and Eq.2.8 can be put together, under the condition for all the final states f to be compatible with a given initial state i through the energy-conserving constraint given by the δ-function, to obtain:

$$\frac{d^2\sigma}{d\Omega dE}d\Omega dE = \frac{k_f}{k_i}\frac{Na^2}{\hbar}\mathcal{S}_i(\mathbf{Q},\omega), \tag{2.10}$$

where

$$\mathcal{S}_i(\mathbf{Q},\omega) = \frac{1}{N}\sum_f \delta\left(\frac{E_f - E_i}{\hbar} + \omega\right)\left|\sum_{\mathbf{R}}\left\langle \Phi_i \,\middle|\, e^{i\mathbf{Q}\cdot\mathbf{r}(\mathbf{R})} \,\middle|\, \Phi_f \right\rangle\right|^2 \tag{2.11}$$

and N is the number of atoms per unit volume in the sample.

The quantity $\mathcal{S}_i(\mathbf{Q},\omega)$ can be evaluated using the representation

$$\delta(\omega) = \int_{-\infty}^{+\infty}\frac{dt}{2\pi}e^{i\omega t}$$

[5] Using the fact that a volume element $d\mathbf{k}_f$ contains $V d\mathbf{k}_f/(2\pi\hbar)^3$ neutron states of a given spin.

and by noting that any operator $\hat{A}$ obeys the relation:

$$e^{i(E_f-E_i)t/\hbar}\left\langle \Phi_f \left| \hat{A} \right| \Phi_i \right\rangle = \langle \Phi_f \,|\, A(t) \,|\, \Phi_i \rangle$$

and, furthermore, for any pair of operators $\hat{A}$ and $\hat{B}$,

$$\sum_f \left\langle \Phi_i \left| \hat{A} \right| \Phi_f \right\rangle \left\langle \Phi_f \left| \hat{B} \right| \Phi_i \right\rangle = \left\langle \Phi_i \left| \hat{A}\hat{B} \right| \Phi_i \right\rangle$$

.

In doing so, defining $\mathbf{u}$ the vector indicating the (small) displacement of the ion with respect to its equilibrium position,

$$\mathcal{S}_i(\mathbf{Q},\omega) = \frac{1}{N}\int \frac{dt}{2\pi} e^{i\omega t} \sum_{\mathbf{R},\mathbf{R'}} e^{-i\mathbf{Q}\cdot(\mathbf{R}-\mathbf{R'})} \left\langle \Phi_i \left| e^{i\mathbf{Q}\cdot\mathbf{u}(\mathbf{R'})} e^{-i\mathbf{Q}\cdot\mathbf{u}(\mathbf{R},t)} \right| \Phi_i \right\rangle . \tag{2.12}$$

Since the crystal is in general in thermal equilibrium, the cross section has to be averaged for the given initial state i over a Maxwell-Boltzmann distribution of equilibrium states. This is done by replacing $\mathcal{S}_i$ by its thermal average:

$$\mathcal{S}(\mathbf{Q},\omega) = \frac{1}{N}\sum_{\mathbf{R},\mathbf{R'}} e^{-i\mathbf{Q}\cdot(\mathbf{R}-\mathbf{R'})} \int \frac{dt}{2\pi} e^{i\omega t} \langle e^{i\mathbf{Q}\cdot\mathbf{u}(\mathbf{R'})} e^{-i\mathbf{Q}\cdot\mathbf{u}(\mathbf{R},t)} \rangle, \tag{2.13}$$

where

$$\langle \hat{A} \rangle = \frac{\sum e^{-\beta E_i} \left\langle \Phi_i \left| \hat{A} \right| \Phi_i \right\rangle}{\sum e^{-\beta E_i}},$$

and $\beta = 1/k_B T$ is the inverse temperature. The quantity $\mathcal{S}(\mathbf{Q},\omega)$ is the *dynamical structure factor* of the crystal, and does not depend on any properties of the neutrons.

All in all, what we get is the concise and elegant result:

$$\frac{d^2\sigma}{d\Omega dE} d\Omega dE = \frac{p_f}{p_i}\frac{Na^2}{\hbar}\mathcal{S}(\mathbf{Q},\omega). \tag{2.14}$$

2.1.2 Neutron scattering in practice

In this section some basic properties of neutron scattering experiments are discussed[6]. The neutron is an elementary particle with a spin 1/2 and is a building block of the atomic nucleus, together with the proton. According to the

[6]For a more exhaustive discussion, see Zaliznyak and Tranquada [25]

standard model of elementary particles, the neutron and proton are fermionic hadrons, also known as baryons, made up of different combinations of quarks. The neutron consists of one "up" quark and two "down" quarks, while the proton consists of two "up" quarks and one "down" quark. The free neutron, unstable when outside of the nucleus, undergoes β-decay into a proton, an electron, and an antineutrino. Despite its relatively short lifespan of 15 minutes, it is still sufficient for the purposes of neutron-scattering experiments.

In order to generate neutron beams, it is necessary to extract neutrons from atomic nuclei. There are two methods to accomplish this. The first is through the fission process in a nuclear reactor, where each uranium ^{235}U fission produces a couple of neutrons, leading to a self-sustaining chain reaction. The second method involves knocking neutrons out of heavy-metal nuclei (*spallation*), such as tungsten or mercury, using a high-energy proton beam.

Experimental measurement of the cross-section

The result of Eq.2.14 does not provide a straightforward way to measure the cross-section in practice. In a scattering experiment, the sample is placed in the neutron beam having a well-defined wave vector $\mathbf{k}_i$ and known incident flux density $\varphi_i(\mathbf{k}_i)$. The detector measures the partial current $\delta J_f(\mathbf{k}_f)$ scattered into a small (infinitesimal, ideally) volume of phase space

$$d^3\mathbf{k}_f = k_f^2 dk_f d\Omega_f = (M_n k_f/\hbar^2) dE_f d\Omega_f,$$

near the wavevector $\mathbf{k}_f$, as shown in Fig.2.5.

This measured partial current, appropriately normalized by the phase space element covered by the detector, yields the scattered current density. At this point the double differential scattering cross-section can be computed:

$$\frac{d^2\sigma(\mathbf{Q},E)}{d\Omega dE} = \frac{1}{\varphi_i(\mathbf{k}_i)} \frac{\delta J_f(\mathbf{k}_f)}{d\Omega dE}. \tag{2.15}$$

For each incident neutron in the plane wave state $e^{i\mathbf{k}_i\cdot\mathbf{r}_n}$, the incident flux density is $\varphi_i(\mathbf{k}_i) = \hbar k_i/M_n$. The scattered current density is instead related to the transition rate $\Gamma_{i\to f}$ from the initial state $\left|\mathbf{k}_i, S^z_{n,i}, \eta_i\right\rangle$, with the neutron in

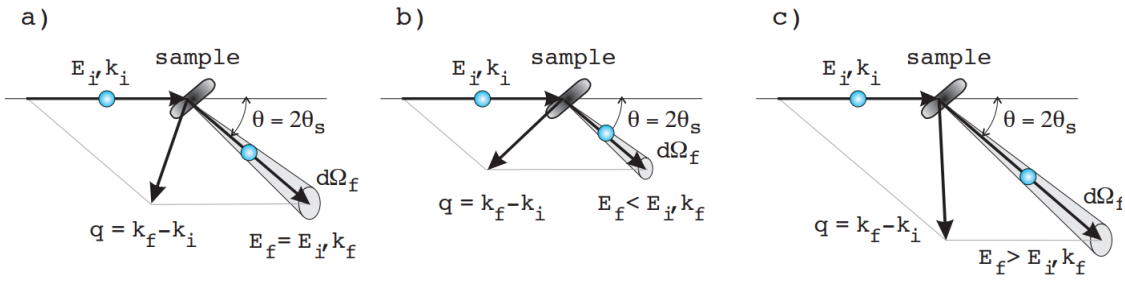

Figure 2.5: [25] Schematic representation of the scattering process in a neutron scattering experiment. *(a)* elastic, *(b)* inelastic with neutron energy loss, *(a)* with neutron energy gain

the plane wave state $e^{i\mathbf{k}_i \cdot \mathbf{r}_n}$ with spin $S^z_{n,i}$ and scattering system described by the set of variables η_i, to the final one $\left|\mathbf{k}_f, S^z_{n,f}, \eta_f\right\rangle$.

Typical experimental setup

The setup for a neutron scattering experiment will vary depending on the specifics of the experiment. However, the key components and principles remain the same and typically involve the following:

- *Neutron source*, among those described in the current chapter. The choice of neutron source depends on the energy range and brightness of the neutrons required for the experiment.
- *Sample*: The sample being studied is typically a single crystal or powder of the material. In the case of stripe order in cuprate superconductors, the sample is prepared and aligned in a specific way to allow the neutron scattering experiment to probe the desired ordered state. This may involve cooling the sample to low temperatures, applying magnetic fields, or orienting the sample in a specific way.
- *Neutron guide and monochromator*: The neutron guide is used to transport the neutrons from the source to the sample, while the monochromator is used to select a specific energy range of neutrons for the experiment.

- *Sample environment*: The sample environment is critical for controlling the temperature, pressure, and magnetic field conditions under which the sample is studied. This may involve a cryostat for cooling the sample, a pressure cell for controlling the pressure, or a magnet for applying magnetic fields.

- *Neutron detectors*: The scattered neutrons are measured by neutron detectors, which can be positioned around the sample to collect data from different scattering angles. The choice of neutron detectors depends on the type of data being collected and the energy range of the scattered neutrons. The precise setup and conditions are chosen to maximize the sensitivity to the desired properties and minimize the contribution from other types of scattering.

- *Data analysis*: The data collected by the neutron detectors is analyzed to extract information about the magnetic and atomic structures of the sample. This may involve Fourier transforming the data to obtain the reciprocal space representation of the structure, or fitting the data to a theoretical model to extract the physical parameters of interest.

2.2 Resonant X-ray methods

[7]X-rays have been widely used to investigate the internal structure of matter, as they interact with the electronic clouds surrounding atomic nuclei [41]. Early signs of resonant x-ray effects were discovered in the 1970s when de Bergevin and Brunel [42] found that x-rays can also detect electronic spin distribution in magnetic materials by identifying antiferromagnetic Bragg reflections in NiO.

Subsequently, synchrotron-based x-ray magnetic scattering has been used as an effective alternative to neutron scattering on several magnetically-ordered systems. Since its introduction in the 1980s, Resonant X-Ray Scattering (RXS) has grown into a highly flexible tool for examining ordering phenomena involving

[7]Main reference: Comin and Damascelli [40]

charge, spin, orbital, and lattice degrees of freedom, often providing a unique viewpoint on their interplay.

2.2.1 X-Ray scattering in theory

RXS is a technique where photons are scattered from a material due to their interaction with the electronic cloud. To have radiation-matter scattering, the interaction Hamiltonian must contain combinations of operators in the form $a_\nu(\mathbf{q})a^\dagger_\nu(\mathbf{q}-\mathbf{Q})$, where $a^\dagger_\nu(\mathbf{q})$ and $a_\nu(\mathbf{q})$ are operators that create and annihilate photons with wave vector $\mathbf{q}$, polarization state ν and frequency $\omega = c|\mathbf{q}|$. The effective non-relativistic interaction Hamiltonian can be derived from the full electron-matter minimal coupling Hamiltonian, and reads:

$$H_{tot} = \sum_j \left\{ \frac{1}{2m_e}[\mathbf{p}_j - \frac{e}{c}\mathbf{A}(\mathbf{r}_j,t)]^2 + V(\mathbf{r}_j,t) \right\} + \sum_{j\neq k} \frac{e^2}{|\mathbf{r}_j - \mathbf{r}_k|^2} + H_{EM} \quad (2.16)$$

$$= \underbrace{H_{el} + H_{EM}}_{H_0} + \underbrace{\frac{e}{m_e c}\sum_j \mathbf{A}(\mathbf{r}_j,t)\cdot\mathbf{p}_j}_{H^{lin}_{int}} + \underbrace{\frac{e^2}{2m_e c^2}\sum_j \mathbf{A}^2(\mathbf{r}_j,t)}_{H^{quad}_{int}} \quad (2.17)$$

where the total Hamiltonian is the sum of the Hamiltonian of the electronic system alone,

$$H_{el} = \sum_j \left\{ \frac{1}{2m_e}\mathbf{p}_j^2 + V(\mathbf{r}_j,t) \right\} + \sum_{j\neq k} \frac{e^2}{|\mathbf{r}_j - \mathbf{r}_k|^2},$$

taking into account the lattice potential $V(\mathbf{r}_j,t)$ and the Coulomb interaction term $\frac{e^2}{|\mathbf{r}-\mathbf{r}'|^2}$, the interaction with the vector potential $\mathbf{A}(\mathbf{r}_j,t)$, and the Hamiltonian of the electromagnetic (EM) field alone,

$$H_{EM} = \sum_{\mathbf{q},\nu} \hbar\omega[a^\dagger_\nu(\mathbf{q})a_\nu(\mathbf{q}) + 1/2];$$

e and m_e represent the electronic charge and mass, $\mathbf{p}_j$ and $\mathbf{r}_j$ are the momentum and position coordinates of the j-th electron.

H^{lin}_{int} and H^{quad}_{int}, linear and quadratic in $\mathbf{A}$ respectively, couple the electronic degrees of freedom and the EM field.

As a basis for the light-matter quantum system, we can use the states

$$|\Psi_M\rangle = |\psi_m\rangle_{el} \times \left|\phi_{n_{\bar{\mathbf{q}},\nu}}\right\rangle_{EM}$$

where $|\psi_m\rangle_{el}$ represents the electronic part of the wavefunction (with eigenvalues ϵ_m and m being the quantum number labeling them), and $\left|\phi_{n_{\bar{\mathbf{q}},\nu}}\right\rangle_{EM}$ indicates a photon state with photon occupation $\bar{n}_{\mathbf{q},\nu} = \{n_{\mathbf{q}_1,\nu_1}, n_{\mathbf{q}_2,\nu_2}, \dots\}$ corresponding to having $n_{\mathbf{q}_1,\nu_1}$ photons with wave vector $\mathbf{q}_1$ and polarization ν_1, $n_{\mathbf{q}_2,\nu_2}$ photons with wave vector $\mathbf{q}_2$ and polarization ν_2, and so on.

Here, $M = \{m, \mathbf{q}, \nu\}$ is the label for the global set of quantum numbers. The interaction between radiation and matter causes the states of the system $\{|\Psi_M\rangle\}$ to not be eigenstates. However, they can still be used as a basis set in a perturbative approach (i.e. by discarding the interaction terms in the first place).

In this approach, the unperturbed energy spectrum is defined as

$$E_M = \epsilon_m + \sum_{\mathbf{q},\nu} (n_{\mathbf{q},\nu}\hbar\omega_{\mathbf{q}} + 1/2).$$

A scattering process is defined as a transition from an initial state

$$|\phi_i\rangle_{EM} = |\dots\rangle \left|n_{\mathbf{q}_{in},\nu_{in}}\right\rangle \left|n_{\mathbf{q}_{out},\nu_{out}}\right\rangle |\dots\rangle$$

of a photon with a certain wavevector and polarization $(\mathbf{q}_{in}, \nu_{in})$ being annihilated, and an outgoing photon with different wavevector and polarization $(\mathbf{q}_{out}, \nu_{out})$ being created in a final photon state

$$|\phi_f\rangle_{EM} = |\dots\rangle \left|n_{\mathbf{q}_{in},\nu_{in}} - 1\right\rangle \left|n_{\mathbf{q}_{out},\nu_{out}} + 1\right\rangle |\dots\rangle .$$

Key quantities in this discussion are the probabilities of transition from a state $|\Psi_i\rangle = |\psi_{GS}\rangle_{el} \times |\phi_i\rangle_{EM}$ to a final one $|\Psi_f\rangle = |\psi_{GS}\rangle_{el} \times |\phi_f\rangle_{EM}$, under the additional hypothesis of having $|\psi_m\rangle_{el} \equiv |\psi_{GS}\rangle_{el}$ (i.e. the electronic part of the initial and final state is in its ground state). By using the generalized Fermi's golden rule [39], the transition probability $w_{i\to f}$ between the two quantum states can be calculated:

$$w_{i\to f} = 2\pi |\langle \Psi_i | T | \Psi_f \rangle|^2 \delta(E_f - E_i) \tag{2.18}$$

where the T-matrix is defined as:

$$T = H_{int} + H_{int}\frac{1}{E_i - H_0 + i\eta}H_{int} + H_{int}\frac{1}{E_i - H_0 + i\eta}H_{int}\frac{1}{E_i - H_0 + i\eta}H_{int} + \dots \tag{2.19}$$

recalling that $H_0 = H_{el} + H_{EM}$ is the unperturbed Hamiltonian and $H_{int} = H_{int}^{lin} + H_{int}^{quad}$ the interaction operator.

The n-th operator on the right-hand side represents the n-th order perturbation term. By looking at the second-quantized form of $\mathbf{A}(\mathbf{r}, t) \propto \sum_{\mathbf{q},\nu} \mathbf{e}_\nu \cdot [e^{i\mathbf{q}\cdot\mathbf{r} - i\omega t} a_\nu^\dagger \mathbf{q} + h.c.]$, we see that the combinations of operators of the kind $a^\dagger a$ required to describe scattering events, is generated in Eq.(2.19) by the quadratic interaction operator H_{int}^{quad} in the first-order term, and by the linear one H_{int}^{lin} in the second-order term. From this, the perturbative transition probabilities $w_{i\to f}^{(1)}$ and $w_{i\to f}^{(2)}$, corresponding to the first and second order respectively, can be computed.

In the x-ray regime, the term $w_{i\to f}^{(2)}$ involves the excitation of a core hole into an intermediate state through the absorption of a photon, followed by the re-emission of a scattered photon once the core hole is filled back. This second-order process is resonant and is associated with RXS. On the other hand, the first-order term $w_{i\to f}^{(1)}$ in the scattering process (known as Thomson scattering) is instantaneous and does not involve the excitation of an intermediate state. The latter is non-resonant and controls the signal in conventional X-Ray Diffraction (XRD).

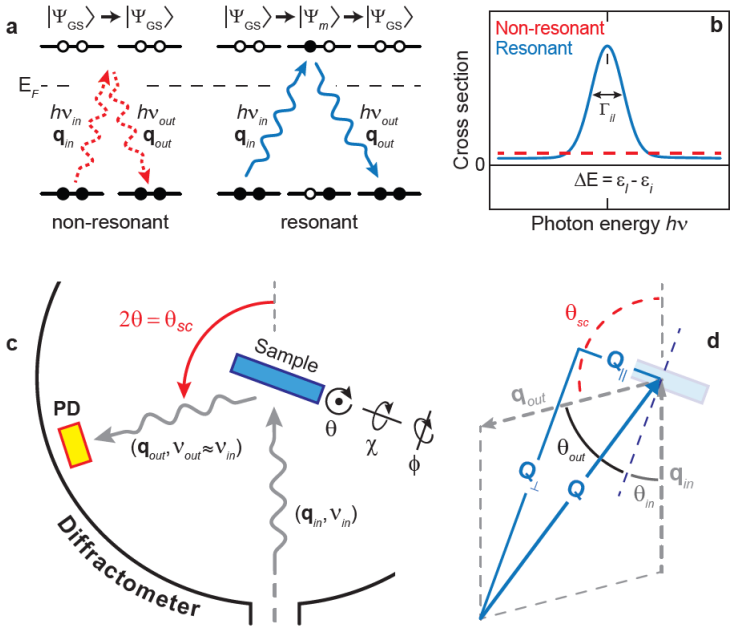

Figure 2.6: Resonant processes and scattering geometry in RXS, from [40]. *(a)* In non-resonant scattering, the excitation process does not involve intermediate energy states, while in resonant scattering, the energy of the incident photon is tuned to promote an electronic transition from the ground state $|\Psi_{GS}\rangle$ to an intermediate state $|\Psi_m\rangle$. This results in the creation of an outgoing scattered photon through the recombination of the excited electron with a core hole. *(b)* Different energy dependence of resonant and non-resonant processes. An enhancement of the resonant channel near an electronic transition with energy ΔE distinguishes the two. *(c)* A schematic of a conventional diffractometer, illustrating the kinematics of the scattering/diffraction process, as outlined in *(d)*.

The two processes are schematically depicted in Fig.2.6(a). XRD is a one-step process due to its first-order nature, while RXS is a two-stage process involving an intermediate state. This is reflected in the different photon energy ($h\nu$) dependencies of the two channels, as shown in Fig.2.6(b). XRD is almost energy-independent (red dashed curve), while the cross-section for RXS

is strongly peaked around the energy of the electronic transition (blue curve), where the experimental signal is greatly enhanced and decays to zero away from the resonance. This typically occurs at an absorption edge, when electronic transitions from deeply bound core states to the valence band (and beyond into the continuum) take place. As a result, RXS is highly sensitive to partial modulations of the charge density involving a single electronic band, while the XRD signal reflects the total electronic density and is therefore less sensitive to spatial variations of the density, unless they are accompanied by a distortion of the lattice, which would involve all the electrons (core and valence).

In order to get closer to computing some observable quantities, the photon-energy/site-dependent complex tensor called *form factor* f_{pq} is defined as follows:

$$f^n_{pq}(\hbar\omega) = \frac{e^2}{m^2c^2}\sum_{i,l}\frac{\left\langle \chi^{(n)}_i \middle| p_q \middle| \chi^{(n)}_l \right\rangle \cdot \left\langle \chi^{(n)}_l \middle| p_p \middle| \chi^{(n)}_i \right\rangle}{\hbar\omega - (\epsilon^{(n)}_l - \epsilon^{(n)}_i) + i\Gamma_{il}}. \tag{2.20}$$

Here, $\chi^{(n)}_i$ and $\chi^{(n)}_l$ represent the initial and intermediate single-particle electronic states at site $\mathbf{R}_n$ and energies $\epsilon^{(n)}_i$ and $\epsilon^{(n)}_l$, respectively, involved in the light-induced transition $i \to l$. $\Gamma_{il} := \hbar/\tau_{il}$ is the inverse lifetime of the intermediate state with an electron in $\chi^{(n)}_l$ and a hole in $\chi^{(n)}_i$. The form factor f^n_{pq} is closely related to the X-Ray Absorption (XAS), a first-order process in the radiation-matter interaction Hamiltonian, which in turn bears a connection to the resonant scattering cross-section:

$$I^{XAS}(\hbar\omega) \propto -\frac{1}{\omega^2} \times Im\left[\sum_n \sum_p (\mathbf{e}_{\nu_{in}})_p \cdot f^{(n)}_{pp}(\hbar\omega)\right] \tag{2.21}$$

$$I^{RXS}(\mathbf{Q},\hbar\omega) \propto \left|\sum_{pq}(\mathbf{e}_{\nu_{in}})_p \cdot \left[\sum_n f^{(n)}_{pq}(\hbar\omega)e^{i\mathbf{Q}\cdot\mathbf{R}_n}\right] \cdot (\mathbf{e}_{\nu_{out}})_q\right|^2 \tag{2.22}$$

$$= \left|\sum_{pq}(\mathbf{e}_{\nu_{in}})_p \cdot F_{pq}(\hbar\omega) \cdot (\mathbf{e}_{\nu_{out}})_q\right|^2. \tag{2.23}$$

From Eq.2.21 it follows that XAS only depends on the polarization of the incoming light $\mathbf{e}_{\nu_{in}}$.

On the other hand, in Eq.2.23, the *scattering tensor* F_{pq} is a nonlocal quantity (i.e. has no dependence of the lattice position $\mathbf{R}_n$) directly related to the physical observable in RXS experiments (I^{RXS}). Moreover, the RXS signal depends on the outgoing polarization $\mathbf{e}_{\nu_{out}}$ as well.

2.2.2 ...and in practice

In a scattering or diffraction experiment, a monochromatic x-ray beam with wavevector $\mathbf{q}_{in}$, photon energy $\hbar\omega_{in} = c \times q_{in}$, and polarization $\mathbf{e}_{\nu_{in}}$, strikes a sample and a scattered photon is detected along the direction of the wavevector $\mathbf{q}_{out}$ by an energy-integrating Photon Detector (PD) or an energy-resolving spectrometer (see Fig.2.6(c)).

At the end of the process, momentum and energy are transferred to the sample and can be determined from the conservation laws:

$$h\nu_{in} = h\nu_{out} + \Delta E \tag{2.24}$$

$$\mathbf{q}_{in} = \mathbf{q}_{out} + \mathbf{Q} \tag{2.25}$$

In the case of elastic scattering $h\nu_{in} = h\nu_{out}$ and there is no energy transfer with the sample ($\Delta E = 0$), while inelastic scattering events have $\Delta E \neq 0$. Elastic scattering probes the static component of the charge and magnetization density in the system under inspection, while inelastic scattering is sensitive to dynamic processes and low-energy excitations.

However, due to the finite energy resolution of the spectrometer δE, purely elastic scattering cannot be accessed experimentally, and it is more appropriate to use the term quasi-elastic scattering, which probes a regime that is static up to a timescale $\tau \sim \hbar/\delta E$.

In most cases, the energy-integrated measurement provides a reliable representation of the momentum structure of the ordered state, due to the fact that the inelastic part of the spectra usually evolves smoothly and can be discarded as background in RXS, especially if it has a different temperature dependence with respect to the zero energy loss feature.

Usually, RXS experiments investigate the momentum structure by using the energy-integrated mode. From Eq.2.25, and using $h\nu_{in} = h\nu_{out}$ (elastic scattering), the magnitude of the exchanged momentum can be written as

$$Q = |\mathbf{Q}| = 2q_{in} \times \sin(\theta_{sc}/2),$$

where θ_{sc} is the scattering angle. $\mathbf{Q}$ can be decomposed along the plane defining the sample surface, into its in-plane $\mathbf{Q}_{||}$ and out-of-plane $\mathbf{Q}_{\perp}$ components. This geometry is illustrated in Fig.2.6(d) and the experimental scheme in Fig.2.6(c).

The experimental signal in XRD and RXS can be composed of both resonant and non-resonant contributions. In the two possible regimes, $w_{fi}^{(XRD)} \gg w_{fi}^{(RXS)}$ or $w_{fi}^{(XRD)} \ll w_{fi}^{(RXS)}$, different phenomena are probed. In the case of non-resonant processes being dominant, the signal is proportional to the atomic number (Z) of the sample. This is because all electrons contribute equally to the signal, and the diffraction signal is dominated by the core electrons, which usually outnumber the valence electrons. The exception to this is with lighter elements, which are not probed very effectively in XRD. Since core states are tightly bound to the parent nucleus, XRD is primarily used for structural studies, as it mainly probes the ionic lattice in reciprocal space. On the other hand, when the scattering process has a strong enhancement corresponding to a specific electronic transition, the signal bears the signature of the electronic distribution of the final state of that transition. This characteristic of resonant scattering allows it to be element-specific and orbital-selective. This capability has been established and employed in many different systems, such as charge-ordering in cuprates and cobaltates, and orbital-ordering in manganites, as it allows to study the spatial inhomogeneities of the valence electrons that characterize the presence of stripe order.

Chapter 3

Variational Monte Carlo

[1]Quantum Monte Carlo (QMC) methods are a family of numerical techniques used to simulate the behavior of quantum mechanical systems. They are based on the idea of using stochastic sampling from a given probability distribution to extract a large number of random configurations of the system, over which one can evaluate the physical quantities of interest.

QMC methods are particularly advantageous in that they are capable of accurately and reliably simulating complex systems with a large number of interacting particles, such as molecules or solids. This is important because such systems are often too complex to solve analytically, and QMC methods can provide accurate and reliable numerical results.

Variational Monte Carlo (VMC) is a specific type of QMC method that uses a trial wave function to approximate the true wave function of a quantum system. The trial wave function is chosen to have a simple form that is easy to calculate, but is also flexible enough to capture the essential physics of the system. Once the trial wave function is chosen, the random configurations of the system are extracted to estimate the ground state energy of the system. Through the process of *variational optimization*, the parameters of the trial wave function

[1]Main reference for this chapter: Becca, Sorella, *Quantum Monte Carlo approaches for correlated systems*[43].

are updated in order to minimize the energy and possibly capture the correct ground-state behaviour.

The energy is calculated by using the *variational principle*, which states that the ground state energy of a system is always lower than or equal to the energy of any other trial wave function, providing us with the path to find the best possible state.

An important advantage of this method is that quite general Hamiltonians, with many parameters, can be considered without affecting much the computational cost. On the other other hand, the form of the variational wave function is arbitrarily chosen, which may introduce a relevant bias that cannot be removed through the optimization procedure and therefore fails in capturing the true physical properties of the system.

3.1 The Variational Principle

At the very heart of VMC there is the variational principle, providing a lower bound for the exact variational ground-state energy.

Let the exact ground state of a given Hamiltonian $\mathcal{H}$ be $|\Upsilon_0\rangle$ with (ground-state) energy E_0, and $|\Psi_{var}\rangle$ a generic state that approximates it. The variational energy for the Hamiltonian can be defined as

$$E_{var} = \frac{\langle\Psi_{var}|\,\mathcal{H}\,|\Psi_{var}\rangle}{\langle\Psi_{var}|\Psi_{var}\rangle}. \tag{3.1}$$

Any state in the Hilbert space can be written as an expansion in terms of the eigenfunctions $|\Upsilon_i\rangle$ of $\mathcal{H}$, with energies E_i. Then

$$|\Psi_{var}\rangle = \sum_i |\Upsilon_i\rangle\,\langle\Upsilon_i|\Psi_{var}\rangle = \sum_i a_i\,|\Upsilon_i\rangle\,, \tag{3.2}$$

while the normalization condition reads

$$\langle\Psi_{var}|\Psi_{var}\rangle = \sum_i |a_i|^2 = 1. \tag{3.3}$$

By substituting the expansion of Eq.3.2 into Eq.3.1, we get that

$$\boxed{E_{var} - E_0 = \sum_{i\neq 0} |a_i|^2\,(E_i - E_0) \geq 0}. \tag{3.4}$$

When dealing with $|\Psi_{var}\rangle$, then, all computational efforts are focused on minimizing the variational energy E_{var}.

In principle, if the variational wave function were able to explore the whole Hilbert space, we would be able to reach at a certain point $|\Psi_{var}\rangle = |\Upsilon_0\rangle$. However, this is not feasible for practical purposes, as the computational cost would be huge. Consequently, one usually resorts to an *ansatz* for the wave function that lives in a subspace of the entire Hilbert space.

3.2 Quantum averages in VMC

At this point, we can start by discussing how averages of operators can be computed in the VMC scheme. First of all, we can fix a generic complete basis set $\{|x\rangle\}$ in the Hilbert space, assumed *orthogonal* and *normalized* for simplicity, such that

$$\sum_x |x\rangle\langle x| = \mathbb{1}. \tag{3.5}$$

Then, any quantum state $|\Psi\rangle$ can be written as

$$|\Psi\rangle = \sum_x |x\rangle\langle x|\,|\Psi\rangle = \sum_x \Psi(x)\,|x\rangle\,. \tag{3.6}$$

Similarly, given a generic operator $\mathcal{O}$, its expectation value over a variational wave function $|\Psi\rangle$ is given by

$$\langle\mathcal{O}\rangle = \frac{\langle\Psi|\,\mathcal{O}\,|\Psi\rangle}{\langle\Psi|\Psi\rangle} = \frac{\sum_x \langle\Psi|x\rangle\,\langle x|\,\mathcal{O}\,|\Psi\rangle}{\sum_x \langle\Psi|x\rangle\,\langle x|\Psi\rangle}. \tag{3.7}$$

This last equation, despite looking concise, is a sum over a number of terms exponential in the number of particles. As it is, it cannot be used to compute $\langle\mathcal{O}\rangle$ in practice. However, it can be rearranged in a form that makes it easy to deal with by standard Monte Carlo methods. Indeed

$$\langle\mathcal{O}\rangle = \frac{\sum_x |\,\langle\Psi|x\rangle\,|^2 \frac{\langle x|\mathcal{O}|\Psi\rangle}{\langle x|\Psi\rangle}}{\sum_x |\,\langle\Psi|x\rangle\,|^2} = \frac{\sum_x |\Psi(x)|^2 \mathcal{O}_L(x)}{\sum_x |\Psi(x)|^2}, \tag{3.8}$$

where the *local estimator* of the operator $\mathcal{O}$ has been defined as

$$\mathcal{O}_L(x) = \frac{\langle x|\,\mathcal{O}\,|\Psi\rangle}{\langle x|\Psi\rangle}. \tag{3.9}$$

What is important to note is that the quantity

$$\mathcal{P}(x) \coloneqq \frac{|\Psi(x)|^2}{\sum_{x'} |\Psi(x')|^2} \tag{3.10}$$

is non-negative for all configurations $|x\rangle$ and normalized ($\sum_x \mathcal{P}(x) = 1$), hence it can be interpreted as a probability. As a result, the quantum average of the operator $\mathcal{O}$ is equal to the statistical average of the random variable $\mathcal{O}_L(x)$ over the distribution $\mathcal{P}(x)$. This can be easily done in a Monte Carlo scheme, in which a sequence of N configurations $\{|x\rangle_i\}_{i=1,\dots,N}$ are generated by, for instance, a Markov chain[2], according to the desired probability distribution and

$$\boxed{\langle \mathcal{O} \rangle = \sum_x \mathcal{P}(x) \mathcal{O}_L(x) \approx \frac{1}{N} \sum_{n=1}^{N} \mathcal{O}_L(x_n)}. \tag{3.11}$$

Another important feature of the VMC approach is the *zero-variance property*. Consider the expectation value of the Hamiltonian, i.e. $\mathcal{O} = \mathcal{H}$, whose local estimator is the *local energy* defined by

$$e_L(x) = \frac{\langle x | \mathcal{H} | \Psi \rangle}{\langle x | \Psi \rangle}. \tag{3.12}$$

If the variational state $|\Psi\rangle$ coincides with one (not necessarily the ground state) of the eigenstates of $\mathcal{H}$ i.e. $\mathcal{H}|\Psi\rangle = E|\Psi\rangle$ it follows that the local energy is simply constant

$$e_L(x) = \frac{\langle x | \mathcal{H} | \Psi \rangle}{\langle x | \Psi \rangle} = E \frac{\langle x | \Psi \rangle}{\langle x | \Psi \rangle} = E. \tag{3.13}$$

Consequently, the random variable $e_L(x)$ exhibits no dependence on $|x\rangle$, indicating a variance of zero and a mean value E precisely equal to the eigenvalue, basically rendering $e_L(x)$ a deterministic variable. This scenario however is not typically encountered in generic correlated models. Nonetheless, in most cases, the variance of $e_L(x)$ reduces when the variational state $|\Psi\rangle$ more closely approximates an exact eigenstate, leading to reduced statistical fluctuations and improved numerical efficiency. It is an essential point to note that the zero-variance property is a unique feature of quantum expectation values, absent in classical computations where observables experience thermal fluctuations.

[2] Of course, after an equilibration time. This convergence is ensured by the detailed balance condition.

Comment

At first glance, computing the local estimator seems to be an exceedingly difficult task: indeed Eq.3.13 can be rewritten, using the completeness relation of Eq.3.5 as

$$e_L(x) = \sum_{x'} \langle x| \mathcal{H} |x'\rangle \frac{\langle x'|\Psi\rangle}{\langle x|\Psi\rangle}. \tag{3.14}$$

It entails a summation across all the states of the many-body Hilbert space. However, only a few terms contribute to the sum when the operator in the estimator of Eq.3.9 is local. For the present case, for the configuration $|x\rangle$, a non-zero matrix element $\langle x| \mathcal{H} |x'\rangle$ is associated with $O(L)$ configurations $|x'\rangle$. To illustrate, let us examine the fermionic Hubbard model. Using the local basis, $|x\rangle$ is linked to only a few other configurations that differ by one electron hopping from a given site to one of its neighbouring sites[3]. The maximum number of such processes is L times the number of bonds times 2 (owing to spin). Hence, computing the local estimator necessitates only a limited number of operations, typically proportional to the number of sites or particles.

3.3 Markov Chain Monte Carlo

Monte Carlo (MC) methods encompass a wide range of numerical algorithms that rely on repeated *random sampling* to solve various mathematical and physical problems. The main objective is typically to compute large sums or complicated integrals, and the novel approach is to bypass an exact enumeration or integration by generating random samples that are combined to provide an approximate solution. Therefore, the core of any MC approach lies in the process of sampling, which involves generating random configurations that are used to estimate the exact quantity of interest with high accuracy.

The basic idea behind this method is that any integral can be recasted as the expectation value of a random variable $f(\mathbf{x})$ over a probability distribution

[3]In our case, in which the Hubbard model allows also the hopping to the next-nearest-neighbours, the number of non-zero matrix elements $\langle x| \mathcal{H} |x'\rangle$ remains small.

$P(\mathbf{x})$. For the sake of generality, $\mathbf{x} \in \mathbb{R}^d$. Explicitly, consider the integral of a generic function $F(\mathbf{x})$

$$\mathcal{I} = \int d\mathbf{x} F(\mathbf{x}). \tag{3.15}$$

Then, it is always possible to split $F(\mathbf{x})$ as the ratio of a probability density $P(\mathbf{x})$ (with $P(\mathbf{x}) \geq 0$ and $\int d\mathbf{x} P(\mathbf{x}) = 1$) and a function $f(\mathbf{x}) = F(\mathbf{x})/P(\mathbf{x})$, such that

$$\mathcal{I} = \langle f(\mathbf{x}) \rangle = \int d\mathbf{x} f(\mathbf{x}) P(\mathbf{x}). \tag{3.16}$$

The central limit theorem guarantees that the *deterministic* integral $\mathcal{I}$ and the *stochastic* average $\langle f(\mathbf{x}) \rangle$ become equal when a large number N of samplings $\{\mathbf{x}_i\}_{i=1,\ldots,N}$ over $P(\mathbf{x})$ is considered. In symbols

$$\langle f(\mathbf{x}) \rangle = \int d\mathbf{x} f(\mathbf{x}) P(\mathbf{x}) \approx \frac{1}{N} \sum_i f(\mathbf{x}_i) \tag{3.17}$$

The meaning of this last equality can be understood as, for large N, the variable

$$\bar{f} = \frac{1}{N} \sum_i f(\mathbf{x}_i) \tag{3.18}$$

is a normally (Gaussian) distributed variable, with mean equal to $\langle f(\mathbf{x}) \rangle$ and variance σ^2/N, where $\sigma^2 = \langle f^2(\mathbf{x}) \rangle - \langle f(\mathbf{x}) \rangle^2$. Therefore, as $N \to \infty$, $\bar{f} \to \langle f(\mathbf{x}) \rangle$, which is now a deterministic number since fluctuations decrease to zero with $1/\sqrt{N}$.

All in all, as long as the number of samplings is large enough, the error due to statistical fluctuations goes to zero and we have that

$$\boxed{\mathcal{I} = \int d\mathbf{x} f(\mathbf{x}) P(\mathbf{x}) = \langle \langle f(\mathbf{x}_i) \rangle \rangle}, \tag{3.19}$$

where $\langle \langle \ldots \rangle \rangle$ indicates the statistical average over many independent samples extracted from $P(\mathbf{x})$.

3.3.1 Markov Chains

Being the sampling process at the heart of the whole method, it is fundamental to perform it in the best possible way. In this section we discuss a powerful

(and probably the most popular) strategy to do so, able to deal with probability distributions that are difficult or impossible to sample analytically. The resulting scheme is referred to as Markov Chain Monte Carlo (MCMC).

To keep the notation simple, we will focus on a single discrete random variable x, but the generalization to continuous systems is straightforward. For instance, $\{x\}$ can represent the discrete Hilbert space of a many-body system on a finite lattice. However, the total number of possible configurations can be too large for direct sampling, making it necessary to adopt a probabilistic approach. This involves constructing a stochastic process, i.e. a random process that allows a configuration x_n to evolve over discrete iteration times n, according to a stochastic dynamics

$$x_{n+1} = F_n(x_1, \ldots, x_n, \xi_n). \tag{3.20}$$

Here, the function F_n governing the evolution over (discrete) time of the configuration x_n may include a dependence on all the previous configurations and its stochastic nature is related to the presence of a random variable ξ_n (distributed according to a certain probability density $\Xi(\xi_n)$). This makes the concept of "trajectory" not defined and the configurations x_n random variables. The goal is to define a suitable function F_n so that the configurations x_n will be distributed, after enough time n, according to the probability distribution we want to sample. It is important to note that the time evolution in this context is not connected to a true dynamics of the system. Rather, it is a method to reach a steady state that allows for the computation of static properties. A particular instance of Eq.3.20 is the Markov Chain (or Markovian process)

$$\boxed{x_{n+1} = F(x_n, \xi_n)} \tag{3.21}$$

in which the process bears memory of its previous state only, and F is taken time-independent. The time evolution is then governed by the (conditional) transition probability $\omega(x'|x)$ (such that $\omega(x'|x) \geq 0 \ \forall x, x'$, and $\sum_{x'} \omega(x'|x) = 1$) representing the probability of being in configuration x at time n and moving to x' at time $n+1$. This allows us to write the *Master equation* associated to

the Markov chain as[4]

$$P_{n+1}(x') = \sum_x \omega(x'|x) P_n(x), \tag{3.22}$$

describing the evolution of the marginal probability $P_n(x)$ as a function of n. Although the exact value of the random variable x is not determined, its probability distribution can instead be computed, by solving the Master equation, provided an initial condition $P_0(x)$.

3.3.2 Approach to equilibrium

The evolution of $P_n(x)$ along the Markov process raises the natural question of whether the sequence of distributions eventually converges to an equilibrium (stationary) distribution $P_{eq}(x)$ or not. With no loss of generality, one can assume $P_{eq}(x) > 0$ for all configurations x, as we can effectively ignore configurations for which $P_{eq}(x) = 0$. Two questions have to be addressed:

1. Does $P_{eq}(x)$ exist?
2. Starting from a given and *arbitrary* $P_0(x)$, is the convergence to $P_{eq}(x)$ guaranteed?

The first question requires Eq.3.22 to become

$$P_{eq}(x') = \sum_x \omega(x'|x) P_{eq}(x), \tag{3.23}$$

which is satisfied by requiring the sufficient (but not necessary) *detailed balance condition* (DBC):

$$\boxed{\omega(x|x')P_n(x') = \omega(x'|x)P_n(x)} \tag{3.24}$$

meaning that, in order to maintain a stable stationary condition, the number of processes undergoing a transition from x to x' has to be exactly compensated by

[4] An altrnative but equivalent formulation makes explicit the (discrete) time derivative of $P(x)$:

$$\frac{\partial P(x)}{\partial t} \approx \sum_{x \neq x'} \left[\omega(x|x')P_n(x') - \omega(x'|x)P_n(x)\right]$$

the same amount of reverse processes from x' to x. Notice that, since $P_{eq}(x) \neq 0$, if $\omega(x'|x) \neq 0$ then also $\omega(x|x') \neq 0$.

The DBC straightforwardly allows a stationary solution of the Master equation. Indeed, given $P_n(x) = P_{eq}(x)$ for some n, Eq.3.22 says

$$P_{n+1}(x') = \sum_x \omega(x'|x) P_{eq}(x) = P_{eq}(x') \sum_x \omega(x|x') = P_{eq}(x'). \tag{3.25}$$

Hence, the Master equation admits equilibrium/stationary (i.e. n-independent) solutions.

Luckily enough, also our second question has an affirmative answer. The discussion of formal proof is out of the scope of the present work, but can be found in [43]. Under the *ergodicity* condition (i.e. if it is possible to reach any state from any other state with a finite number of iterations of the Markov process), one can show that any initial $P_0(x)$ will converge towards the stationary distribution $P_{eq}(x)$. In symbols

$$\lim_{n\to\infty} P_n(x) = P_{eq}(x) \tag{3.26}$$

Practically, we assume that, after a *thermalization time* n_{therm}, the probability distribution $P_n(x)$ is converged to the equilibrium distribution $P_{eq}(x)$ and the configurations x_n (with $n > n_{\text{therm}}$) can be used to evaluate the quantity of interest. However, subsequent configurations are not independent, and it takes a finite number of steps to reduce the degree of correlation among them. The *correlation time* is the time needed to obtain essentially independent configurations. The correlation and thermalization times can be considered equal and are directly related to the spectrum of the transition probability.

3.3.3 Metropolis algorithm

We are now left with the task of establishing a stochastic dynamics such that the transition probability $\omega(x'|x)$ satisfies the DBC and, after a thermalization time, the configurations $\{x_n\}_{n\geq n_{\text{therm}}}$ are distributed according to a given $P_{eq}(x)$. The Metropolis algorithm (Metropolis *et. al.*,1957 (or Metropolis-Hastings, named

after W. Keith Hastings who generalized it in 1970), based on random walks and widely used in computational methods, involves accepting a new configuration if it results in a reduction in total energy. However, if there is an increase in the total energy, the new configuration is accepted only if it survives a biased random game governed by a Boltzmann factor. Otherwise, the old configuration is retained.

To begin with, $\omega(x'|x)$ is written as the product of a *trial probability* $T(x'|x)$ of proposing a new configuration x' while being in x, and an *acceptance probability* $A(x'|x)$. Explicitly

$$\omega(x'|x) = T(x'|x)A(x'|x). \tag{3.27}$$

One suitable choice for the acceptance probability, such that the DBC is satisfied is

$$A(x'|x) = \min\left\{1, \frac{P_{eq}(x')T(x|x')}{P_{eq}(x)T(x'|x)}\right\}. \tag{3.28}$$

As a check, take x and $x' \neq x$ such that $\frac{P_{eq}(x')T(x|x')}{P_{eq}(x)T(x'|x)} > 1$ (the opposite case, in which the previous ratio is < 1 is obtained analogously). As a consequence,

$$A(x'|x) = \min\left\{1, \underbrace{\frac{P_{eq}(x')T(x|x')}{P_{eq}(x)T(x'|x)}}_{>1}\right\} = 1 \tag{3.29}$$

and

$$A(x|x') = \min\left\{1, \underbrace{\frac{P_{eq}(x)T(x'|x)}{P_{eq}(x')T(x|x')}}_{<1}\right\} = \frac{P_{eq}(x)T(x'|x)}{P_{eq}(x')T(x|x')}. \tag{3.30}$$

Then the DBC can be directly verified

$$T(x'|x)A(x'|x)P_{eq}(x) = T(x|x')A(x|x')P_{eq}(x'). \tag{3.31}$$

In practice, being at time n in the configuration x_n, the Markov chain iteration is defined in these two steps:

1. Propose a move by extracting a new configuration x' according to $T(x'|x_n)$

2. Accept the trial move if, taken a random number $\eta \in [0,1)$, $\eta < A(x'|x_n)$, In this case $x_{n+1} = x'$. Otherwise, the move is rejected and $x_{n+1} = x_n$[5].

Pros of the Metropolis algorithm

Among the many important simplifications introduced by this strategy, it is worth mentioning that

- Only the ratio $P_{eq}(x')/P_{eq}(x)$ is needed for the computation of the acceptance probability of Eq.3.28. The normalization constant, usually very hard to compute, cancels out
- $T(x'|x)$ can be chosen freely. It can be very simple, symmetric or not. If x and x' are too similar, the rejection mechanism fails and the configurations stay highly correlated. Conversely, if they are too different, correlations are suppressed but too many moves are discarded. In general, in strongly correlated models, a 10% acceptance ratio is already good but still the configurations are correlated.

3.3.4 Metropolis algorithm for electron systems

The general procedure described in the previous section can now be made explicit for an electron system with N_e electrons. If $\Psi(x) = \langle x|\Psi\rangle$ is our variational wave function, with $|x\rangle$ the full many-electron configuration, we can define $P(x) = |\Psi(x)|^2$ according to the usual probabilistic interpretation of the wave function.

A common choice for the trial wave function for electron systems, which must be flexible enough to account for correlations, fluctuations in the *particle*

[5] As an example in classical physics, consider $P_{eq}(x) = \frac{1}{Z}\exp\{-\beta E(x)\}$ a Boltzmann distribution. Then, $A(x'|x_n) = \min\{1, \exp\{-\beta[E(x') - E(x_n)]\}\} = \min\{1, \exp\{-\beta\Delta E\}\}$. If $\Delta E < 0$, $\exp\{-\beta\Delta E\} < 1$ and the new configuration is always accepted. In the opposite case, an energetically costly configuration is accepted with probability proportional to the Boltzmann weight (i.e. exponentially small).

density n[6] and all their different phases, while remaining easy to handle, is the *Jastrow-Slater state*, given by

$$|\Psi_J\rangle = \mathcal{J}\,|\Phi_0\rangle\,, \tag{3.32}$$

where $|\Phi_0\rangle$ is a generic, fermionic non-interacting state and $\mathcal{J}$ is the *Jastrow factor* taking into account the electron correlation. On a lattice, $\mathcal{J}$ takes the form

$$\mathcal{J} = \exp\left\{-\frac{1}{2}\sum_{i,j} v_{ij}(n_i - n)(n_j - n)\right\}. \tag{3.33}$$

Here, v_{ij} is a pseudo-potential for the density-density correlations and has to be optimized for all possible distances $|i-j|$. The function of the long-range tail in the Jastrow factor is to produce a bound state between holons and doublons. While this may hinder conduction, it does allow for local density fluctuations.

A case that is both simple and important is when $\mathcal{J}$ includes density-density correlations only, and not density fluctuations. In this case

$$\mathcal{J} = \exp\left\{-\frac{1}{2}\sum_{i,j} v_{ij} n_i n_j\right\}. \tag{3.34}$$

The two definitions of the Jastrow factor are essentially the same, except for a multiplicative factor that is not relevant, for systems with conserved number of particles.

Once defined the wave function, the algorithm proceeds as follows:

1. Select randomly two sites i and j and the spin component σ along the quantization axis. The new configuration in which one electron with spin σ hops from i to j, defines the trial probability $T(x'|x)$;

2. Compute the acceptance probability $A(x'|x)$ of the new configuration. Otherwise, repeat the previous step if the move is not possible;

3. Generate a random number η and accept the new configuration if $\eta < A(x'|x)$. Reject it otherwise;

[6] Fluctuations manifest themselves as the creation of doublons(doubly-occupied sites) and holons (empty sites).

4. Compute the quantities of interest (the local energy for instance) every N_e steps, in order to have uncorrelated configurations;

5. Go back to 1.

All the configurations $\{x_1, \ldots, x_N\}$ extracted after the thermalization time, will be distributed according to $P(x)$ and the estimate for the variational energy is given by

$$E = \lim_{N\to\infty} \frac{1}{N} \sum_{i=1}^{N} e_L(x_i) \tag{3.35}$$

In principle, we would like to deal with configurations as uncorrelated as possible in order to have independent random variables, that are easier to handle. Configurations obtained through a Markov process usually possess some degree of correlation, since a trial configuration completely uncorrelated from the current one has a very low acceptance probability. A common method to circumvent the problem, lowering the correlations, is the so-called *binning technique*, in which the data set is divided into N_{bin} bins, each of length $L_{bin} = N/N_{bin}$, so that the average over the bins is (trivially) the original average, but the probability distribution of the binned variables changes. As L_{bin} increases, the binned variables become more and more uncorrelated and eventually independent random variables.

3.4 The Stochastic Reconfiguration Method

We have already pointed out that the variational wavefunction *ansatz* contains a number of parameters to be optimized in order to reach the best approximation possible of the ground state, following the variational principle summarized in Eq.3.4. In this chapter we discuss the strategy to perform this optimization, namely the so-called Stochastic Reconfiguration method [44], within Jastrow-Slater wave functions. It is worth mentioning that an optimization via the zero-variance property, discussed in Sec.3.2, has been shown to yield less accurate expectation values with respect of those from energy minimization [45].

Let us call the "initial" Jastrow-Slater wave function $\left|\Psi(\alpha_k^0)\right\rangle$, $\left|\Psi^0\right\rangle$ for simplicity in the following, which depends on a set of p variational parameters $\{\alpha_k\}_{k=1,\dots,p}$. To improve its variational energy, we can apply to it the projection operator $(\Lambda - \mathcal{H})$, with Λ an appropriate constant energy shift, such that

$$|\Psi_\Lambda\rangle = (\Lambda - \mathcal{H}) \left|\Psi^0\right\rangle. \tag{3.36}$$

Since, in general $|\Psi_\Lambda\rangle$ is not written in the Jastrow-Slater form, the idea is to look for the best quantum state $|\Psi'\rangle \equiv |\Psi(\alpha_k')\rangle$ that approximates it. This can be done by considering small variations $\{\delta\alpha_k\}$ of the parameters $\{\alpha_k\}$

$$\alpha_k' = \alpha_k^0 + \delta\alpha_k \tag{3.37}$$

related to a change of the wave function, at first order in $\{\delta\alpha_k\}$, as follows

$$|\Psi'\rangle = \delta\alpha_0 \left|\Psi^0\right\rangle + \sum_{k=1}^{p} \delta\alpha_k \frac{\partial}{\partial\alpha_k} \left|\Psi^0\right\rangle + \mathcal{O}(\delta\alpha_k^2), \tag{3.38}$$

where $\delta\alpha_0$ has to match the normalization condition. We define now the local operators $O(\alpha_k^0)$ on the configuration $|x\rangle$ as the log-derivatives with respect to the parameters

$$O_k(x) = \frac{\partial}{\partial\alpha_k^0} \ln \left\langle x\middle|\Psi^0\right\rangle = \frac{1}{\Psi^0(x)} \frac{\partial\Psi^0(x)}{\partial\alpha_k^0}, \tag{3.39}$$

with $O_0(x) \equiv \mathbb{1}$, so that $|\Psi'\rangle$ can be compactly written as

$$|\Psi'\rangle = \delta\alpha_0 \left|\Psi^0\right\rangle + \sum_{k=1}^{p} \delta\alpha_k O_k \left|\Psi^0\right\rangle = \sum_{k=0}^{p} \delta\alpha_k O_k \left|\Psi^0\right\rangle. \tag{3.40}$$

Within the method, we now impose that the projection of $|\Psi_\Lambda\rangle$ and $|\Psi'\rangle$ onto the subspace defined by $O_j \left|\Psi^0\right\rangle$ $(j = 0, \dots, p)$ coincide, i.e.

$$\boxed{\left\langle\Psi^0\middle| O_j \middle|\Psi'\right\rangle = \left\langle\Psi^0\middle| O_j \middle|\Psi_\Lambda\right\rangle}, \tag{3.41}$$

ensuring that the energy computed on $|\Psi'\rangle$ is lower than that on $\left|\Psi^0\right\rangle$. By substituting Eq.3.36 and Eq.3.40 into the *ansatz* 3.41 we obtain:

$$\sum_{k=0}^{p} \delta\alpha_k \langle O_j O_k\rangle = \langle O_j(\Lambda - \mathcal{H})\rangle, \tag{3.42}$$

where $\langle \dots \rangle = \langle \Psi^0 | \dots | \Psi^0 \rangle$. Specifically, for $j = 0$, the previous equation reduces to

$$\sum_{k=0}^{p} \delta\alpha_k \langle O_k \rangle = \Lambda - \langle \mathcal{H} \rangle, \tag{3.43}$$

while for $j = 1, \dots, p$ we get

$$\sum_{k=0}^{p} \delta\alpha_k \langle O_j O_k \rangle = \Lambda \langle O_j \rangle - \langle O_j \mathcal{H} \rangle. \tag{3.44}$$

By taking out the term for $k = 0$, the two equations become, respectively,

$$\delta\alpha_0 + \sum_{k=1}^{p} \delta\alpha_k \langle O_k \rangle = \Lambda - \langle \mathcal{H} \rangle \tag{3.45}$$

and

$$\delta\alpha_0 \langle O_j \rangle + \sum_{k=1}^{p} \delta\alpha_k \langle O_j O_k \rangle = \Lambda \langle O_j \rangle - \langle O_j \mathcal{H} \rangle. \tag{3.46}$$

Being the term $\delta\alpha_0$ related to the normalization of the wave function only, it does not affect any physical observable of the system. Thus, we can solve for $\delta\alpha_0$ in order to obtain

$$\sum_{k=1}^{p} \delta\alpha_k [\langle O_j O_k \rangle - \langle O_j \rangle \langle O_k \rangle] = \langle O_j \rangle \langle \mathcal{H} \rangle - \langle O_j \mathcal{H} \rangle, \tag{3.47}$$

which is a linear systems in the unknowns $\{\delta\alpha_k\}$ that, in a compact form, becomes

$$\boxed{\sum_{k=1}^{p} \delta\alpha_k S_{jk} = f_j}, \tag{3.48}$$

where we have defined $S \in \mathbb{R}^{p \times p}$ a symmetric, semi positive-definite covariance matrix

$$S_{jk} \doteq \langle O_j O_k \rangle - \langle O_j \rangle \langle O_k \rangle \tag{3.49}$$

and a vector ($\in \mathbb{R}^p$) of generalized forces[7]

$$f_j = \langle O_j \rangle \langle \mathcal{H} \rangle - \langle O_j \mathcal{H} \rangle. \tag{3.50}$$

[7] They are indeed related to the derivative of the variational energy w.r.t. the variational parameters:

$$\frac{\partial E}{\partial \alpha_j} = \frac{\partial}{\partial \alpha_j} \frac{\langle \Psi^0 | \mathcal{H} | \Psi^0 \rangle}{\langle \Psi^0 | \Psi^0 \rangle} = -2 f_j$$

.

All in all, the method consists in performing a MC simulation with *fixed* parameters, in which both S_{jk} and f_j are computed stochastically and their values are used to solve the linear system of Eq.3.48. The parameters are then updated as follows

$$\boxed{\begin{cases} \delta\alpha_k = \sum_{j=1}^{p} S_{kj}^{-1} f_j \\ \alpha_k' = \alpha_k^0 + \tau\delta\alpha_k \end{cases}}. \tag{3.51}$$

The parameter τ is chosen such that is large enough to ensure a fast convergence, without making the algorithm unstable when it becomes *too* large.

Finally, the effectiveness of this scheme can be shown in computing the energy. By taking τ small enough and expanding up to linear order in τ, we get

$$E(\Psi') = E(\Psi^0) + \sum_{k=1}^{p} \frac{\partial E(\Psi^0)}{\partial \alpha_k}\delta\alpha_k + \mathcal{O}(\tau^2) \tag{3.52}$$

implying

$$E(\Psi') - E(\Psi^0) = -\sum_{k,j=1}^{p} S_{kj}^{-1} f_j f_k + \mathcal{O}(\tau^2) \leq 0. \tag{3.53}$$

This last step, using the fact that also the inverse of S_{jk} is semi-positive definite, shows that, on average, the energy decreases at each step at linear order in τ. The minimum is certainly reached when all the forces disappear.

3.5 VMC for Cuprates

This section is finally devoted to the description of the research conducted in the context of this thesis. Specifically, we define and describe the key quantities that constitute the core of the VMC wave function for stripe order and superconductivity in Cuprates. The results of our empirical analysis and their implications will be discussed later in Ch.4. The present work is built upon the previous investigation by VMC simulations of the metallic/insulating character of stripes and their relation with superconductivity in the doped Hubbard model (Tocchio *et. al.* [46]), and a subsequent work by Marino *et. al.* [47]

inspecting its behaviour in its extended version (i.e. by including also next-nearest-neighbours hopping) for different values of the hopping parameters at fixed doping[8].

The single-band Hubbard model on the square lattice is the simplest model able to capture the essential characteristics of the cuprates' phase diagram. This model comprises the on-site electron-electron repulsion U and the nearest-neighbor hopping t. However, obtaining accurate approximations or exact solutions for low-energy excitations and the ground state is a challenging task, particularly for the electron densities that generate unconventional superconductivity. Various analytical and numerical methods have been employed, leading to different conclusions since several states with comparable energy levels have been proposed [48]. It is then crucial to assess the role of extra parameters in promoting tendencies towards stripes or superconductivity. Consequently, we start by considering the *extended Hubbard model*, which comprises also the next-nearest-neighbor hopping t', as justified in Sec.1.4.3 [13].

$$\mathcal{H} = -t \sum_{\langle R,R'\rangle,\sigma} c^{\dagger}_{R\sigma} c_{R'\sigma} - t' \sum_{\langle\langle R,R'\rangle\rangle,\sigma} c^{\dagger}_{R\sigma} c_{R'\sigma} + \text{H.c} + U \sum_{R} n_{R\uparrow} n_{R\downarrow}, \quad (3.54)$$

where $c^{\dagger}_{R\sigma}$ and $c_{R\sigma}$ respectively denote the creation and annihilation operator of an electron with spin σ on site R, while $n_{R\sigma} = c^{\dagger}_{R\sigma} c_{R\sigma}$ is the electron density per spin σ on site R. By calling N the total number of electrons and L the total number of sites, the electron density is $n = N/L$[9]. The hole doping is $x = 1 - n$. In the following, $\mathbf{R} = (x, y)$ will denote the coordinates of the sites. In order to set the energy scale, t is set to 1 and, in the following, only the ratio t'/t will be considered.

Our numerical simulations rely on appropriate variational wave functions that incorporate correlations, through the Jastrow factor on top of a Slater determinant or a BCS state. Additionally, *backflow correlations* [49, 50, 51], are integrated into the model. The latter play a critical role in constructing

[8] Both are the main reference for this section.

[9] Note that at half filling $N = L \Rightarrow x = 0$.

reliable variational states that are comparable in accuracy to other state-of-the-art numerical methods [52, 53].

The main idea behind the backflow terms is to include correlation effects directly in the variational wave function, and not only as a multiplicative term as in the Jastrow factor. The single-particle eigenstates of the mean-field Hamiltonian (for instance the BCS Hamiltonian) $\phi_k(\mathbf{r}_{i,\sigma})$ are modified according to the electronic configuration on the lattice:

$$\phi_k^b(\mathbf{r}_{i,\sigma}) \equiv \tilde{\epsilon}\phi_k(\mathbf{r}_{i,\sigma}) + \eta_1 \sum_{j\in\partial i} D_i H_j \phi_k(\mathbf{r}_{j,\sigma}) + \eta_2 \sum_{j\in\partial^2 i} D_i H_j \phi_k(\mathbf{r}_{j,\sigma}), \quad (3.55)$$

where k labels the single-particle eigenstates and $\tilde{\epsilon}$,η_1 and η_2 are variational parameters to be optimized. $D_i = n_{i\uparrow}n_{i\downarrow}$ and $H_i = h_{i\uparrow}h_{i\downarrow}$ (with $h_{i\sigma} = 1 - n_{i\sigma}$) are the number of doublons and holons, respectively. The notation $j \in \partial i$ and $j \in \partial^2 i$ for sites i and j is indicating nearest- and next-nearest-neighbours. Furthermore, additional terms useful in the intermediate-coupling regime and related to all possible hopping processes can be included in the previous equation.

The wave function is defined as

$$|\Psi\rangle = \mathcal{J}\,|\Phi_0\rangle \quad (3.56)$$

where, consistently with the notation of the previous sections, $\mathcal{J}$ is the density-density Jastrow factor of Eq.3.34 that, with the current indices, is written as

$$\mathcal{J} = \exp\left\{ -\frac{1}{2} \sum_{R,R'} v_{RR'} n_R n_{R'} \right\} \quad (3.57)$$

and $|\Phi_0\rangle$ a state obtained from the ground state of an auxiliary non-interacting Hamiltonian $\mathcal{H}_{aux}$ with the introduction of backflow correlations.

Explicitly, $\mathcal{H}_{aux}$ is the sum of different terms

$$\mathcal{H}_{aux} = \mathcal{H}_0 + \mathcal{H}_{charge} + \mathcal{H}_{spin} + \mathcal{H}_{AF} + \mathcal{H}_{BCS}. \quad (3.58)$$

The first term consists of the *kinetic energy* of the electrons in the Hubbard model

$$\mathcal{H}_0 = -t \sum_{\langle R,R'\rangle,\sigma} c^\dagger_{R\sigma} c_{R'\sigma} - \tilde{t'} \sum_{\langle\langle R,R'\rangle\rangle,\sigma} c^\dagger_{R\sigma} c_{R'\sigma} + \text{H.c.} \quad (3.59)$$

The second and third term take into account *striped states both in charge and spin* along the x direction in the following way

$$\mathcal{H}_{charge} = \Delta_C \sum_{R'} \cos\left[Q(x - x_0)\right] \left(c^\dagger_{R\uparrow} c_{R\uparrow} + c^\dagger_{R\downarrow} c_{R\downarrow}\right) \tag{3.60}$$

and

$$\mathcal{H}_{spin} = \Delta_S \sum_{R} (-1)^{x+y} \sin\left[\frac{Q}{2}(x - x_0)\right] \left(c^\dagger_{R\uparrow} c_{R\uparrow} - c^\dagger_{R\downarrow} c_{R\downarrow}\right) \tag{3.61}$$

If $x_0 = 1/2$ the stripes are symmetric with respect to the bond halfway in between two neighboring lattice sites, hence they are called *bond centered*. Conversely, for $x_0 = 0$, the stripes are called *site centered*, as the symmetry axis lies exactly on a lattice site. The periodicity of the charge modulation in both cases is given by $\lambda = 2\pi/Q$. On the other hand, the spin modulation has a π-phase shift (see the scheme 1.37) across the sites with maximal hole density, resulting in a spin modulation of $2\lambda = 4\pi/Q$ when λ is even and $2\pi/Q$ when λ is odd. The spin modulation along the y direction is assumed to have Néel order in all cases.

The fourth term includes antiferromagnetism by *standard Néel order*

$$\mathcal{H}_{AF} = \Delta_{AF} \sum_{R} (-1)^{x+y} \left(c^\dagger_{R\uparrow} c_{R\uparrow} - c^\dagger_{R\downarrow} c_{R\downarrow}\right) \tag{3.62}$$

while the last one introduces the *BCS electron pairing*

$$\mathcal{H}_{BCS} = \sum_{R,\eta=x,y} \Delta_{R,R+\eta} \left(c^\dagger_{R,\uparrow} c^\dagger_{R+\eta,\downarrow} - c^\dagger_{R,\downarrow} c^\dagger_{R+\eta,\uparrow}\right) + \text{H.c.} - \mu \sum_{R,\sigma} c^\dagger_{R\sigma} c_{R\sigma} \tag{3.63}$$

where μ is a generic chemical potential and, eventually, also the pairing amplitude may be periodically modulated in space

$$\Delta_{R,R+x} = \Delta_x \left|\cos\left[\frac{Q}{2}(x + \frac{1}{2} - x_0)\right]\right| \qquad \Delta_{R,R+y} = -\Delta_y \left|\cos\left[\frac{Q}{2}(x - x_0)\right]\right| \tag{3.64}$$

which, in the case with $Q = 0$ corresponds to a uniform pairing amplitude (with d-wave symmetry).

The optimizations of the variational wave functions are performed on two different states:

- *striped state*, with charge and spin modulations. This state is set by imposing $\Delta_{AF} = 0$ and a given stripe wavelength λ, while the remaining parameters Δ_x, Δ_y, Δ_C, Δ_S, t', μ, the pseudo-potentials in $\mathcal{J}$ and the backflow parameters are optimized;

- *uniform state*, appropriate to study homogeneous superconducting states. This state is set by imposing $\Delta_C = \Delta_S = 0$ and a uniform pairing, while all the other parameters are optimized. Néel order can eventually emerge whenever $\Delta_{AF} \neq 0$.

The presence of charge and spin inhomogeneities is unveiled by computing the *static structure factors*

$$N(\mathbf{q}) = \frac{1}{L}\sum_{R,R'} \langle n_R n_{R'} \rangle e^{i\mathbf{q}\cdot(\mathbf{R}-\mathbf{R}')} \quad , \quad S(\mathbf{q}) = \frac{1}{L}\sum_{R,R'} \langle S^z_R S^z_{R'} \rangle e^{i\mathbf{q}\cdot(\mathbf{R}-\mathbf{R}')}, \tag{3.65}$$

where $\langle \dots \rangle = \langle \Psi | \dots | \Psi \rangle$ and $S^z_R = \frac{1}{2}\left(c^\dagger_{R\uparrow}c_{R\uparrow} - c^\dagger_{R\downarrow}c_{R\downarrow}\right)$ is the spin operator along the z direction. A peak (divergent in the thermodynamic limit) at a given $\mathbf{q}$ indicates an ordering at the related wavelength.

From the small-q behaviour of $N(\mathbf{q})$ it is also possible to assess the metallic or insulating character of the ground state. Indeed, it is possible to find a relation between the spectrum of the charge excitations and $N(\mathbf{q})$ [50], with a charge gap found to be

$$E_q \propto \lim_{q\to 0} \frac{|q|^2}{N(q)}. \tag{3.66}$$

The metallic phase is characterized by $N(q) \sim q$ for $q \to 0$, implying a vanishing energy gap. The insulating phase, instead, is characterized by $N(q) \sim q^2$ for $q \to 0$ and consequently a finite charge gap.

Finally, by computing the correlation functions between Cooper pairs at a distance r, the existence of superconductivity can be investigated. We chose to consider singlets along the y direction and observe the change in strength of the correlations along the x direction. Explicitly

$$D(r) = \left\langle \left(c^\dagger_{R,\uparrow}c^\dagger_{R+y,\downarrow} - c^\dagger_{R,\downarrow}c^\dagger_{R+y,\uparrow}\right)\left(c^\dagger_{R',\uparrow}c^\dagger_{R'+y,\downarrow} - c^\dagger_{R',\downarrow}c^\dagger_{R'+y,\uparrow}\right)\right\rangle, \tag{3.67}$$

with $R' = R + rx$. In the superconducting phase, this object factorizes as $\langle \dots \rangle \langle \dots \rangle$, remains finite at large r and proportional to the the order parameter squared. Conversely, when superconductivity is absent, $D(r)$ decays to zero at large r.

Comment on the site- and bond-centered nature of the stripes

From a mathematical point of view, site- and bond-centered stripes are well-defined: in the definitions of $\mathcal{H}_{charge}$ and $\mathcal{H}_{spin}$ the parameter $x_0 = 0$ for the former case and $x_0 = 1/2$ for the latter. When the stripes have an even wavelength λ, the two definitions are clearly related to having the symmetry axis laying on a site or on a bond[10]. For odd wavelengths, on the other hand, such geometrical meaning is much more ambiguous. To see why, we begin by looking at the case with λ even, fixing as an example $\lambda = 6$. In the following figures, symmetries with respect to a bond will be highlighted in red, while those with respect to a site in blue.

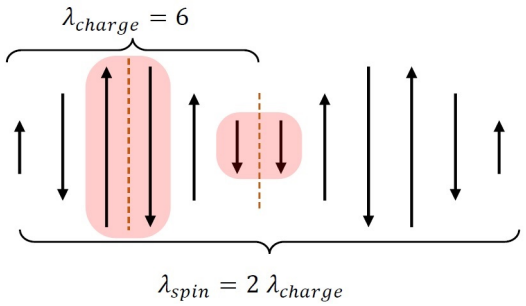

Figure 3.1: Pictorial representation of a stripe with $\lambda = 6$, bond-centered.

In Fig.3.1 a bond-centered stripe with $\lambda = 6$ is depicted. This clearly corresponds to a symmetry axis halfway in between two neighboring lattice sites. The situation is equally unambiguous when its site-centered counterpart is considered in Fig.3.2.

[10] Considering such symmetries with respect to the sites or bonds where amplitude modulation is the largest or the smallest does not make any difference.

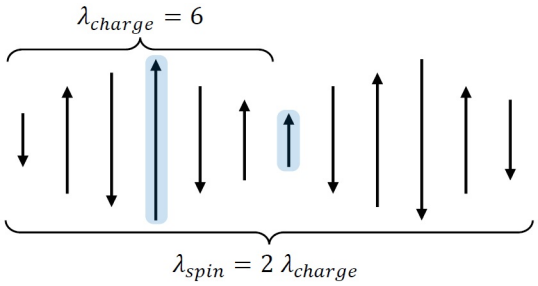

Figure 3.2: Pictorial representation of a stripe with $\lambda = 6$, site-centered.

Taking, as customary, the largest or the smallest amplitude modulation as a reference for the periodicity, the symmetry axis is located on the lattice site. Note again how the $\pi-$shift doubles the periodicity of the spin modulation.

The situation is instead not so clear when λ is odd, fixing as an example $\lambda = 5$. As before, a bond-centered stripe is shown in Fig.3.3.

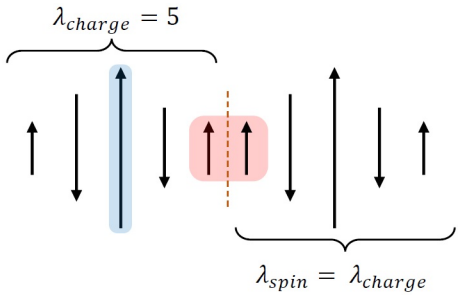

Figure 3.3: Pictorial representation of a stripe with $\lambda = 5$, bond-centered.

This time, there is no way to enforce a symmetry with respect to the bond without having also a symmetry with respect with a site. This is equally true when considering a site-centered stripe with λ odd, as plotted in Fig.3.4: the site-centered symmetry cannot exist without a bond-centered one.

We can then say that for λ odd, the idea of a site- or bond-centeredness of the stripes is ill-defined. However, as we will report in Ch.4, our choice has been to consider site-centered stripes when λ is odd.

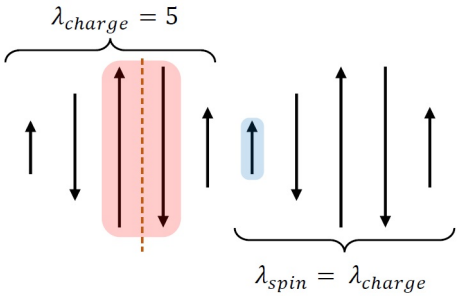

Figure 3.4: Pictorial representation of a stripe with $\lambda = 5$, site-centered.

Chapter 4

Results

In this chapter we finally discuss the results obtained by means of VMC techniques to investigate the instauration of stripes in the single-band Hubbard model on the square lattice with both nearest-(t) and next-nearest-(t') neighbour hopping. In Ch.1 we have discussed the main features of cuprates and justified why this model well describes these materials, while Ch.2 gave us insights on the two main methods to support via experiments the theoretical and numerical evidences for stripe order.

In the present work we empirically study the instauration of superconductivity and stripes with different wavelengths λ and different character (bond- or site-centered) when changing the hole-doping x. We consider two typical values of the hopping parameter for cuprates ($t'/t = -0.25$ and $t'/t = -0.4$) in order to see how larger values of $|t'/t|$ affect the stripe order. The on-site Coulomb repulsion $U/t = 8$, kept fixed throughout the simulations, is chosen to ensure strong enough correlations. Indeed, in [47] it is shown that for smaller values of U/t, such as $U/t \lesssim 4$, the striped wave functions are not stable and converge to the uniform state with vanishing parameters Δ_C and Δ_S.

Our simulations are conducted on ladders with $L = L_x \times 6$ sites and periodic boundary conditions in both x and y directions. To match the charge and spin patters in the cluster, we choose $L_x = 2k\lambda$, where $k \in \mathbb{Z}$ and λ the wave-

length associated to the modulations. This geometry is expected to capture the behaviour of truly two-dimensional clusters [53], while allowing to accommodate long stripes along the L_x rungs. Stripes with even values of λ are taken bond-centered, while those with odd values of λ are site-centered. However, by comparing the two configurations we found that bond- and site-centered stripes are essentially degenerate in energy (within the error bar) for each value of λ (odd or even).

The Monte Carlo simulation is initialized with an arbitrary[1] set of variational parameters that, at each MC step are updated according to the Stochastic Reconfiguration method (see Sec.3.4) and consequently the variational energy decreases until, eventually, oscillates around a stable value bounded from below by the exact ground-state energy, according to the Variational Principle, discussed in Sec.3.1. In Fig.4.1 a typical curve for the variational (after some binning) energy along the optimization process is shown. In computing the average variational energy, the "transient" part is discarded.

From the figure it is safe to assume that the variational energy converged to the minimum. A safety check is performed by looking at the curves for the variational parameters, to make sure they have approached a stable value too. A few of them, as an example, are reported in Fig.4.2. Once the energy and all the parameters converge to stable values, the *optimization run* can be concluded. Their values are fixed to their averages and a *run at fixed parameters* is performed to compute, for instance, the quantum averages needed for the correlation function or the superconducting order parameter.

4.1 Optimal state

In this section we work out the optimal state for different values of hole-doping x and the two next-nearest-neighbour hopping t' values. Chosen a value for the hole-doping, the different wave functions, i.e. striped states for various λ and the uniform state, are compared by looking at their variational energies. The

[1] But still reasonable enough to avoid numerical instabilities.

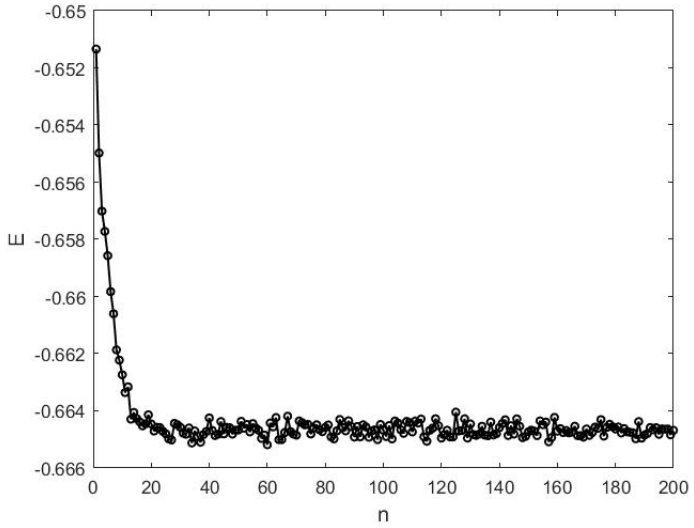

Figure 4.1: Value of the variational energy E along the optimization process. Here, each data point represents a bin over 1000 MC steps.

optimal state is the one corresponding to the lowest variational energy.

Both *commensurate* and *incommensurate* doping values have been considered. By "commensurate" doping we refer to the introduction of an integer number of holes every $1/x$ lattice sites; conversely, this number is noninteger for "incommensurate" doping values.

We start by considering the case $t'/t = -0.25$. The energy per site, in units of t, as a function of x is reported in Table 4.1. Here, we compare the energy for the best striped state E_{stripe} with that of the uniform state E_{uniform} for a broad range of doping values.

The striped state is almost always energetically favourable. As x increases, the wavelength λ decreases more and more until, at the large doping $x = 1/3$, the striped state and the uniform state become energetically indistinguishable. When discussing the behaviour of the gap parameters in Sec.4.2, we will show that this effectively corresponds to a *melting* of the stripe.

The second set of simulations involved the same search for the optimal state

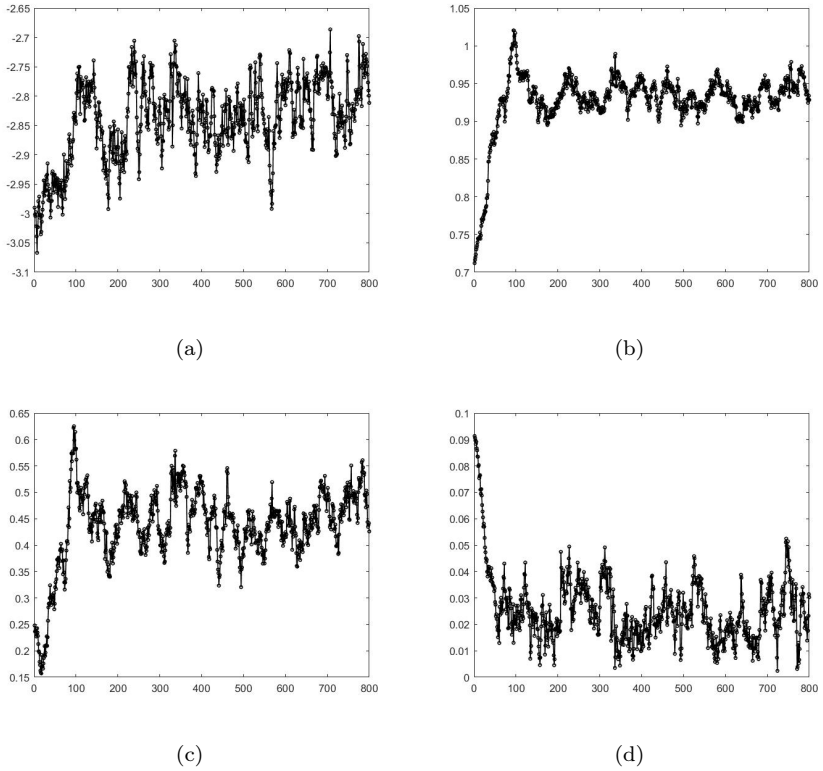

Figure 4.2: Value of a few variational parameters along the optimization process via Stochastic Reconfiguration.

x	E_{stripe}	E_{uniform}	Δ_E
1/12	-0.6646 ($\lambda = 8$)	-	-
1/10	-0.6920 ($\lambda = 7$)	-	-
1/8	-0.7322 ($\lambda = 5$)	-0.7239	-0.0082
1/6	-0.7936 ($\lambda = 4$)	-0.7847	-0.0088
1/5	-0.8280 ($\lambda = 3$)	-0.8260	-0.0020
1/4	-0.8749 ($\lambda = 3$)	-0.8727	-0.0021
1/3	-0.9197 ($\lambda = 3$)	-0.9197	0

Table 4.1: Energy per site (in units of t) for the best striped state E_{stripe} and the uniform state E_{uniform}, along with their relative difference $\Delta_E = E_{\text{stripe}} - E_{\text{uniform}}$, as a function of x for $t'/t = -0.25$. Data are shown for $L_x = 48$ for the stripes with $\lambda = 3, 4, 8$, $L_x = 40$ for the stripes with $\lambda = 5$ and $L_x = 70$ for the stripes with $\lambda = 7$. For the uniform state $L_x = 48$. The error bar on the energy is always smaller than $10^{-4}t$.

but at a larger value of $|t'/t|$, namely $t'/t = -0.4$. The results are reported in Table 4.2. The main effect of a larger hopping $|t'/t|$ is to suppress the stripe pattern and makes the optimal state converge to the uniform one faster. Indeed, already at $x = 1/4$, the striped state is no longer favourable and the uniform state is the optimal one.

4.2 Behaviour of the gap parameters

In Sec.3.5 we have introduced the gap parameters Δ_C, Δ_S and Δ_{AF} related to the "strength" of the charge, spin, and Néel order respectively. In this section we proceed by looking at their behaviour as the hole-doping increases in the case $t'/t = -0.25$, once the parameters converge after a long enough VMC simulation. Their values are reported in Table 4.3 and plotted in Fig.4.3.

For small doping, as also shown in Table 4.1, the striped state is well estab-

x	E_{stripe}	E_{uniform}	Δ_E
1/6	-0.7901 ($\lambda = 4$)	-0.7854	-0.0047
1/5	-0.8250 ($\lambda = 3$)	-0.8244	-0.0005
1/4	-0.8650 ($\lambda = 3$)	-0.8654	0.0004

Table 4.2: Energy per site (in units of t) for the best striped state E_{stripe} and the uniform state E_{uniform}, along with their relative difference $\Delta_E = E_{\text{stripe}} - E_{\text{uniform}}$, as a function of x for $t'/t = -0.4$. Data are shown for $L_x = 48$ for all the stripes and the uniform state. The error bar on the energy is always smaller than $10^{-4}t$.

x	λ	Δ_C	Δ_S	Δ_{AF}
1/12	8	0.4498±0.0024	0.9341±0.001	0.5396±0.0008
1/10	7	0.4165±0.0019	0.8540±0.0005	0.4605±0.0006
1/8	5	0.3828±0.0015	0.8437±0.0006	0.2526±0.0011
1/6	4	0.2113±0.0012	0.6559±0.0004	0.0148±0.0002
1/5	3	0.2068±0.0015	0.4933±0.0006	0.0001±0.0002
1/4	3	0.0739±0.0007	0.3842±0.0003	-0.0001±0.0001
1/3	3	-0.0003±0.0010	-0.0002±0.0002	-0.0002±0.0005

Table 4.3: Value of the gap parameters Δ_C and Δ_S for the best striped state and Δ_{AF} for the uniform state, as a function of x for $t'/t = -0.25$. The λs refer to the optimal striped state.

lished and indeed Δ_C and Δ_S are finite. This corresponds to well-defined order in both charge and spin. Also the uniform state, despite not being the optimal one, is able to develop Néel antiferromagnetism in the underdoped regime, as indicated by a finite Δ_{AF}.

As x increases, we see that all these parameters decrease monotonically until, at large x they become much smaller and eventually negligible. This

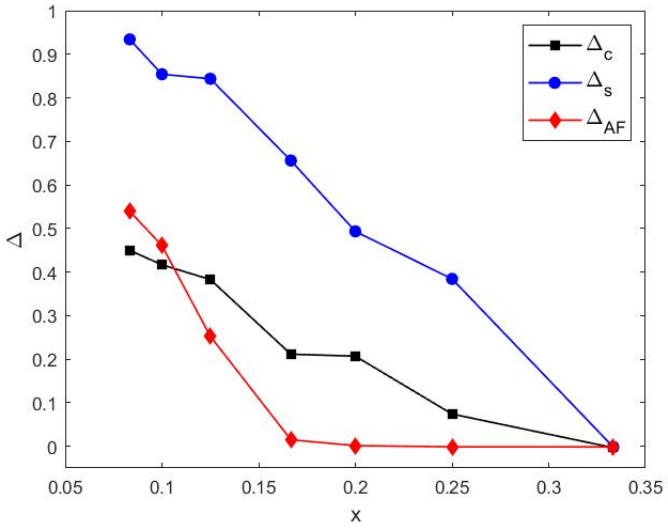

Figure 4.3: Behaviour of Δ_C and Δ_S for the best striped state and Δ_{AF} for the uniform state, as a function of x for $t'/t = -0.25$. The error bars, reported in Table 4.3, are not visible.

corresponds, for the striped states, to the absence of any order: the stripe "melts" and effectively reduces to the uniform state. Hence the degeneracy in energy pointed out for $x = 1/3$.

Moreover, the weakening of correlations in charge and spin provides a justification for the shrinkage of the wavelength λ of the striped states. A long-range, periodic modulation, extending over many lattice sites, in fact, can be stabilized only by strong enough correlations; conversely, upon increasing the hole doping, only shorter stripes can eventually form.

4.3 Correlation functions

The actual presence of charge and spin order in the wave function can be directly detected in the static structure factors of Eqs.3.5, which exhibit clear peaks in this case. These peaks are present at $\mathbf{Q} = \left(\frac{2\pi}{\lambda}, 0\right)$ for $N(\mathbf{q})$ and

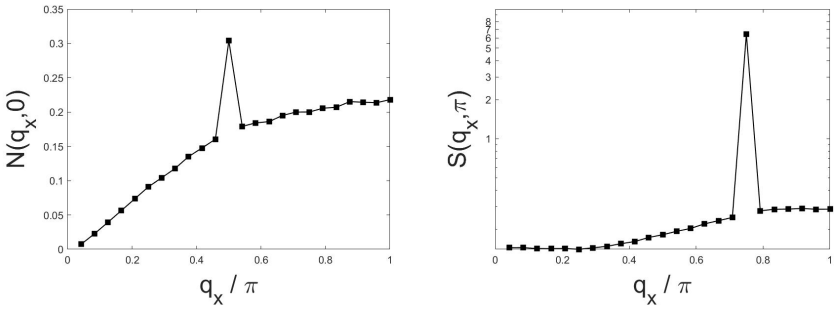

(a) (b)

Figure 4.4: *(a):* Static structure factor $N(\mathbf{q})$ as a function of q_x with $q_y = 0$. *(b):* Spin-spin correlation function $S(\mathbf{q})$ as a function of q_x with $q_y = \pi$ on a semi-log scale. Both quantities refer to the optimal striped state at $x = 1/6$, $t'/t = -0.25$ and $\lambda = 4$.

$\mathbf{Q} = (\pi(1 - 1/\lambda), \pi)$ for $S(\mathbf{q})$. Whenever the gap parameters Δ_C and Δ_S are finite, peaks in $N(\mathbf{q})$ and $S(\mathbf{q})$, respectively, should appear. From time to time, the size of the lattice happens to be too small to see them. In this case, using the fact that the peaks diverge in the thermodynamical limit, the issue is solved by increasing the lattice size.

The results for $N(\mathbf{q})$ and $S(\mathbf{q})$ for the optimal striped state at $x = 1/6$ and $\lambda = 4$, visualized in Fig.4.4, show that it is clearly ordered. $N(\mathbf{q})$ exhibits a peak for $q_x = \frac{\pi}{2}$, while $S(\mathbf{q})$ for $q_x = \frac{3}{4}\pi$ consistently with the wavelength of the stripe. The behaviour of $N(\mathbf{q})$ at $x = 1/3$ and $\lambda = 3$, associated to a really small Δ_C, is instead plotted in Fig.4.5 and confirms that this state is effectively uniform. Indeed, the correlation functions for the uniform state and the striped one at high doping do not exhibit any peaks.

The results displayed in Fig.4.3 suggest that spin modulations are more robust than the charge and AF ones when increasing the doping. For this reason, spin-spin correlations are expected to exhibit small peaks even when the charge-charge correlations do not. To show this, the correlation functions

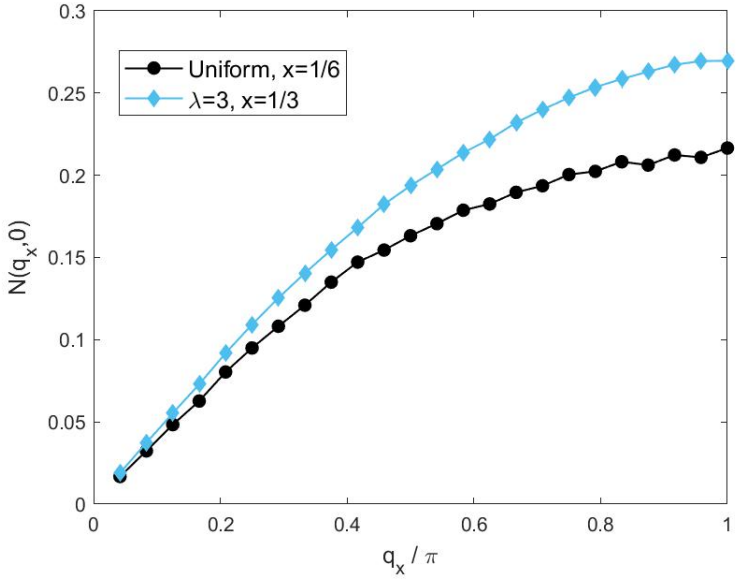

Figure 4.5: Static structure factor $N(\mathbf{q})$ as a function of q_x with $q_y = 0$. Data are reported for the non-optimal uniform state at $x = 1/6$ (circles) and the state at $x = 1/3$, $\lambda = 3$ (diamonds). In both cases $t'/t = -0.25$.

for the non-optimal striped state at $x = 1/3$, $\lambda = 3$, next to the optimal state at $x = 1/4$ and $\lambda = 3$ for comparison, are reported side by side in Fig.4.6. The peaks for the latter state are correctly located for $N(q_x, 0)$ and $S(q_x, \pi)$ at $q_x = \frac{2}{3}\pi$. We can observe though that the former, as already discussed, presents no peaks in the charge order while, on the other hand, $S(\mathbf{q})$ seems to attempt some kind of weak ordering at a wavelength close to $\lambda = 3$. Even if the state is practically uniform, as the charge ordering is not realized, the ordering of the spins tends to imitate those of the optimal wavelength, of the kind

$$\ldots \uparrow \downarrow \bigcirc \uparrow \downarrow \bigcirc \uparrow \downarrow \bigcirc \ldots$$

Now we can move on to assess the metallic or insulating behaviour of the optimal state in the case $t'/t = -0.25$ which, as a consequence of Eq.3.66, can be extracted from the small-q behaviour of the static structure factor $N(\mathbf{q})$. In

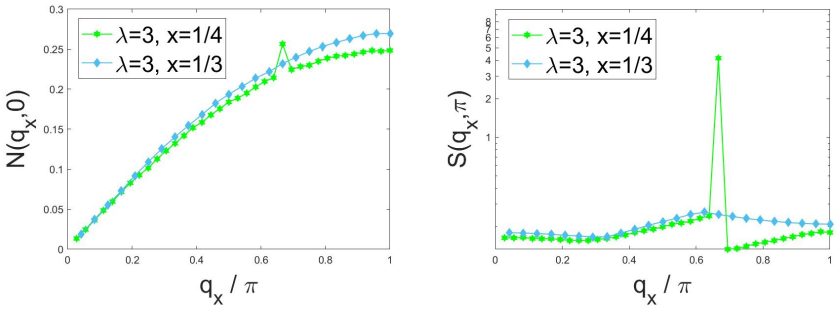

(a) (b)

Figure 4.6: *(a):* Static structure factor $N(\mathbf{q})$ as a function of q_x with $q_y = 0$. *(b):* Spin-spin correlation function $S(\mathbf{q})$ as a function of q_x with $q_y = \pi$ on a semi-log scale. The non-optimal striped state at $x = 1/3$, $\lambda = 3$ and the optimal one at $x = 1/4$ and $\lambda = 3$ are being compared. In all these cases, $t'/t = -0.25$.

particular, we proceed to plot the quantity $N(q_x, 0)/q_x$ at small q_x. The results are shown in Fig.4.7.

As a reference, we used the uniform state (circles), which is known to be metallic (except at half-filling, when each site is occupied by one electron and the Coulomb repulsion prevents them from moving freely) even though it has a higher variational energy. We observe that, for the striped state at $x = 1/6$ (squares), $N(q_x, 0)/q_x$ clearly tends to zero, compatibly with an insulating behaviour. On the other hand, for all the other striped states at $x = 1/5$ (stars) and $x = 1/4$ (hexagrams), $N(q_x, 0)/q_x$ tends to a finite value indicating that these states are metallic.

4.4 Superconductivity and Stripes

Finally, we address the coexistence of superconductivity and stripe order, by computing the superconducting order parameter of Eq.3.67 for the uniform (but not optimal) state and the optimal striped states. The results, in the case $t'/t = -0.25$, are reported in Fig.4.8. As before, we have taken the uniform

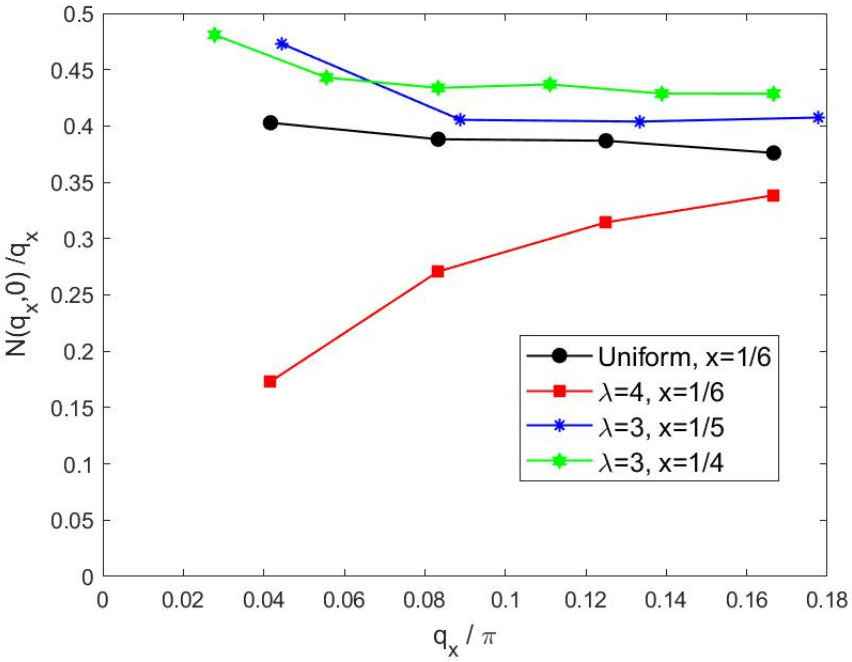

Figure 4.7: Static structure factor (divided by q_x) $N(\mathbf{q})/q_x$ as a function of q_x with $q_y = 0$. Data are reported for different hole-dopings x and $t'/t = -0.25$. The state at $x = 1/3$, being effectively uniform, has not been plotted.

state (circles) as a reference. All the striped states show strongly suppressed pair-pair correlation with respect to the uniform case. The stripe at $x = 1/5$ and $x = 1/4$, despite having a metallic character, exhibit a suppression in $D(r)$ similar to that of the insulating stripe at $x = 1/6$. This supports the idea that the stripe order disrupts superconductivity, no matter their metallic or insulating character. Also in the case $t'/t = -0.4$, the very same trend is found.

Stripes, then, are found to compete with superconductivity. Also at strong hole-doping, however, in which the stripes melt and the uniform state is restored, superconductivity cannot survive. This can be seen from the phase diagram discussed in Ch.1. Is there an "intermediate" regime in which the hole-doping is strong enough to restore the uniform state but not too strong to suppress

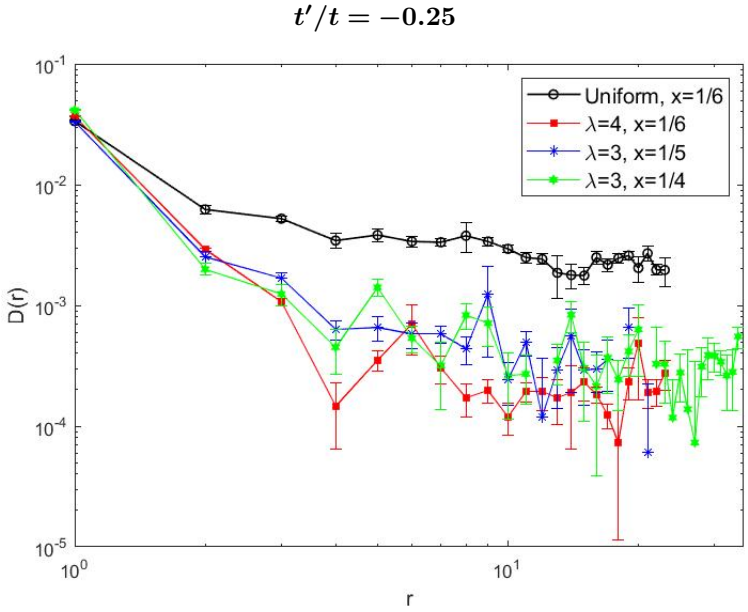

Figure 4.8: Pair-pair correlations $D(r)$ as a function of r on a log-log scale. Data are reported for different hole-dopings x and $t'/t = -0.25$. In presence of stripe order, $D(r)$ decays much faster than in the uniform state.

superconductivity? To answer this question, we look for the first value of x at which the uniform state becomes energetically favourable and compute the pair-pair correlations.

For $t'/t = -0.25$, as discussed in Table 4.1, the optimal state at $x = 1/4$ is a stripe of wavelength $\lambda = 3$ while at $x = 1/3$ we have already reached the uniform state. We then study incommensurate values of x in the range $\left[\frac{1}{4}, \frac{1}{3}\right]$. Since the wavelengths of the stripes decrease at increasing doping, it is sufficient to compare the striped state with $\lambda = 3$ and the uniform state in this doping regime. Their variational energies are presented in Table 4.4.

The difference in energy found in this range are very close to the value of the error bar, but we can identify as the "transition" doping, the value $x = 0.29$. From Fig.4.9, the pair-pair correlations for this state are plotted next to the uniform but not optimal, superconducting state at $x = 1/6$ (circles) and the non-

x	E_{stripe}	E_{uniform}	Δ_E
0.26	-0.8837 ($\lambda = 3$)	-0.8833	-0.0004
0.27	-0.8933 ($\lambda = 3$)	-0.8932	-0.0001
0.29	-0.9015 (uniform)	-0.9016	0.0001
0.31	-0.9086 (uniform)	-0.9087	0.0001

Table 4.4: Energy per site (in units of t for the best striped state E_{stripe} and the uniform state E_{uniform}, along with their relative difference $\Delta_E = E_{\text{stripe}} - E_{\text{uniform}}$, as a function of incommensurate x for $t'/t = -0.25$. Data are shown for $L_x = 48$ for all the stripes and the uniform state. The error bar on the energy is always smaller than $10^{-4}t$.

superconducting striped state at $x = 1/6$ and $\lambda = 4$ (squares) for comparison. In this "intermediate" state, superconductivity is suppressed with respect to the uniform state, most likely due to the already strong hole-doping, but less than the striped, insulating one, even if x in the latter is much smaller.

To complete this analysis, it is worth investigating the analogous situation in the case $t'/t = -0.4$ in which, as we have already mentioned, the effect of a higher $|t'/t|$ is to shorten the stripes faster and reach the uniform state at a smaller doping x. The suppression of the stripes at a lower concentration of holes might be associated to the presence of stronger superconducting correlations. Following the same reasoning as before, by looking at Table 4.2, the doping at which the uniform state prevails again is for x in the range $\left[\frac{1}{5}, \frac{1}{4}\right]$. The variational energies for these states are recorded in Table 4.5.

As expected, the stripes are suppressed earlier, already at $x = 0.21$. The pair-pair correlations for the case $t'/t = -0.4$, the commensurate doping values considered and the incommensurate "transition" state, are shown in Fig.4.10. Again, we can see how correlations in the "transition" state (triangles) are suppressed with respect to the uniform but not optimal, superconducting state at $x = 1/6$ (denoted also in this case by circles), but still stronger than in the

$$t'/t = -0.25$$

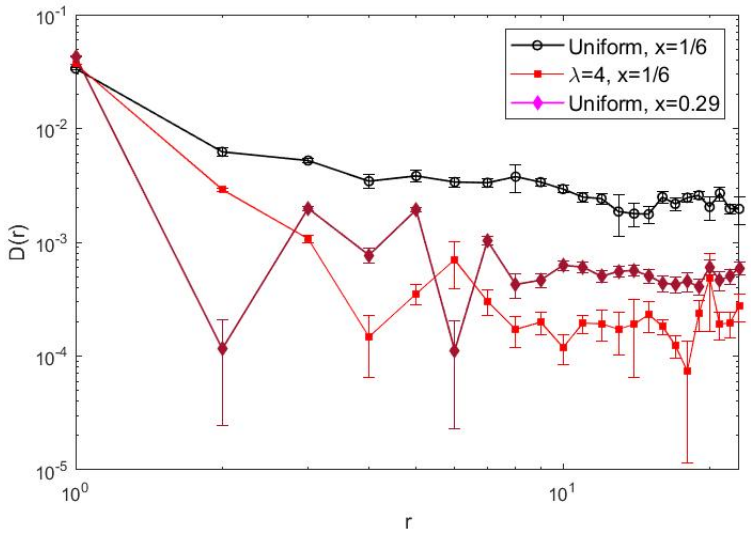

Figure 4.9: Pair-pair correlations $D(r)$ as a function of r on a log-log scale, for $t'/t = -0.25$. The "transition" state at $x = 0.29$ (denoted by diamonds) is reported along with the uniform, superconducting state at $x = 1/6$ (circles) and the non-superconducting striped state at $x = 1/6$ and $\lambda = 4$ (squares).

cases where the stripe order is established.

To make sure this "transition" state is effectively the most superconducting at high x, we show in Fig.4.11 the same curves of Fig.4.10 along with the pair-pair correlations for the remaining incommensurate doping values in Table 4.5.

To conclude the discussion, we went on to compare the magnitude of the superconducting correlations. The curves are plotted in Fig.4.12. We observe how, when $|t'/t|$ is larger, superconductivity for the uniform state is slightly suppressed. This is equally true for the uniform states at high hole-dopings x, when the uniform state is restored. This suggests that not only high dopings, but also larger values of $|t'/t|$ undermine the instauration of superconductivity. Even more notably, the role of $|t'/t|$ might be dominant, since even a definitely smaller values of x in the case $t'/t = -0.4$ is not enough to strengthen the

x	E_{stripe}	E_{uniform}	Δ_E
1/5	-0.8250 ($\lambda = 3$)	-0.8244	-0.0005
0.21	-0.8321 (uniform)	-0.8323	0.0002
0.22	-0.8448 (uniform)	-0.8449	0.0001
0.24	-0.8557 (uniform)	-0.8559	0.0002
1/4	-0.8650 ($\lambda = 3$)	-0.8654	0.0004

Table 4.5: Energy per site (in units of t for the best striped state E_{stripe} and the uniform state E_{uniform}, along with their relative difference $\Delta_E = E_{\text{stripe}} - E_{\text{uniform}}$, as a function of incommensurate x for $t'/t = -0.4$. Data are shown for $L_x = 48$ for all the stripes and the uniform state. The error bar on the energy is always smaller than $10^{-4}t$.

correlations.

$$t'/t = -0.4$$

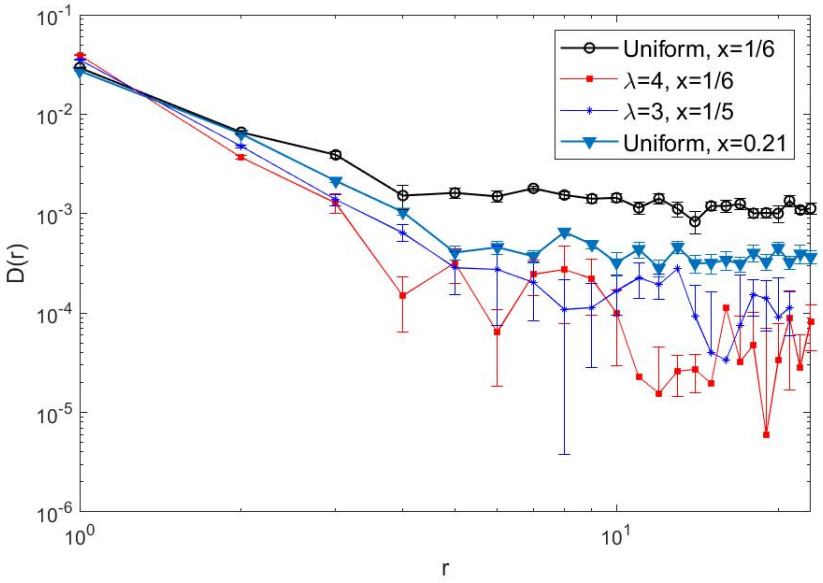

Figure 4.10: Pair-pair correlations $D(r)$ as a function of r on a log-log scale. Data are reported for different hole-dopings x and $t'/t = -0.4$. The "transition" state at $x = 0.21$ (denoted by triangles) is reported. In presence of stripe order, as already found for $t'/t = -0.25$, $D(r)$ decays much faster than in the uniform state.

$t'/t = -0.4$

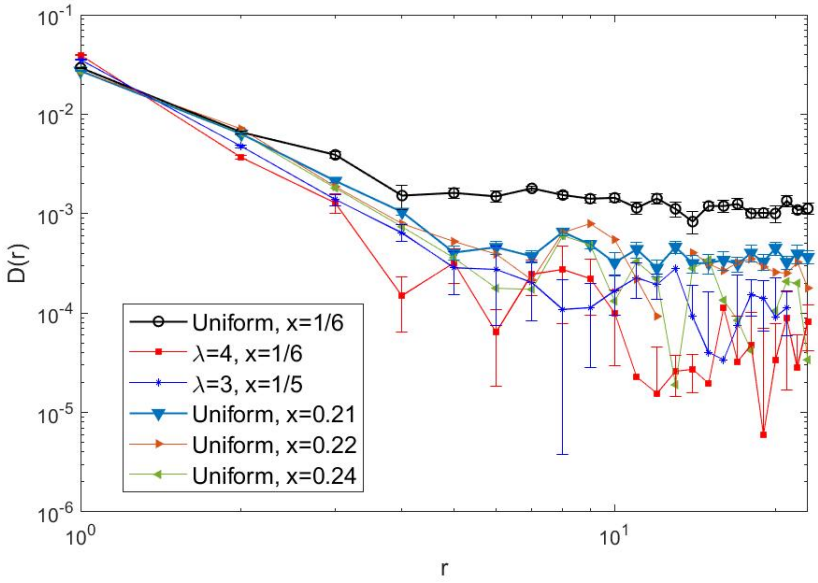

Figure 4.11: Pair-pair correlations $D(r)$ as a function of r on a log-log scale. Data are reported for all the different hole-dopings x considered and $t'/t = -0.4$. The "transition" state at $x = 0.21$ (denoted by triangles) is the most superconducting uniform state, after the disappearance of the striped states at high hole-dopings.

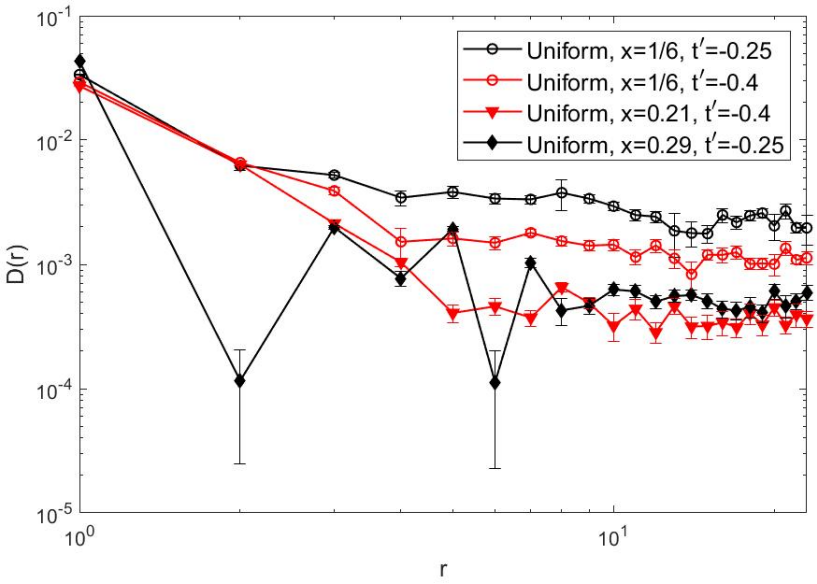

Figure 4.12: Comparison of the pair-pair correlations $D(r)$ as a function of r on a log-log scale, for the uniform but not optimal, superconducting states at $x = 1/6$ and the two "transition" states for the two values of $|t'/t|$. A larger value of $|t'/t|$ seems associated to a suppression of superconductivity, even when the hole doping required to suppress the stripe order is smaller.

Chapter 5

Conclusion

In this thesis we explored the consequences of increasing hole doping on the instauration of stripe order, superconductivity and their reciprocal interplay. The Variational Monte Carlo method, which allowed us to find the variety of results shown in Ch.4, proved to be a valuable tool to simulate many-body, strongly correlated, quantum systems such as cuprates. The two values of the next-nearest-neighbour hopping $|t'/t|$ served as an additional degree of freedom to better understand the role of this material-dependent parameter in the case of two prototypical different compounds in the family of cuprates (with $t'/t = -0.25$ and $t'/t = -0.4$).

By looking for the optimal state for different values of the hole-doping x, we found that stripes are present over a broad range of doping values, as they are energetically favourable in comparison to the uniform state. Site and bond-centered stripes, which we considered for stripes with odd and even wavelength λ respectively, have been found to be essentially degenerate energy, suggesting that there is no relevant difference between the two configurations. Upon increasing x, the wavelength of the stripes shrinks until eventually the uniform state is restored. A larger $|t'/t|$ is associated to a faster dissolution of the stripes and leads to the uniform state at a smaller x, probably due to a frustration in the formation of superconducting singlets.

The inspection of the gap parameters Δ_C, Δ_S and Δ_{AF} related to the "strength" of the charge, spin, and Néel modulations respectively, showed that they are suppressed as x increases. This fact conveys the idea that long-range periodic modulations cannot be stabilized and hence the shrinkage of their wavelength λ. The degeneracy in energy of the striped and uniform states, when the stripe has "melted", is associated to vanishing values of the gap parameters.

This "melting" is confirmed by looking at the correlation functions $N(\mathbf{q})$ and $S(\mathbf{q})$, which exhibit peaks in $\mathbf{q}$-space whenever charge and spin order, respectively, are present. The curves for $N(\mathbf{q})$ for a uniform state and the striped states at $x = 1/3$, associated to vanishing gap parameters, exhibit the same behaviour. Spin correlations, however, tend to be stronger than charge correlations, still resulting in weak peaks in $S(\mathbf{q})$: even though the charge ordering is not realized, the spins still attempt some order close to that of the optimal wavelength.

The coexistence of superconductivity and stripe order is finally addressed by looking at the pair-pair superconducting correlations $D(r)$. The uniform (but not optimal) state at small enough hole-doping x is found to be superconducting. For both values of $|t'/t|$, superconductivity is found to be suppressed whenever stripes (no matter their metallic or insulating nature) are present, suggesting that the two phenomena interfere with each other. Even when a large x leads to the disappearance of stripes and the consequent instauration of the uniform state, superconductivity is again suppressed due to the large number of holes among the lattice sites.

This fact led us to consider superconducting correlations for the first value of x at which the stripes melt and the uniform state is restored. This "intermediate" doping regime is indeed observed to be more superconducting than any striped state, but still less than the uniform state at smaller hole-doping. There exists, then, a small interval in x among which the hole-doping is strong enough to restore the uniform state but not too strong to suppress superconductivity. Stronger pair-pair correlations for the larger value of $t'/t = -0.4$ (with respect to the case for $t'/t = -0.25$), which we expected since the uniform state is

reached earlier, at smaller x, have not been found. Our results instead show that, in the former case, all superconducting correlations are weaker. This suggests that not only a larger $|t'/t|$ undermines superconductivity too, but its role in this suppression might dominate that of the hole-doping.

All the main results of the present work are collected and summarized by the *final phase diagram* reported in Fig.5.1.

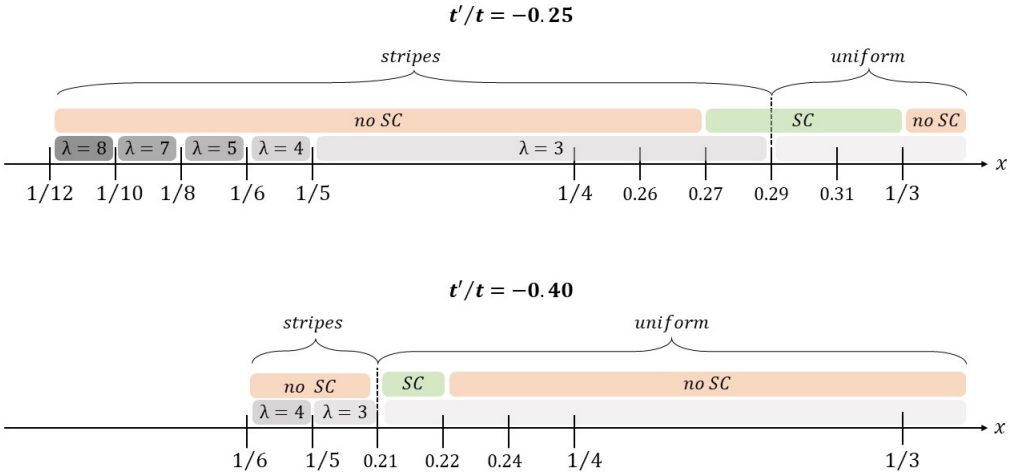

Figure 5.1: Phase diagram collecting all the main results. SC = superconductivity.

In order to identify the intermediate superconducting regions, the average of $D(r)$ over the last 10 values has been considered, because we assumed it to be a good indicator for pair-pair correlations at large r. Above the threshold value 3×10^{-4}, the state was considered superconducting[1]. The superconducting region $x \in [0.27, 0.29]$ for $t'/t = -0.25$ partially contradicts our previous statements, but in reality it is justifiable since we are right at the boundary between the two states and the striped states overcomes the uniform state very weakly.

Despite having focused on cuprates only, the phenomena investigated in the

[1] Clearly this threshold value is chosen arbitrarily, but the goal is to show evidences for some residual superconductivity in between the striped states and the uniform (but strongly-doped) one.

present work are extremely common in many other high-temperature superconductors too, and we are confident that our findings might contribute to a deeper understanding of their physics.

5.1 Future Developments

Of course, there is still a lot of work to be done in this field.

First of all, we remark that the VMC method relies on an *ansatz* that may eventually introduce some bias in the results. The one we considered, though, is expected to be general and flexible enough to account properly for the phenomena studied.

Different values for the Coulomb interaction U could be taken into account. In the present work we focused on a constant $U/t = 8$, appropriate to make the system strongly correlated and able to eventually stabilize the striped states. However, a more complete picture is obtained by considering even more correlated systems with, for instance, $U/t = 12$ or $U/t = 16$.

A more systematic study on the role of $|t'/t|$ is expected to be significant, in order to better understand how this further parameters affects superconductivity.

A major issue in our results, however, is the overestimation of the striped phase when changing the hole-doping, in comparison to experimental observations. Superconductivity is expected to be more dominant and, consequently, there must exist additional details actually missing in the current model that better suppress the stripe order. Some possible improvements could involve extending the Coulomb interaction up to the nearest-neighbours, and not only on-site. Further hopping terms might also play a non-negligible role.

Two papers very recently[2] published tried to address the limitations of the single-band Hubbard model which, despite its simplicity, for many decades proved to be sufficient to describe the physics of HTSCs. In [54], Jiang *et. al.* started from a three-band Hubbard model (i.e the Cu $d_{x^2-y^2}$, O p_x and O

[2]March 2023. This "very recently" is going to sound very funny to my future self.

p_y orbitals) and successively reduced it to an effective single-band model. In [55], an enhanced superconductivity is found by calculations on an *ab initio* model.

Bibliography

[1] J. Sólyom, *Fundamentals of the Physics of Solids: Volume 3-Normal, Broken-Symmetry, and Correlated Systems*, vol. 3. Springer Science & Business Media, 2010.

[2] J. Sólyom, *Fundamentals of the Physics of Solids: Volume II: Electronic Properties*, vol. 2. Springer Science & Business Media, 2008.

[3] J. Bardeen, L. N. Cooper, and J. R. Schrieffer, "Theory of superconductivity," *Physical review*, vol. 108, no. 5, p. 1175, 1957.

[4] V. Emery, S. Kivelson, and J. Tranquada, "Stripe phases in high-temperature superconductors," *Proceedings of the National Academy of Sciences*, vol. 96, no. 16, pp. 8814–8817, 1999.

[5] J. M. Tranquada, "Spins, stripes, and superconductivity in hole-doped cuprates," in *AIP Conference Proceedings*, vol. 1550, pp. 114–187, American Institute of Physics, 2013.

[6] J. G. Bednorz and K. A. Müller, "Possible hight c superconductivity in the ba-la- cu- o system," *Zeitschrift für Physik B Condensed Matter*, vol. 64, no. 2, pp. 189–193, 1986.

[7] F. Zhang and T. Rice, "Effective hamiltonian for the superconducting cu oxides," *Physical Review B*, vol. 37, no. 7, p. 3759, 1988.

[8] P. W. Anderson, "The resonating valence bond state in la2cuo4 and superconductivity," *science*, vol. 235, no. 4793, pp. 1196–1198, 1987.

[9] A. Damascelli, Z. Hussain, and Z.-X. Shen, "Angle-resolved photoemission studies of the cuprate superconductors," *Reviews of modern physics*, vol. 75, no. 2, p. 473, 2003.

[10] M. Newman and R. M. Ziff, "Efficient monte carlo algorithm and high-precision results for percolation," *Physical Review Letters*, vol. 85, no. 19, p. 4104, 2000.

[11] O. Vajk, P. Mang, M. Greven, P. Gehring, and J. Lynn, "Quantum impurities in the two-dimensional spin one-half heisenberg antiferromagnet," *Science*, vol. 295, no. 5560, pp. 1691–1695, 2002.

[12] C. Niedermayer, C. Bernhard, T. Blasius, A. Golnik, A. Moodenbaugh, and J. Budnick, "Common phase diagram for antiferromagnetism in la 2- x sr x cuo 4 and y 1- x ca x ba 2 cu 3 o 6 as seen by muon spin rotation," *Physical review letters*, vol. 80, no. 17, p. 3843, 1998.

[13] E. Pavarini, I. Dasgupta, T. Saha-Dasgupta, O. Jepsen, and O. Andersen, "Band-structure trend in hole-doped cuprates and correlation with t c max," *Physical review letters*, vol. 87, no. 4, p. 047003, 2001.

[14] M. Lilly, K. Cooper, J. Eisenstein, L. Pfeiffer, and K. West, "Evidence for an anisotropic state of two-dimensional electrons in high landau levels," *Physical Review Letters*, vol. 82, no. 2, p. 394, 1999.

[15] R. Du, D. Tsui, H. Stormer, L. Pfeiffer, K. Baldwin, and K. West, "Strongly anisotropic transport in higher two-dimensional landau levels," *Solid State Communications*, vol. 109, no. 6, pp. 389–394, 1999.

[16] J. Schrieffer, X.-G. Wen, and S.-C. Zhang, "Spin-bag mechanism of high-temperature superconductivity," *Physical review letters*, vol. 60, no. 10, p. 944, 1988.

[17] V. Emery, S. Kivelson, and H. Lin, "Physica b (amsterdam) 163: 306–308," *Emery VJ, Kivelson SA, Lin HQ (1990) Phys Rev Lett*, vol. 64, pp. 475–478, 1990.

[18] V. Emery, S. Kivelson, and H. Lin, "Phase separation in the t-j model," *Physical review letters*, vol. 64, no. 4, p. 475, 1990.

[19] C. S. Hellberg and E. Manousakis, "Phase separation at all interaction strengths in the tj model," *Physical review letters*, vol. 78, no. 24, p. 4609, 1997.

[20] S. Trugman, "Interaction of holes in a hubbard antiferromagnet and high-temperature superconductivity," *Physical Review B*, vol. 37, no. 4, p. 1597, 1988.

[21] J. Zaanen and O. Gunnarsson, "Charged magnetic domain lines and the magnetism of high-t c oxides," *Physical Review B*, vol. 40, no. 10, p. 7391, 1989.

[22] K. Machida, "Magnetism in la2cuo4 based compounds," *Physica C: Superconductivity*, vol. 158, no. 1-2, pp. 192–196, 1989.

[23] V. J. Emery and S. Kivelson, "Frustrated electronic phase separation and high-temperature superconductors," *Physica C: Superconductivity*, vol. 209, no. 4, pp. 597–621, 1993.

[24] J. Tranquada, B. Sternlieb, J. Axe, Y. Nakamura, and S.-i. Uchida, "Evidence for stripe correlations of spins and holes in copper oxide superconductors," *nature*, vol. 375, no. 6532, pp. 561–563, 1995.

[25] I. A. Zaliznyak and J. M. Tranquada, "Neutron scattering and its application to strongly correlated systems," *Strongly Correlated Systems: Experimental Techniques*, pp. 205–235, 2015.

[26] D. Vaknin, S. Sinha, D. Moncton, D. Johnston, J. Newsam, C. Safinya, and H. King Jr, "Antiferromagnetism in la 2 cuo 4- y," *Physical review letters*, vol. 58, no. 26, p. 2802, 1987.

[27] J. M. Tranquada, D. Buttrey, V. Sachan, and J. Lorenzo, "Simultaneous ordering of holes and spins in la 2 ni o 4.125," *Physical Review Letters*, vol. 73, no. 7, p. 1003, 1994.

[28] A. Moodenbaugh, Y. Xu, M. Suenaga, T. Folkerts, and R. Shelton, "Superconducting properties of la 2- x ba x cuo 4," *Physical Review B*, vol. 38, no. 7, p. 4596, 1988.

[29] J. Axe, A. Moudden, D. Hohlwein, D. Cox, K. Mohanty, A. Moodenbaugh, and Y. Xu, "Structural phase transformations and superconductivity in la 2- x ba x cuo 4," *Physical review letters*, vol. 62, no. 23, p. 2751, 1989.

[30] M. Fujita, H. Goka, K. Yamada, J. Tranquada, and L. Regnault, "Stripe order, depinning, and fluctuations in la 1.875 ba 0.125 cuo 4 and la 1.875 ba 0.075 sr 0.050 cuo 4," *Physical Review B*, vol. 70, no. 10, p. 104517, 2004.

[31] K. Yamada, C. Lee, K. Kurahashi, J. Wada, S. Wakimoto, S. Ueki, H. Kimura, Y. Endoh, S. Hosoya, G. Shirane, *et al.*, "Doping dependence of the spatially modulated dynamical spin correlations and the superconducting-transition temperature in la 2- x sr x cuo 4," *Physical Review B*, vol. 57, no. 10, p. 6165, 1998.

[32] S.-W. Cheong, G. Aeppli, T. Mason, H. Mook, S. Hayden, P. Canfield, Z. Fisk, K. Clausen, and J. Martinez, "Incommensurate magnetic fluctuations in la 2- x sr x cuo 4," *Physical review letters*, vol. 67, no. 13, p. 1791, 1991.

[33] S. Hayden, G. Lander, J. Zarestky, P. Brown, C. Stassis, P. Metcalf, and J. Honig, "Incommensurate magnetic correlations in la 1.8 sr 0.2 nio 4," *Physical review letters*, vol. 68, no. 7, p. 1061, 1992.

[34] C. Chen, S. Cheong, and A. Cooper, "Charge modulations in la 2- x sr x nio 4+ y: ordering of polarons," *Physical review letters*, vol. 71, no. 15, p. 2461, 1993.

[35] O. Zachar, S. Kivelson, and V. Emery, "Landau theory of stripe phases in cuprates and nickelates," *Physical Review B*, vol. 57, no. 3, p. 1422, 1998.

[36] P. Wochner, J. Tranquada, D. Buttrey, and V. Sachan, "Neutron-diffraction study of stripe order in la 2 nio 4+ δ with δ= 2 15," *Physical Review B*, vol. 57, no. 2, p. 1066, 1998.

[37] S. A. Kivelson, E. Fradkin, and V. J. Emery, "Electronic liquid-crystal phases of a doped mott insulator," *Nature*, vol. 393, no. 6685, pp. 550–553, 1998.

[38] N. W. Ashcroft and N. D. Mermin, *Solid state physics*. Cengage Learning, 2022.

[39] H. Bruus and K. Flensberg, *Many-body quantum theory in condensed matter physics: an introduction*. OUP Oxford, 2004.

[40] R. Comin and A. Damascelli, "Resonant x-ray scattering studies of charge order in cuprates," *Annual Review of Condensed Matter Physics*, vol. 7, pp. 369–405, 2016.

[41] D. McMorrow and J. Als-Nielsen, *Elements of modern X-ray physics*. John Wiley & Sons, 2011.

[42] F. De Bergevin and M. Brunel, "Observation of magnetic superlattice peaks by x-ray diffraction on an antiferromagnetic nio crystal," *Physics Letters A*, vol. 39, no. 2, pp. 141–142, 1972.

[43] F. Becca and S. Sorella, *Quantum Monte Carlo approaches for correlated systems*. Cambridge University Press, 2017.

[44] S. Sorella, "Green function monte carlo with stochastic reconfiguration," *Physical review letters*, vol. 80, no. 20, p. 4558, 1998.

[45] M. Snajdr and S. M. Rothstein, "Are properties derived from variance-optimized wave functions generally more accurate? monte carlo study of non-energy-related properties of h 2, he, and lih," *The Journal of Chemical Physics*, vol. 112, no. 11, pp. 4935–4941, 2000.

[46] L. F. Tocchio, A. Montorsi, and F. Becca, "Metallic and insulating stripes and their relation with superconductivity in the doped hubbard model," *SciPost Physics*, vol. 7, no. 2, p. 021, 2019.

[47] V. Marino, F. Becca, and L. F. Tocchio, "Stripes in the extended $t\theta$\prime $hubbardmodel$: $Avariationalmontecarloanalysis,''$ $SciPostPhysics, vol.$ $12, no.$ $6, p.$ $180, 2022$.

[48] M. Qin, T. Schäfer, S. Andergassen, P. Corboz, and E. Gull, "The hubbard model: A computational perspective," *Annual Review of Condensed Matter Physics*, vol. 13, pp. 275–302, 2022.

[49] L. F. Tocchio, F. Becca, A. Parola, and S. Sorella, "Role of backflow correlations for the nonmagnetic phase of the t–t hubbard model," *Physical Review B*, vol. 78, no. 4, p. 041101, 2008.

[50] L. F. Tocchio, F. Becca, and C. Gros, "Backflow correlations in the hubbard model: An efficient tool for the study of the metal-insulator transition and the large-u limit," *Physical Review B*, vol. 83, no. 19, p. 195138, 2011.

[51] R. P. Feynman, "Atomic theory of the two-fluid model of liquid helium," *Physical Review*, vol. 94, no. 2, p. 262, 1954.

[52] J. P. LeBlanc, A. E. Antipov, F. Becca, I. W. Bulik, G. K.-L. Chan, C.-M. Chung, Y. Deng, M. Ferrero, T. M. Henderson, C. A. Jiménez-Hoyos, *et al.*, "Solutions of the two-dimensional hubbard model: Benchmarks and results from a wide range of numerical algorithms," *Physical Review X*, vol. 5, no. 4, p. 041041, 2015.

[53] B.-X. Zheng, C.-M. Chung, P. Corboz, G. Ehlers, M.-P. Qin, R. M. Noack, H. Shi, S. R. White, S. Zhang, and G. K.-L. Chan, "Stripe order in the underdoped region of the two-dimensional hubbard model," *Science*, vol. 358, no. 6367, pp. 1155–1160, 2017.

[54] S. Jiang, D. J. Scalapino, and S. R. White, "A single-band model with enhanced pairing from dmrg-based downfolding of the three-band hubbard model," *arXiv preprint arXiv:2303.00756*, 2023.

[55] M. T. Schmid, J.-B. Morée, Y. Yamaji, and M. Imada, "Superconductivity studied by solving ab initio low-energy effective hamiltonians for carrier doped cacuo _2, bi _2 sr _2 cuo _6, bi _2 sr _2 cacu _2 o _8, and hgba _2 cuo _4," *arXiv preprint arXiv:2303.06672*, 2023.